Chapter 5

Enantio-selective laser control of (4-methyl-cyclohexylidene)-fluoromethane

5.1 Introduction

In the previous chapter a simple model system, the molecule H_2POSH, was used to develop several laser control mechanisms intended to purify a racemate of preoriented molecules. The advantages of such a model were discussed in detail in section 4.2, based on certain criteria enumerated by (a) to (f). Yet, as mentioned in section 4.2, the model system can be improved, especially in terms of its experimental availability (criterion (f)) and the lifetime of its enantiomers (criterion (d)). These two criteria become crucial if an experiment is to be carried out. The proposed experiment presented in section 4.8 demands stable enantiomers that can be synthesized and purified by chemical means; H_2POSH is, in this sense, an unfavorable molecule since its enantiomers racemize immediately at room temperature and its reactivity with Oxygen is spontaneous. Therefore, a new model system, (4-methyl-cyclohexylidene)fluoromethane, shown in figure 5.1, is introduced in this chapter. The chapter starts discussing the advantages of this system and continues with one-dimensional dynamical simulations for enantio-selective laser control. Later, a second degree of freedom is introduced and finally the requirement of using pre-oriented molecules is discussed, demonstrating an approach to partially overcome this restriction.
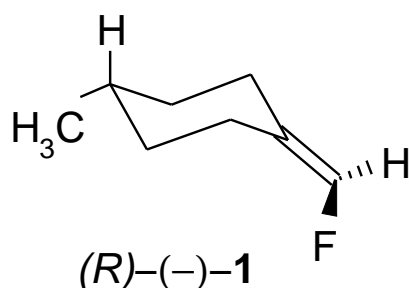
Figure 5.1: (R)-$(-)$-(4-methyl-cyclohexylidene)fluoromethane **1**

5.2   Model system

The two enantiomers of (4-methyl-cyclohexylidene)fluoromethane or 4-Me(C_6H_9)CHF, also called F-methylene-p-(eq)methyl-cyclohexane, are shown in figure 5.2. The molecule possesses a chiral axis specified by the terminal carbon atom of the ethylene group with two different substituents, namely fluorine and hydrogen, and by the carbon atom in the 4-position of the cyclohexane ring connected to a hydrogen and a methyl group. The two pairs of substituents at the opposite ends of this chiral axis form two perpendicular planes. By exchanging the substituents either on the terminal carbon of the ethylene group or on the ring carbon atom at the 4-position the opposite enantiomer is formed. Since the substitution of the hydrogen and the methyl group would require to break and reform bonds it will not be further considered. Therefore, to obtain the respective opposite chiral form the hydrogen and fluorine atom have to exchange places e.g. by rotation around the C=C double bond. Since this rotation requires to break the double bond[1], the energy barrier between the S- and R-form is so high that the molecules form stable enantiomers at room temperature, i.e. no spontaneous racemization occurs. Therefore, pure enantiomers of 4-Me(C_6H_9)CHF can be observed by experimental methods, making the molecule satisfactory in terms of criterion (d).

---

[1]The energy difference between a C=C double bonds and a C-C single bond is about 300 KJ/mol [12].
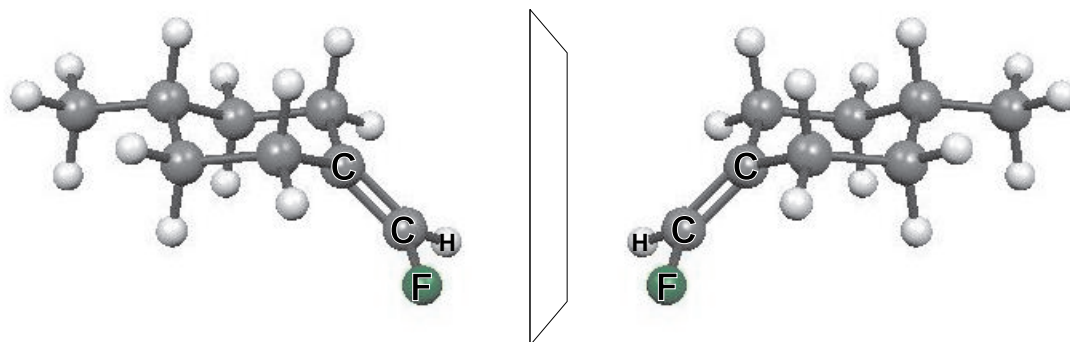
Figure 5.2: Enantiomers of (4-methyl-cyclohexylidene)fluoromethane; left of the mirror the (aR)-form and right of the mirror the (aL)-form.

Further, this model system was chosen such that its pure enantiomeric forms can be synthesized from available chemicals, fulfilling criterion (f). The here described three-step synthesis of (R)-$(-)$-(4-methyl-cyclohexylidene)fluoromethane **1**, shown in scheme 5.3, can be found in reference [142]. It starts from the purchasable achiral 4-methylcyclohexanone **2**. In the first step **a**, buthyllithium forms under metal-halogen exchange with trifluo-rochloroethylene a nucleophil that attacks the carbon of the ketone group forming the lithium alcoholate of 4-methyl-1-trifluorovinyl-cyclohexanol. Then, the alcoholate is hy-dolyzed at the difluoro-substituted terminal carbon of the double bond to the free car-bonic acid. After acidification, a water molecule is eliminated yielding a racemic mixture of (4-methyl-cyclohexylidene)fluoroacetic acid **3**. The racemate is re-crystallized with (S)-$(-)$-α-phenethylamine to give, after acification, the pure (S)-$(-)$-fluoroacetic acid **3**. The (R)-enantiomer of **3** is obtained analogously by re-crystallization with (R)-$(-)$-α-phenethylamine.

In the second step **b**, the fluoroacetic acid **3** is oxidized with bromine under elimination of carbondioxide yielding (4-methyl-cyclohexylidene)bromofluoromethane **4**. Finally, in the third step **c** the (4-methyl-cyclohexylidene)bromofluoromethane **4** reacts with magne-sium forming a Grignard which is afterwards methanolyzed to give the desired product **1**. The last two steps of the reaction **b** and **c** are stereospecific, hence, the respective S-form of the product is produced starting from the (R)-$(-)$-(4-methyl-cyclohexylidene)fluoroacetic acid. The pure (R)-$(-)$-(4-methyl-cyclohexylidene)fluoromethane **1** is a colorless liquid (bp 115-116°) with the specific rotation $[\alpha]^{20} = -38.6°$. A circular dichroism (CD) spec-

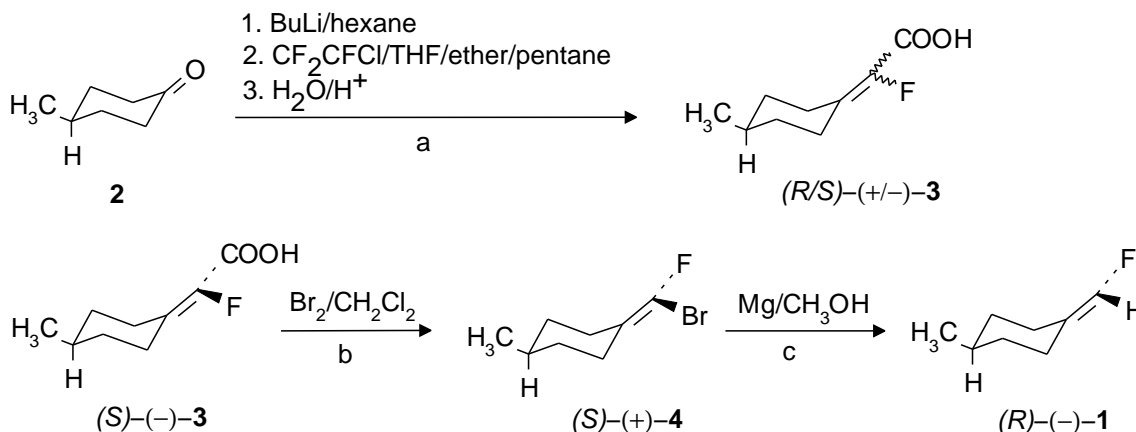trum of the deuterated species can be found in ref. [142].

Figure 5.3: Synthesis of (R)-$(-)$-(4-methyl-cyclohexylidene)fluoromethane, step **a** to **c** are explained in the text, see also refs. [143, 142].

The choice of the new model system was made such that the knowledge gained from previous results, using H_2POSH, could be used as a basis for further investigations, i.e. a model system not possessing a chiral axis would have been disadvantageous. $4\text{-}Me(C_6H_9)CHF$ allows as H_2POSH an *one-dimensional* interconversion between both enantiomers by a torsional motion around its chiral axis. The disadvantage of H_2POSH is the small (but still adequate) difference in the moment of inertia between the "moving" SH-fragment and the "fixed" H_2PO-fragment. Investigations including the coupled motion of both fragments proved that enantio-selectivity can still be obtained if circularly polarized laser pulses are used, see section 4.6.5. In the case of $4\text{-}Me(C_6H_9)CHF$ the torsional motion of the F and H around the C=C double bond can be considered to be decoupled from the cyclohexyl ring because of the high mass of the ring.

5.3 One-dimensional model simulations

5.3.1 Quantum chemical results

In analogy to H_2POSH, $4\text{-}Me(C_6H_9)CHF$ is assumed to be pre-oriented, here with its $C_1=C_2$ double bond, along the space-fixed z-axis, as depicted in figure 5.4. The F and

the H atom lie in the xz-plane while the cyclohexane ring is split symmetrically by the yz-plane with the carbon at the 4-position of the ring and the carbon of the methyl group lying in the yz-plane[2]. The torsional motion of F and H around the $C_1=C_2$ double bond is described by the angle ϕ, keeping the rest of the molecule fixed in space. The F and the H atom rotate in the same direction around the space-fixed z-axis never changing their relative position, i.e. the distances r_F, r_H and angles α_F, α_H, as defined in figure 5.4 are constant. All degrees of freedom of the rest of the molecule are kept frozen. For $\phi = 0°$ H and F are in the yz-plane with F pointing in +y direction and H pointing in -y direction. Then, the molecule has C_S symmetry (σ_{yz}) and hence, it is achiral. This is also true for $\phi = \pm 180°$ where the H-atom is pointing in $-y$ direction.
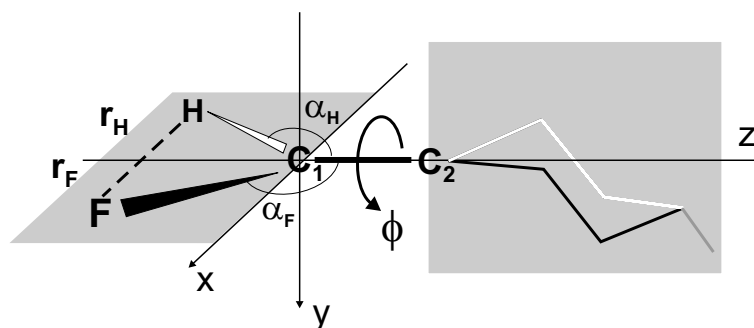

Figure 5.4: Sketch of 4-Me(C_6H_9)CHF pre-oriented in the space-fized coordinate system. The angle ϕ describes the one-dimensional torsional motion of F and H around the C=C double bond.

The geometry of the molecule has been optimized at MP2/6-311+G(d,p) level of theory. To obtain a symmetric structure for the 4-methyl-cyclohexylidene fragment, which ensures a symmetric double well potential for a *non-relaxed* PES, in practice, first both enantiomers have been optimized separately. Their geometries were built such that the following five atoms were lying in the yz-plane (see fig. 5.4): C_1, C_2, the carbon atom at the 4-position of the ring and its axial hydrogen, the carbon of the methyl group and one hydrogen connected to it. Then, the coordinates of all other atoms of the cyclohexane ring and of the methyl group were averaged from the geometry of the S- and the R-form yielding a symmetric structure with respect to the yz-plane. Relevant bond distances and angles of the optimized S-form and of the respective averaged geometry are illustrated in figure 5.5.

---

[2]The axial hydrogen atom on the carbon at the 4-position of the ring and one hydrogen of the methyl group also lie in the yz-plane.
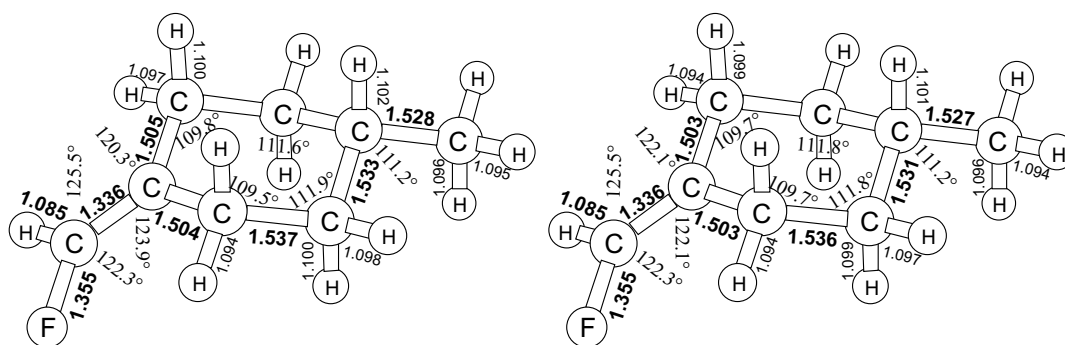
Figure 5.5: Left: Optimized geometry of (S)-4-Me(C_6H_9)CHF at MP2/6-311+G(d,p) level of theory; the optimized geometry of the R-form is the exact mirror image of the one shown. All bond distances are in Å and angles (only shown for the carbon frame including the F and H at the double bond) are in degrees. Right: Symmetrized geometry (except for F and H at the double bond) of the same molecule with averaged bond distances, angles and dihedrals from the S- and R-form.

The unrelaxed PES along the torsional angle ϕ has been calculated using DFT and TD-DFT for the ground and the electronic excited states, respectively. In particular, the hybrid functional B3LYP with a 6-311+G(d,p) basis set, as implemented in GAUSSIAN 98 package [66], was employed with the averaged geometry, depicted in fig. 5.5 (right). Figure 5.6 shows the obtained potential energy curves $V_0(\phi)$ and $V_1(\phi)$ of the electronic ground state S_0 and the electronic first excited singlet state S_1. V_0 possess two minima at $\phi = -90°$ and $+90°$ corresponding to the L- (left) and R-(right)enantiomer, respectively. The two minima are separated by two potential barriers at $\phi = 0°$ and $\phi = \pm180°$, both being of similar height (30803 cm^{-1} vs. 30855 cm^{-1}). The electronic excited state potential V_1 has minima where V_0 has its maxima.

The adiabatic curves in fig. 5.6 show the following distinctive features: i) The PESs V_0 and V_1 nearly coincide at $\phi = 0°$ and $\phi = \pm180°$, ii) the maxima of the excited potential V_1 are not exactly at $\phi = \pm90°$, where V_0 has its minima, and iii) the course of the curve V_1 is unsymmetric and rather flat between $\pm60°$ and $\pm120°$. These phenomena can be understood by taking a close look at the molecular orbitals (MOs) involved in the electronic $S_0 \rightarrow S_1$ transition at different torsional angles. Table 5.1 lists the dominant electronic transitions for the S_1, S_2 and S_3 states at $\phi = 0°, \pm90°$ and $\pm180°$, as well as the MOs involved in those transitions. Figures 5.7 to 5.9 show the relevant orbitals for $\phi = 0°, \pm90°$ and 180°, respectively.

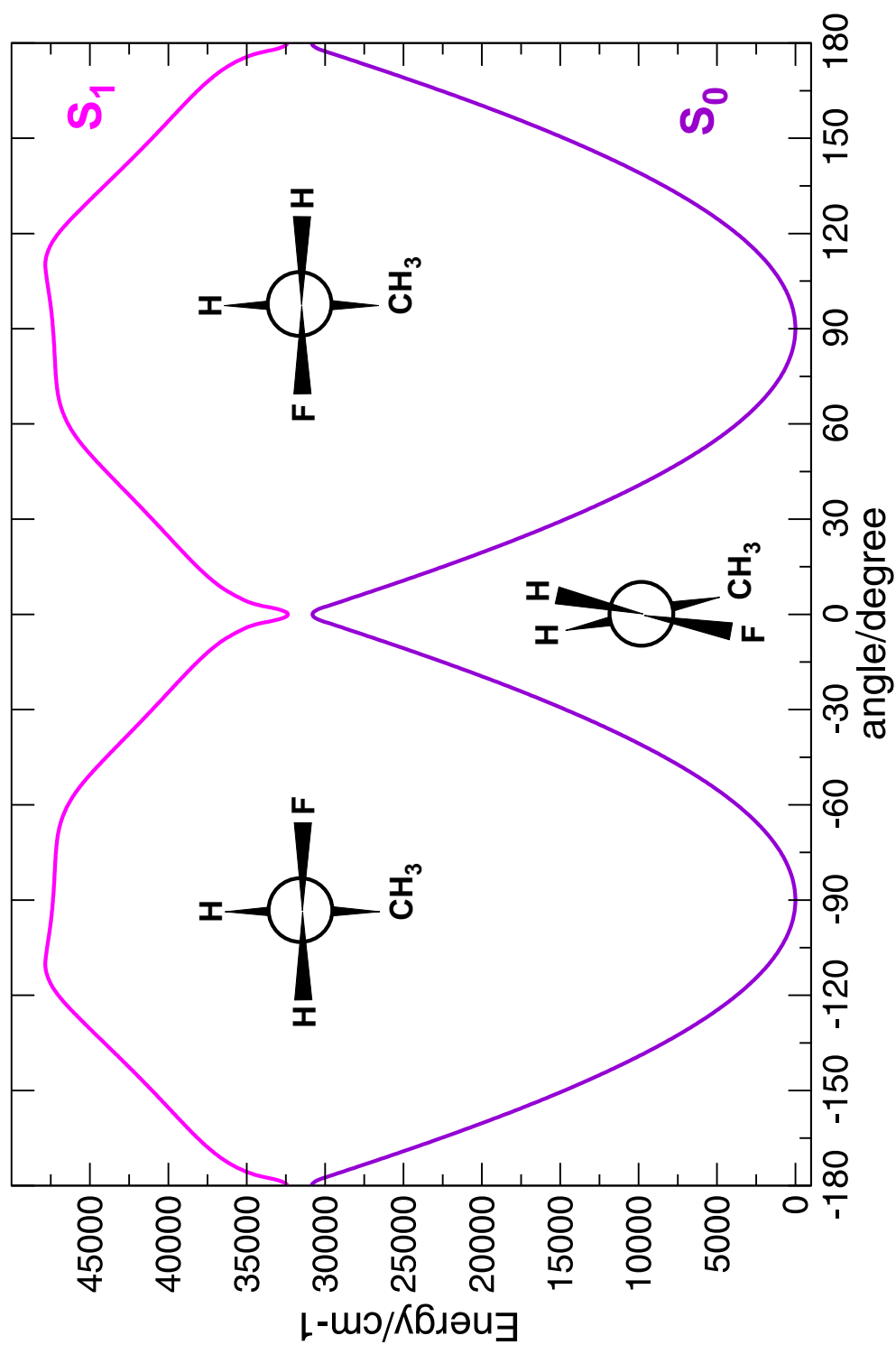Figure 5.6: Potential energy curves V_0 and V_1 of the electronic ground state S_0 and the first electronic excited singlet state S_1 along the torsional angle ϕ of 4-Me(C_6H_9)CHF calculated at B3LYP/6-311+G(d,p) level of theory. The Fisher projections along the chiral axis specify the configuration of the molecule at the respective extrema of V_0 at $\phi = 0°$ and $\phi = \pm90°$.

Figure 5.7: The HOMO (orbital 35) and LUMO (orbital 36) of (S)-4-Me(C_6H_9)CHF at the torsional angle $\phi = -90°$ as obtained from TDDFT calculations.

Figure 5.8: The HOMO (orbital 35) and the LUMO (orbital 36) of 4-Me(C_6H_9)CHF at the torsional angle $\phi = \pm 180°$ as obtained from TDDFT calculations.
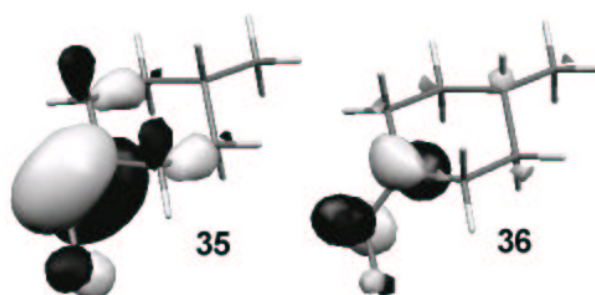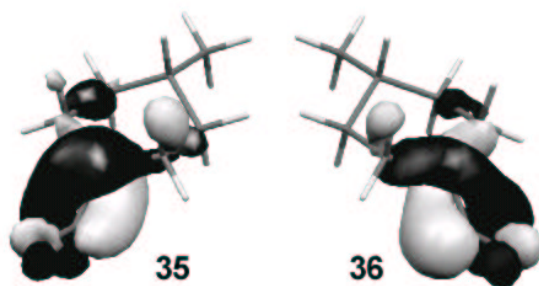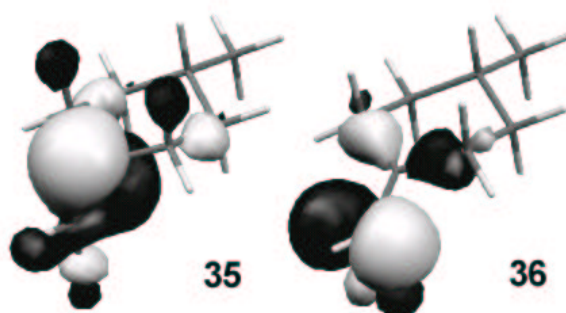

Figure 5.9: The HOMO (orbital 35) and the LUMO (orbital 36) of 4-Me(C_6H_9)CHF for the torsional angle $\phi = 0°$ as obtained from TDDFT calculations.

angle ϕ	$0°$	$\pm 90°$	$\pm 180°$
ex. state	transition/CI-coeff.	transition/CI-coeff.	transition/CI-coeff.
S_1	$35 \to 36$ / 0.73	$35 \to 36$ / 0.59 $35 \to 37$ / 0.29	$35 \to 36$ / 0.37
S_2	$35 \to 37$ / 0.68	$35 \to 36$ / 0.27 $35 \to 37$ / 0.56	$35 \to 37$ / 0.67
S_3	$34 \to 36$ / 0.52 $35 \to 38$ / 0.40	$35 \to 38$ / 0.38 $35 \to 39$ / 0.57	$35 \to 38$ / 0.68

orbital number	$\phi = 0°$ $^{(a)}$	$\phi = \pm 90°$ $^{(b)}$	$\phi = \pm 180°$ $^{(c)}$
34 (HOMO-1)	$\sigma_{CC} + \sigma_{CH}$	-	-
35 (HOMO)	$2p_y$ AO C_2	$\pi_{C_1 C_2}$	twisted $\pi_{C_1 C_2}$
36 (LUMO)	$2p_x$ AO C_1	$\pi^*_{C_1 C_2}$	twisted $\pi^*_{C_1 C_2}$
37 (LUMO+1)	Ryd. s	Ryd. s	Ryd. s
38 (LUMO+2)	Ryd. p	Ryd. p	Ryd. p
39 (LUMO+3)	-	Ryd. p	-

Table 5.1: Top: Dominant electronic transitions for S_1, S_2 and S_3 at $\phi = 0°, \pm 90°$ and $\pm 180°$ of 4-Me(C_6H_9)CHF calculated at B3LYP/6-311+G(d,p) level of theory. Bottom: Molecular orbitals for $\phi = 0°, \pm 90°$ and $\pm 180°$, (a) orbitals in fig. 5.9, (b) orbitals in fig. 5.7, (c) orbitals in fig. 5.8.

For the minimum energy configuration of the molecule at $\phi = \pm 90°$ the S_1 state is characterized by a dominant electronic transition from the orbitals 35 (HOMO) to orbital 36 (LUMO), see fig. 5.7, which corresponds to a $\pi\pi^*$ transition. Besides, there is a small contribution from the HOMO to the orbital 37 which corresponds to a Rydberg of s-type orbital. Therefore, the S_1 state is characterized by a valence-Rydberg mixing. This mixing is also found in the second excited state S_2. Hence, a differentiation betweeen the $\pi \to \pi^*$ and the $\pi \to$ Ryd. s state is difficult and the adiabatic curves calculated by TD-DFT might not give the correct energies of the excited states S_1 and S_2 around $\phi = \pm 90°$. The unsymmetric course of V_1 between $\pm 120°$ and $\pm 60°$ cannot easily be understood from the $\pi \to \pi^*$ excitation. It might be caused by avoided crossings with S_2. Figure 5.10 shows the PESs of S_1, S_2 and S_3 calculated by TD-DFT. The potential curve of S_2 shows the same unsymmetric behavior around its minima as S_1 around its maxima. In figure 5.10 dashed lines sketch the proposed course of the diabatic PES of S_1 and S_2 considering two crossings around $\phi = \pm 90°$. The excitation $S_0 \to S_3$ is assigned to a $\pi \to Ryd.p$ transition.
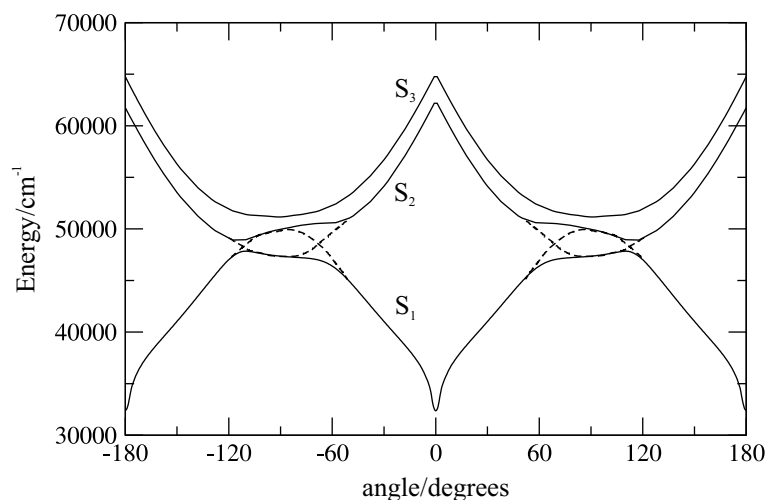
Figure 5.10: Adiabatic potential energy curves (solid line) along ϕ for the electronic excited singlet states S_1, S_2 and S_3 obtained at B3LYP/6-311+G(d,p) level of theory. Around $\phi = \pm 90°$ the curves of S_1 and S_2 show a typical behavior of avoided crossings. The dashed lines represent the assumed diabatic curves.

In going from $\phi = 90°$ to $\phi = 0°$ or $\pm 180°$ the double bond twists until the p-orbitals are perpendicular to each other. Thereby, π- and π^*-orbital of the double bond formally become identical, besides a change in phase. For $\phi = \pm 180°$, the HOMO (orbital 35) and the LUMO (orbital 36) are such a twisted π- and π^*-orbital, respectively, see fig. 5.8. The S_1 state can then be considered a $\pi\pi^*$ excitation (see table 5.1). Since these two orbitals (35 and 36) are equivalent, the character of their electronic wave functions become almost identical at $\phi = \pm 180°$ causing S_0 and S_1 to be energetically almost degenerate. Orbitals 37 and 38 are assigned to Rydberg orbitals of s and p character, therefore, S_2 and S_3 correspond to pure Rydberg transitions.

The results for $\phi = 0°$ are similar to those found for $\phi = \pm 180°$. Orbitals 35 and 36 can be considered also twisted π- and π^*-orbitals, where one of the perpendicular p-orbitals is dominant. Indeed, the HOMO (orbital 35) mainly consists of the $2p_y$-orbital at C_2, while the LUMO (orbital 36) is characterized by a $2p_x$ AO at the C_1 atom, see fig. 5.9[3]. The $S_0 \rightarrow S_1$ transition is then assigned to a $\pi\pi^*$ transition. The S_2 state, in contrast, has Rydberg character, see tab. 5.1. In case of S_3 two transitions are involved, namely a Rydberg and a $\sigma \rightarrow 2p_x$ transition.

---

[3]A close look at the twisted MOs at $\phi = 180°$ in fig. 5.8 reveals that also at that angle the $2p_y$-orbital at C_2 dominates the twisted π-HOMO while for the twisted π^*-LUMO the $2p_x$-orbital at C_1 dominates.

Since the torsional motion around the C=C double bond of 4-Me(C_6H_9)CHF is analogous to the long studied cis-trans isomerization of ethylene it is worth to compare the here obtained results with those for ethylene. Ethylene is known to posses many low-lying excited states of Rydberg character which cannot easily reproduced by *ab initio* calculations without extensive electron correlation and basis sets containing diffuse functions. In their most recent calculations [144], Ben-Nun and Martínez reported that in ethylene the $\pi \rightarrow \pi^*$ excited state (valence state V) lies above several Rydberg excited states depending on the basis set and level of electron correlation used. CASSCF with a basis set augmented with diffuse functions predicts low-lying Rydberg excited states near the ground state equilibrium geometry, while at the twisted geometry the lowest excited state was found to have pure valence character and the Rydberg states are higher in energy. At larger twisting angles Ben-Nun and Martínez also found that the energy of the ionic state Z of ethylene begins to decrease, and at $\phi = 0°$ this state is strongly coupled to the V state, including a strongly avoided crossing around $\pm 10°$. In this region, a conical intersection between the V and the Z state was found [144].

The *ab initio* results obtained for 4-Me(C_6H_9)CHF are in reasonable accordance with those found for ethylene. At the twisted geometry ($\phi = 0°/ \pm 180°$) the lowest excited state S_1 was found to have pure valence character, while S_2 and S_3 could be assigned to Rydberg states much higher in energy. Considering the diabatic PES proposed in figure 5.10, the order of the excited states S_1 and S_2 would exchange at $\phi = \pm 90°$ raising the valence state above the Rydberg state.

Based on the absorption and CD spectrum of 4-Me(C_6H_9)CHF in the gas phase Gedanken *et. al* [142] assigned the energetically lowest electronic excitation to a $\pi \rightarrow 3s$ Rydberg transition 48840 cm^{-1} and the second excitation at 51180 cm^{-1} to the $\pi \rightarrow \pi^*$ excitation. As depicted in figure 5.10 the proposed diabatic curves of S_1 and S_2 could cross twice around the equilibrium geometry of the ground state changing the energetic order of these states. The energy obtained from TDDFT at $\phi = \pm 90°$ for S_1 is 47370 cm^{-1} which is only 3% off the experimental value, and the energy for S_2 at the same angle is 49960 cm^{-1} which is 2% off the experimental value.

In conclusion, the adiabatic curves obtained for 4-Me(C_6H_9)CHF from TDDFT are probably not able to entirely describe the correct energetic characteristics of the low-lying electronic excited states. This is due to the incapability of the currently implemented TDDFT to describe double excitations and therefore, take into account the ionic state. In this case, only multiconfigurational methods like CASPT2/CASSCF can correctly describe the system. However, 4-Me(C_6H_9)CHF has a large number of electrons (70) which restricts a CASSCF calculation to a rather small basis set and a limited active space which cannot adequately describe the valence and Rydberg states. Therefore, TDDFT is a good compromise between computational costs and reliability of the results.
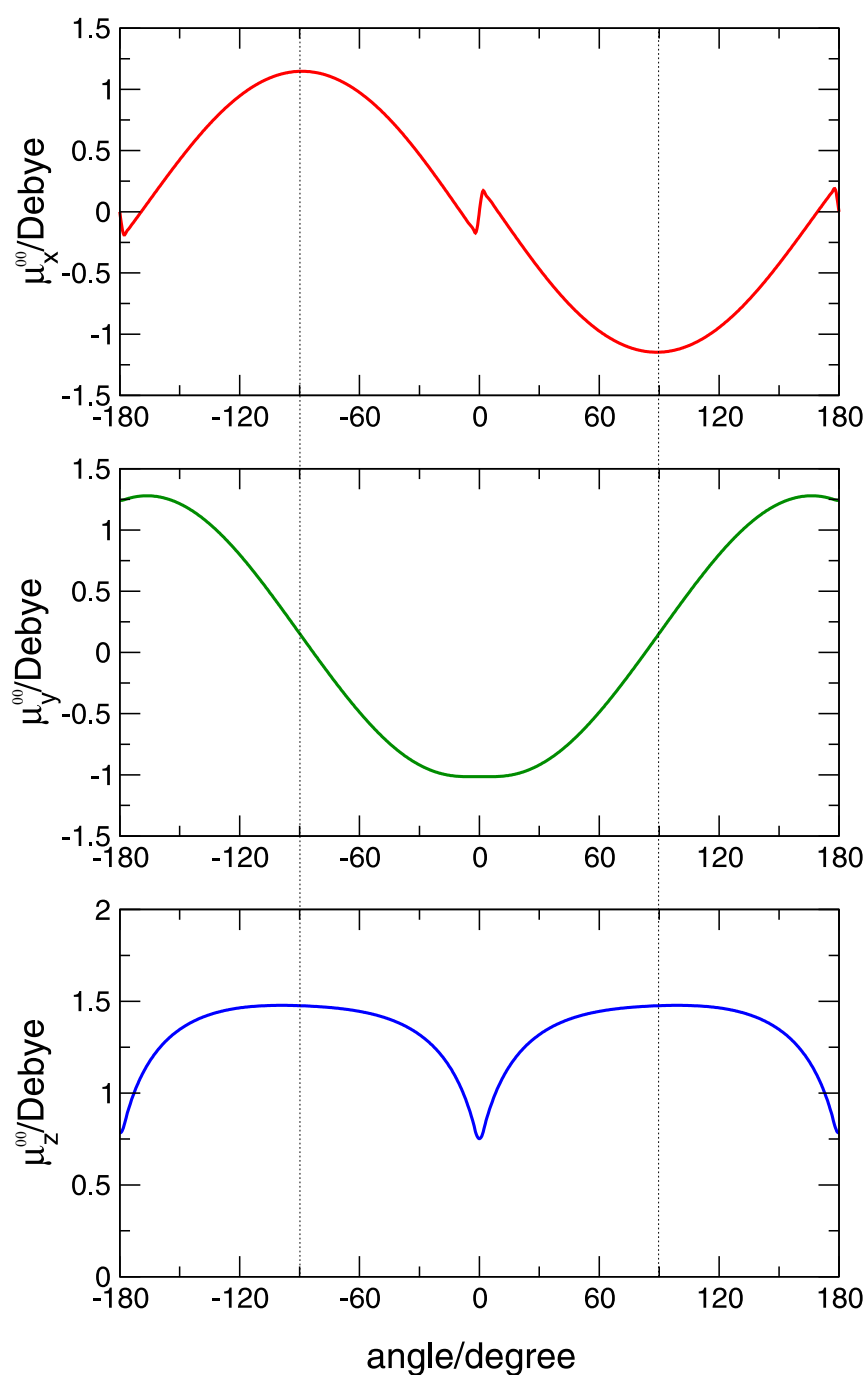
Figure 5.11: Components of the dipole moment along ϕ of the electronic ground state S_0 as obtained from DFT calculations. The dotted lines mark the equilibrium geometries for the L- and R-enantiomers.

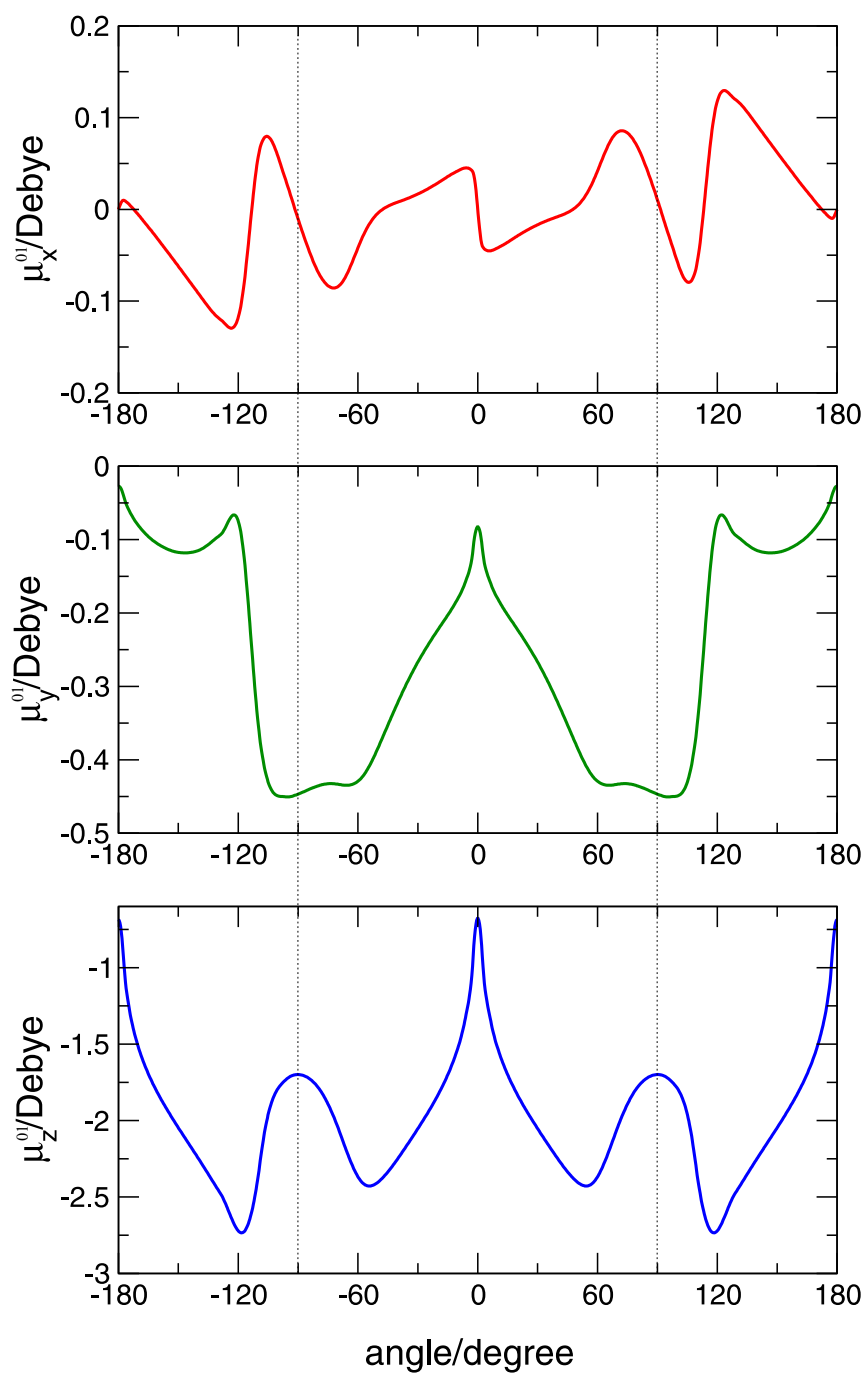Figure 5.12: Components of the electronic transition dipole moment along ϕ for transitions between S_0 and S_1 as obtained from TDDFT calculations. The dotted lines mark the equilibrium geometries for the L- and R-enantiomers.

The dipole moment $\vec{\mu}$ as a function of ϕ has been calculated at the same level of theory as used for the PES. In figure 5.11 the components of the dipole moment μ_x^{00}, μ_y^{00} and μ_z^{00} of the electronic ground state along ϕ are shown. It is important to note that μ_x^{00} is anti-symmetric with respect to $\phi = 0°$ while μ_y^{00} and μ_z^{00} are symmetric. The discontinuities around $\phi = 0°$ and $\pm 180°$ are due to the incapability of TD-DFT to describe the ionic state. However, since transitions only take place within the region from approximately $\phi = \pm 120°$ to $\pm 60°$, these artifacts do not effect the dynamical simulations. The components of the electronic transition dipole moments μ_x^{01}, μ_y^{01} and μ_z^{01} along ϕ are illustrated in figure 5.12: μ_x^{01} is the anti-symmetric component, whereas μ_y^{01} and μ_z^{01} are symmetric with respect to $\phi = 0°$.

5.3.2   One-dimensional Hamiltonian and its torsional eigenstates

In analogy to the model H_2POSH (section 4.4), the one-dimensional Hamilton operator $\hat{H}$ of $4\text{-}Me(C_6H_9)CHF$ describing the concerted torsional motion of F and H around the space-fixed z-axis is given for each electronic state i by:

$$\hat{H} = -\frac{\hbar^2}{2I_{FH}}\frac{\partial^2}{\partial\phi^2} + V_i(\phi),\tag{5.1}$$

where I_{FH} is the moment of inertia defined as

$$I_{FH} = m_F r_F^2 + m_H r_H^2\tag{5.2}$$

with m_F and m_H being the mass of the F and H atom, respectively. The distances r_F and r_H of the respective atom to the z-axis, as sketched in figure 5.4, are calculated by

$$\begin{aligned}r_H &= R_{C_1H} \cdot \sin(180° - \alpha_H)\\ r_F &= R_{C_1F} \cdot \sin(180° - \alpha_F),\end{aligned}\tag{5.3}$$

with R_{C_1H} and R_{C_1F} being the C_1-H and C_1-F bond distances.

The torsional eigenfunctions and eigenenergies of the electronic ground and first excited state are obtained as solution of the TISE (cf. section 4.4) using the Hamilton operator (5.1). The numerical calculations were carried out on a grid of 1024 points by applying the FGH method, as implemented in *qmbound* [131], using the moment of inertia $I_{FH} = 167395.73\ m_e a_0^2$ obtained from the averaged geometry. Qualitatively, the eigenfunctions $\left|\Phi_{v\pm}^0\right\rangle$ of S_0 do not differ from the ones of the H_2POSH one-dimensional model system, but because of the barrier height (ca. 30800 cm^{-1}) the number of doublets below the barrier increases drastically from six (three doublets) in case of H_2POSH to several

hundreds in case of 4-Me(C_6H_9)CHF. The energy splittings of the doublets of more than the 250 energetically lowest states is smaller than the numerical precision of 11 significant figures. For example, for the lowest doublet of eigenstates $\left|\Phi_{0\pm}^0\right\rangle$, the splitting is smaller than the numerical error of 10^{-9} cm^{-1} corresponding to tunneling time longer than 30 ms. Clearly, the tunneling times for the localized wave functions $\left|\Psi_{vL/R}\right\rangle$ cannot be calculated accurately on this level of theory. In fact, they are so long that the enantiomers of 4-Me(C_6H_9)CHF do not racemize at room temperature. In the S_1 state also doublets of eigenstates are found. Since the two minima at $\phi = 0°$ and $\phi = \pm180°$ are not identical the eigenfunctions $\left|\Phi_{v\pm}^1\right\rangle$ are either localized in the central well or in the outer well. The torsional eigenenergies for S_0 and S_1 are listed in table 5.2.

S_0		S_1		S_1	
$E_{v\pm}^0$	energy [cm^{-1}]	$E_{v\pm}^1(i/o)$	energy [cm^{-1}]	$E_{v\pm}^1(i/o)$	energy [cm^{-1}]
$0+$	94.5328	$0 + (o)$	32995.2	$125 + (i)$	47109.1
$0-$	94.5328	$1 + (i)$	33074.7	$126 - (o)$	47125.8
$1+$	283.682	$2 - (o)$	34168.6	$127 - (i)$	47172.7
$1-$	283.682	$3 - (i)$	34387.3	$128 + (i)$	47225.1
$2+$	472.931	$4 + (o)$	35167.8	$129 + (o)$	47250.6
$2-$	472.931	$5 + (i)$	35375.8	$130 - (i)$	47269.1
$3+$	662.195	$6 - (o)$	35860.0	$131 + (i)$	47309.1
$3-$	662.195	$7 - (i)$	36010.1	$132 - (i)$	47348.2
$4+$	851.439	$8 + (o)$	36395.0	$133 - (o)$	47372.3
$4-$	851.439	$9 + (i)$	36527.4	$134 + (i)$	47387.4
$5+$	1040.64	$10 - (o)$	36857.7	$135 - (i)$	47426.8
$5-$	1040.64	$11 - (i)$	36979.6	$136 + (i)$	47466.6
$6+$	1229.79	$12 + (o)$	37246.4	$137 + (o)$	47490.1
$6-$	1229.79	$13 + (i)$	37357.0	$138 - (i)$	47507.0
$7+$	1418.90	$14 - (o)$	37601.6	$139 + (i)$	47547.7
$7-$	1418.90	$15 - (i)$	37702.4	$140 - (i)$	47588.8
$8+$	1607.95	$16 + (o)$	37918.8	$141 - (o)$	47603.0
$8-$	1607.95	$17 + (i)$	38013.3	$142 + (o)$	47630.4

Table 5.2: Torsional eigenenergies for the S_0 and S_1 state of the model system 4-Me(C_6H_9)CHF. The energies of eigenfunctions localized in the central well ($\phi = 0°$) of V_1 are labelled by (i) (*inner* well) while those localized in the outer well ($\phi = \pm180°$) are denoted by an (o) (*outer* well).

Because of the height of the potential barriers, laser control using the enantio-selective pump-dump mechanism via an intermediate state within the electronic ground state po-

tential is impossible in practice. Hence, the electronic excited state S_1 becomes mandatory for the purification of the racemic mixture of enantiomers, as presented in the following section.

5.3.3   One-dimensional dynamical simulations

In the proposed experiment, introduced in section 4.8, the first step is an enantio-selective pump pulse transferring one chiral part of the initial population to an intermediate state so that the two initially energetically degenerate enantiomers of the racemic mixture become energetically separated. The electronic excited state S_1 of $4\text{-Me}(C_6H_9)CHF$ is a good choice for the intermediate state since it is energetically well separated (> 30000 cm^{-1}) from the populated states in the electronic ground state. After enantio-selective excitation of one enantiomer to the excited state by a single linearly polarized UV laser pulse, different subsequent scenarios can be conceived:

(a) An enantio-selective dump pulse transfers the population of the electronic excited state back to the ground state but selectively into the potential well of the desired enantiomer, e.g. to $|\Psi_{1L}\rangle$ or $|\Psi_{1R}\rangle$ as in the case of H_2POSH. Then, the racemic mixture is 100% purified.

(b) The population in the electronic excited state is allowed to relax back to the ground state[4]. If this decay is non-selective, i.e. population is evenly distributed to both potential minima of S_0, then a scheme analogous to the laser distillation proposed by Shapiro *et. al* [58] could be designed, repeating enantio-selective pump and unselective decay until the racemate is completely purified.

(c) Taking advantage of the energetical difference of both enantiomers after the asymmetric photo-excitation, a subsequent laser pulse could transfer the population of the intermediate state to a dissociative state eliminating there the undesired enantiomer, as proposed for H_2POSD in ref. [130].

In the following, two laser control simulations are presented that investigate the first step of the discussed scenarios. The dynamical simulations are based on the solution of the TDSE (cf. section 4.5); for the interaction with the laser field the semi-classical dipole-approximation is assumed. All simulations are carried out on a grid of 1024 points using the split operator method as implemented in the FORTRAN program *qmpropa* [133] with a time step of 0.01 fs. At initial time t_0 the system is prepared as an incoherent mixture of

---

[4]e.g. by spontaneous relaxation or via a conical intersection.

the L- and R-enantiomer in the lowest doublet of torsional eigenstates (cf. section 4.5.2) at low temperature (below $60K$):

$$\rho(t_0) = \frac{1}{2}\rho_{0L} + \frac{1}{2}\rho_{0R}. \tag{5.4}$$

The first laser control simulation is shown in figure 5.13 with laser pulse parameters listed in table 5.3. An enantio-selective linearly polarized laser pulse is designed to excite exclusively the R-enantiomer $|\Psi_{0R}\rangle$ to the torsional eigenstate $|\Phi^1_{135-}\rangle$ in the electronic excited state S_1, while leaving the L-enantiomer $|\Psi_{0L}\rangle$ unaffected.

property/parameter	UV pump pulse
dominant transition	$\left|\Phi^0_{0-}\right\rangle \rightarrow \left|\Phi^1_{135-}\right\rangle$
transition dipole matrix	$\left\langle\Phi^0_{0-}\right|\mu^{01}_z\left|\Phi^1_{135-}\right\rangle$
element$/ea_0$	$-4.3343 \cdot 10^{-1}$
coupled to laser field	E^0_z
field amplitude E^0_z/GVm^{-1}	0.06
phase $\eta_z/^\circ$	0
dominant transition	$\left|\Phi^0_{0+}\right\rangle \rightarrow \left|\Phi^1_{135-}\right\rangle$
transition dipole matrix	$\left\langle\Phi^0_{0+}\right|\mu^{01}_x\left|\Phi^1_{135-}\right\rangle$
element$/ea_0$	$-2.3898 \cdot 10^{-3}$
coupled to laser field	E^0_x
field amplitude E^0_x/GVm^{-1}	-10.9
phase $\eta_x/^\circ$	$(10.0)^{(a)}$
frequency $\omega/2\pi c \cdot cm^{-1}$	47329
duration t_p/ps	2.0
total field amplitude $\overline{E}^0/GVm^{-1}$	10.9
intensity $I_k/TW\,cm^{-2}$	31.537
polarization angle $\alpha/^\circ$	-89.7

Table 5.3: Laser pulse parameters for the control pulse depicted in figure 5.13. (a) The phase increases the enantio-selectivity slightly.
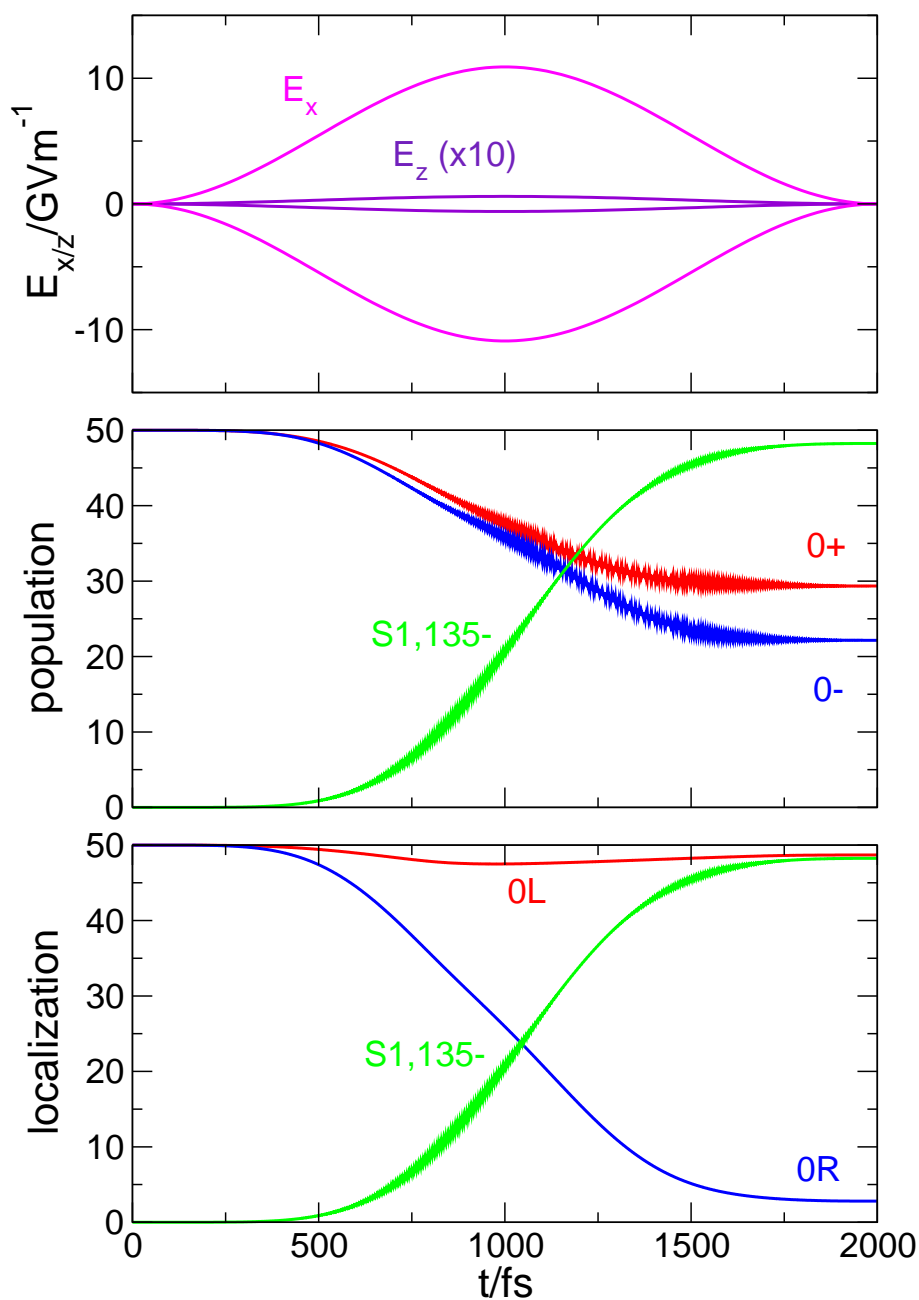
Figure 5.13: Enantio-selective photo-excitation of the R-enantiomer of 4-Me(C_6H_9)CHF to the S_1 state. Top panel: Envelope function of the linearly polarized UV pulse (parameters are given in table 5.3). Middle panel: Population dynamics of affected torsional eigenstates in S_0 and S_1 ($v\pm \ \widehat{=}\ \left|\Phi^0_{v\pm}\right\rangle$; $S1, v\pm \ \widehat{=}\ \left|\Phi^1_{v\pm}\right\rangle$). Bottom panel: Localization of the wave packet in S_0 and population of the intermediate state $\left|\Phi^1_{135-}\right\rangle$ as a function of time. Population and localization are given in percentage.

The amplitudes E_x^0 and E_z^0 of the two components of the linearly polarized UV laser pulse differ by more than a factor hundred. This is due to the large difference in the transition dipole matrix elements (see table 5.3) and can be understood by looking at the components of the electronic transition dipole moment μ_x^{01} and μ_z^{01} in fig. 5.12. The perpendicular transition from S_0 to S_1 at $\phi \approx 90°$ is induced by a laser field that couples to a very small μ_x^{01} and to a relatively large μ_z^{01} ($\approx$ -1.75 Debye) in the Franck-Condon region, see fig. 5.12. The intermediate state $\left| \Phi_{135-}^1 \right\rangle$ is chosen because it was the energetically lowest eigenstate in S_1 with a sufficient large overlap with the initial wave function $\left| \Psi_{0R} \right\rangle$ in the Franck-Condon region, causing an adequate transition dipole moment element $\left\langle \Phi_{0\pm}^0 \right| \mu_{x/z}^{01} \left| \Phi_{135-}^1 \right\rangle$. However, because of the small value of $\left\langle \Phi_{0+}^0 \right| \mu_x^{01} \left| \Phi_{135-}^1 \right\rangle$ the intensity of the laser field is rather high. Here an IR excitation prior to the UV excitation could create a wave packet that allows to choose a different intermediate state in S_1 with higher transition dipole matrix elements. This will be discussed later in this section.

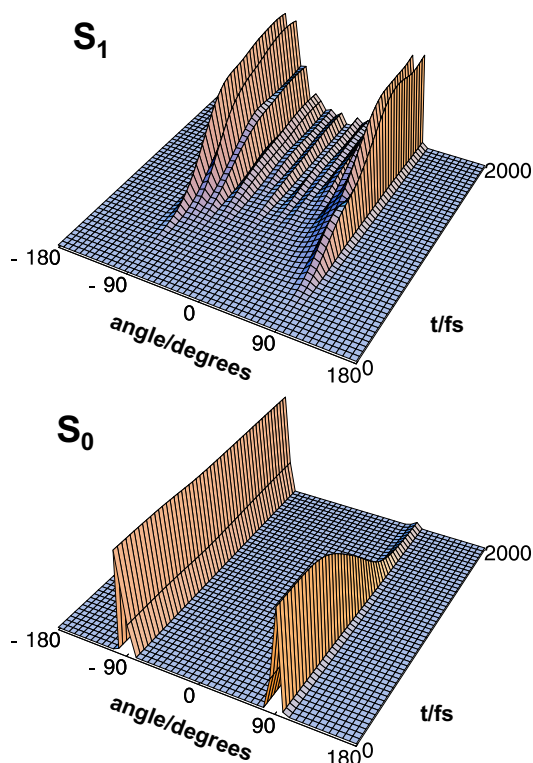Figure 5.14: Densities as a function of time for the asymmetric photo-excitation of 4-Me(C_6H_9)CHF. The electronic ground state S_0 starts initially with a racemic mixture $\frac{1}{2}\rho_{0L} + \frac{1}{2}\rho_{0R}$. The enantio-selective laser pulse excites $\left| \Psi_{0R} \right\rangle$ to the intermediate state $\left| \Phi_{135-}^1 \right\rangle$ in the electronic excited state S_1. (adapted from [130])

As shown in figure 5.13, almost 95% of the population of $|\Psi_{0R}\rangle$ is transferred to the electronic excited state S_1 and only $\sim 2\%$ of $|\Psi_{0L}\rangle$ is also excited. The selectivity of the UV pulse can be increased slightly by introducing a phase of $\eta_x = 10°$ (see table 5.3) which causes the electric field to become eliptically polarized. Figure 5.14 shows the densities of the wave function $|\Psi_{0L}\rangle$ and $|\Psi_{0R}\rangle$ as a function of time illustrating the efficiency of the asymmetric photo-excitation.

After the UV pulse an L-selective dump pulse could now transfer the population of $\left|\Phi^1_{135-}\right\rangle$ to e.g. $|\Psi_{1L}\rangle$ as discussed in scenario (a). This subsequent reaction is only possible if the lifetime of the population in S_1 is long enough for the second laser pulse to take place. The same must hold if the subsequent pulse is used to transfer the population to a dissociative state. It is known that electronic excited states of olefins often decay very fast – within the order of few hundred femtoseconds – via conical intersections to the electronic ground state [145, 146, 147, 148]. In *ab initio* calculations on ethylene including torsion and pyramidalization Ben-Nun and Martínez localized S_1/S_0 conical intersections for a pyramidalized twisted geometry [144]. If 4-Me(C_6H_9)CHF shows S_1/S_0 conical intersections scenario (b) could be applied providing the decay is unselective and an even population transfer to both wells of S_0 occurs. Since the problem of pyramidalization seems to play a major role in olefinic systems, it will be discussed in more detail in section 5.4.

In general, the described enantio-selective photo-excitation can be applied to any chiral molecule, because it only requires an intermediate state which can be reached by a single linearly polarized laser pulse. The only condition of the presented simulation is the need of a sufficient coupling between the initial state and the electronic excited intermediate state to garantee efficient population transfer. This is not always the case and hence, a modification of the photo-excitation scheme is presented in the following.

The basic concept of enantio-selective laser pulses derived in section 4.7.1 was based on the fact that the laser pulse is polarized such that it only interacts with the desired chiral form of the pre-oriented racemic mixture of molecules while the interaction with the opposite form vanishes, see eqns. (4.56) and (4.57). So far always a transition from a localized state to a pure eigenstate and vice versa was considered. Obviously eqns. (4.56) and (4.57) are also true for a transition to a localized state $\left|\Psi_{vL/R}\right\rangle$ different from the initial state $\left|\Psi_{0L/R}\right\rangle$, i.e.:

$$\langle\Psi_{0L}|\,\vec{\mu}\,|\Psi_{vL}\rangle \cdot \vec{E}^0 \;=\; 0 \qquad\qquad\qquad (5.5)$$

$$\langle\Psi_{0R}|\,\vec{\mu}\,|\Psi_{vR}\rangle \cdot \vec{E}^0 \;\neq\; 0, \qquad v = 1, 2, 3, \ldots \qquad (5.6)$$

provided $|\Psi_{0R}\rangle$ is to be excited by the laser[5]. Using the definition for $|\Psi_{vL}\rangle$ and the fact

that μ_x^{01} has $-$ symmetry and μ_y^{01} has $+$ symmetry, equation (5.5) is rewritten following the selection rule (4.19):

$$
\frac{1}{\sqrt{2}} \left(\langle \Phi_{0+}^0 | + \langle \Phi_{0-}^0 | \right) E_x^0 \cdot \mu_x^{00} \frac{1}{\sqrt{2}} \left(| \Phi_{v+}^0 \rangle + | \Phi_{v-}^0 \rangle \right)
$$
$$
= -\frac{1}{\sqrt{2}} \left(\langle \Phi_{0+}^0 | + \langle \Phi_{0-}^0 | \right) E_y^0 \cdot \mu_y^{00} \frac{1}{\sqrt{2}} \left(| \Phi_{v+}^0 \rangle + | \Phi_{v-}^0 \rangle \right)
$$
$$
\Rightarrow \frac{1}{2} E_x^0 \left(\langle \Phi_{0+}^0 | \mu_x^{00} | \Phi_{v-}^0 \rangle + \langle \Phi_{0-}^0 | \mu_x^{00} | \Phi_{v+}^0 \rangle \right)
$$
$$
= -\frac{1}{2} E_y^0 \left(\langle \Phi_{0+}^0 | \mu_y^{00} | \Phi_{v+}^0 \rangle + \langle \Phi_{0-}^0 | \mu_y^{00} | \Phi_{v-}^0 \rangle \right) \tag{5.7}
$$

In the S$_0$ the energy splitting ΔE_v of more than the 250 energetically lowest eigenstates $| \Phi_{v\pm}^0 \rangle$ is negligible. Therefore, the following transition dipole elements are approximately equal:

$$
\langle \Phi_{0+}^0 | \mu_x^{00} | \Phi_{v-}^0 \rangle \approx \langle \Phi_{0-}^0 | \mu_x^{00} | \Phi_{v+}^0 \rangle \tag{5.8}
$$
$$
\langle \Phi_{0+}^0 | \mu_y^{00} | \Phi_{v+}^0 \rangle \approx \langle \Phi_{0-}^0 | \mu_y^{00} | \Phi_{v-}^0 \rangle . \tag{5.9}
$$

Using eqns. (5.8) and (5.9) the expression (5.7) simplifies to

$$
E_x^0 \cdot \langle \Phi_{0+}^0 | \mu_x^{00} | \Phi_{v-}^0 \rangle = -E_y^0 \cdot \langle \Phi_{0+}^0 | \mu_y^{00} | \Phi_{v+}^0 \rangle . \tag{5.10}
$$

For the R-enantiomer the interaction with the laser should not vanish, see condition (5.6), hence, the following expression for $\sin^2$-shaped laser pulses is derived using (5.8) and (5.9) as well as (5.10) and by introducing the relation (4.62) of the Rabi frequency and the pulse area for π-pulse transitions:

$$
- \quad E_x^0 \cdot \langle \Phi_{0+}^0 | \mu_x^{00} | \Phi_{v-}^0 \rangle + E_y^0 \cdot \langle \Phi_{0+}^0 | \mu_y^{00} | \Phi_{v+}^0 \rangle = \frac{\hbar \Omega(t)}{s(t)} \neq 0
$$
$$
\Rightarrow \quad 2 \cdot E_y^0 \cdot \langle \Phi_{0+}^0 | \mu_y^{00} | \Phi_{v+}^0 \rangle = \frac{2\pi\hbar}{t_p} . \tag{5.11}
$$

Then, the amplitude of each component of the linear polarized enantio-selective laser pulse is given by

$$
E_y^0 = \frac{\pi\hbar}{\langle \Phi_{0+}^0 | \mu_y^{00} | \Phi_{v+}^0 \rangle t_p} \approx \frac{\pi\hbar}{\langle \Phi_{0-}^0 | \mu_y^{00} | \Phi_{v-}^0 \rangle t_p} \tag{5.12}
$$
$$
E_x^0 = -\frac{\pi\hbar}{\langle \Phi_{0+}^0 | \mu_x^{00} | \Phi_{v-}^0 \rangle t_p} \approx -\frac{\pi\hbar}{\langle \Phi_{0-}^0 | \mu_x^{00} | \Phi_{v+}^0 \rangle t_p} \tag{5.13}
$$

---

[5]Note that $\langle \Psi_{0R} | \vec{\mu} | \Psi_{1L} \rangle$ and $\langle \Psi_{0L} | \vec{\mu} | \Psi_{1R} \rangle$ are equal zero.

provided $|\Psi_{0R}\rangle$ is to be excited to $|\Psi_{vR}\rangle$ ($v > 0$). Similarly, for $|\Psi_{0L}\rangle$ to be pumped to an energetically higher localized state $|\Psi_{vL}\rangle$ the components of the laser pulse amplitudes become:

$$E_y^0 \;=\; \frac{\pi\hbar}{\langle\Phi_{0+}^0|\,\mu_y^{00}\,|\Phi_{v+}^0\rangle\,t_p} \approx \frac{\pi\hbar}{\langle\Phi_{0-}^0|\,\mu_y^{00}\,|\Phi_{v-}^0\rangle\,t_p} \tag{5.14}$$

$$E_x^0 \;=\; \frac{\pi\hbar}{\langle\Phi_{0+}^0|\,\mu_x^{00}\,|\Phi_{v-}^0\rangle\,t_p} \approx \frac{\pi\hbar}{\langle\Phi_{0-}^0|\,\mu_x^{00}\,|\Phi_{v+}^0\rangle\,t_p} \tag{5.15}$$

with $E_x^0 \cdot \langle\Phi_{0+}^0|\,\mu_x^{00}\,|\Phi_{v-}^0\rangle = E_y^0 \cdot \langle\Phi_{0+}^0|\,\mu_y^{00}\,|\Phi_{v+}^0\rangle$.

In figures 5.15 (top) the result of a R-selective IR pulse on 4-Me(C_6H_9)CHF is shown. The localized state $|\Psi_{0R}\rangle$ is excited to a manifold of excited doublets from $|\Psi_{1R}\rangle$ to $|\Psi_{8R}\rangle$[6] creating a wave packet travelling between $\phi = 77°$ and $103°$. The laser pulse is optimized for the transition $|\Psi_{0R}\rangle \rightarrow |\Psi_{1R}\rangle$, but because of the harmonicity of the potential well for small torsional quantum numbers v, higher doublets up to $|\Psi_{8R}\rangle$ are also populated, cf. fig. 5.16 and tab. 5.4. The L-enantiomer $|\Psi_{0L}\rangle$ is affected by less than 1% and small torsional motion is observed (see oscillations of the density ρ_{0L} in fig. 5.15).

Following the IR pulse, a subsequent enantio-selective UV laser pulse pumps the population of the coherent superposition of R-states $|\Psi_{0R}^0(t_{p1})\rangle$ ($\approx \sum_{v=1}^{8} c_v |\Psi_{vR}\rangle$) to the electronic excited state S_1, as depicted in fig. 5.15 (bottom). This UV pump pulse is short and hence, broad enough in frequency to cover most of the populated R-localized states. Further, the pulse is optimized[7] such that the wave packet in the right well is excited when it reaches its turning point at $\phi \approx 77°$, there the coupling to the state $|\Phi_{128+}^1\rangle$ is maximal. While the wave packet in S_0 moves towards higher angles (to the right) the laser pulse connects it also to higher states in S_1, mainly to $|\Phi_{130-}^1\rangle$, $|\Phi_{131+}^1\rangle$ and $|\Phi_{132-}^1\rangle$, but also to energetically close states, e.g. $|\Phi_{127-}^1\rangle$, $|\Phi_{134+}^1\rangle$, $|\Phi_{135-}^1\rangle$, $|\Phi_{136+}^1\rangle$, $|\Phi_{138-}^1\rangle$, $|\Phi_{139+}^1\rangle$ and $|\Phi_{140-}^1\rangle$[8]. The population in the left well of S_0 is virtually not affected by this second pump pulse: about 1.5% of the population of $|\Psi_{0L}\rangle$ is excited temporarily to S_1 but returns before the UV laser pulse is switched off (cf. fig. 5.15). The wave packet created in the electronic excited state S_1 moves primarily towards the left, i.e. towards $\phi = -90°$, as depicted in 5.15 (bottom). At $t = 7500$ fs a subsequent laser pulse could dump the wave packet to the left well of the electronic ground state, thereby satisfying scenario (a). For scenario (b) the condition of unselective decay to the electronic ground state would not be fulfilled, if the wave packet will relax primarily into the well which is along its path. If relaxation were included into the model simulations, a scenario could be designed where such a selective decay could be used to obtain the desired enantiomer. Of

---

[6]$|\Psi_{9R}\rangle$ is populated less than 1%.

[7]The envelope of the laser field has its maximum.

[8]The states $|\Phi_{129+}^1\rangle$, $|\Phi_{133-}^1\rangle$ and $|\Phi_{137+}^1\rangle$ are localized in the outer minima at $\phi = \pm180°$.

course, also scenario (c) can be applied to the here discussed results. A subsequent pump pulse could excite the wave packet from S_1 to a dissociative state eventually destroying the R-enantiomer.
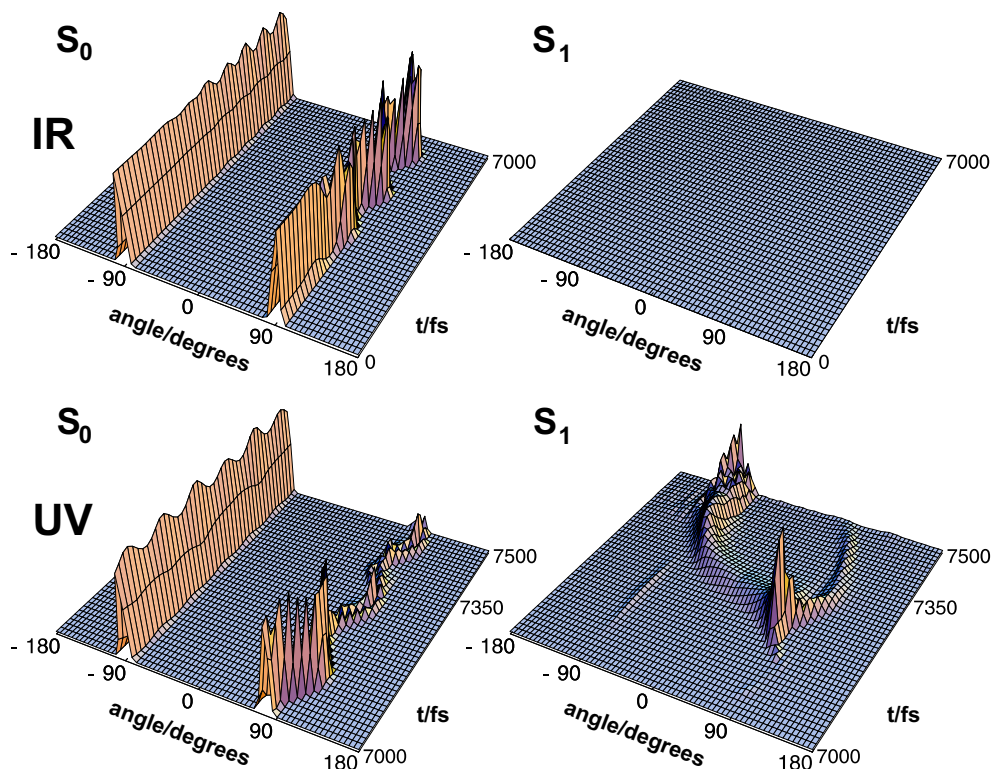

Figure 5.15: Densities as a function of time for a sequence of an IR and UV enantio-selective pump pulses on 4-Me(C_6H_9)CHF. Top: Effect of the first IR pulse on the densities ρ_{0L} and ρ_{0R} in the electronic ground state S_0 (left) and the electronic excited state S_1 (right). Bottom: Effect of the UV excitation induced by the second laser pulse.

In figure 5.16 the envelopes of the laser pulse components of the complete laser pulse sequence as well as the population dynamics are shown, table 5.4 lists the respective laser parameters. For the IR pulse the field amplitudes E_y^0 and E_x^0 differ by a factor 50 due to the dipole matrix elements. Again a look at the curves of μ_y^{00} and μ_x^{00} in fig. 5.11 gives some explanation. While μ_y^{00} changes by about 1 Debye within $77° < \phi < 103°$, μ_x^{00} stays almost constant. Since the coupling with an anti-symmetric dipole component is necessary for an enantio-selective laser pulse, and the value of $\left\langle \Phi_{0\pm}^0 \middle| \mu_x^{00} \middle| \Phi_{1\mp}^0 \right\rangle$ is small, the high value of E_x^0 cannot be diminished unless longer laser pulses are employed.
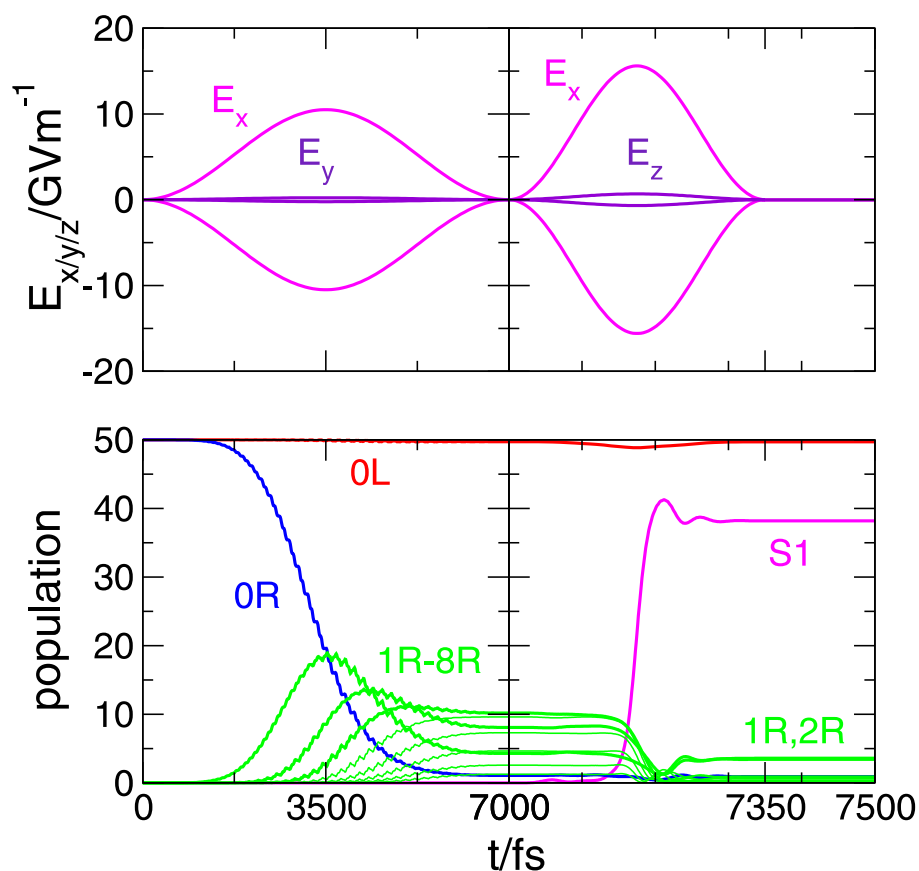
Figure 5.16: Selective excitation of the R-enantiomer of 4-Me(C_6H_9)CHF by using a sequence of an IR and an UV laser pulse. Top panel: Envelope of the linearly polarized IR and UV pulse (parameters are found in table 5.3). Bottom panel: Population dynamics in percentage of the affected localized states in S_0 ($vL/R \mathrel{\widehat{=}} \left|\Psi_{vL/R}\right\rangle$) and the overall population of S_1 ($S1 \mathrel{\widehat{=}} \sum_v \left|\Phi^1_{v\pm}\right\rangle$) as a function of time. Note the different time scales used for the IR and UV laser pulses.

The transition dipole matrix element $\left\langle \Psi^0_{0R}(t_{p1}) \right| \mu^{01}_x \left| \Phi^1_{128+} \right\rangle$ for the UV transition is about five times larger than the one of the previous simulation, see tab. 5.3. Still, the amplitude E^0_x is even higher than previously. This is due to the short duration of the laser pulse needed to cover most of the populated R-localized states. Therefore, an increase of the pulse duration would make the control less effective even though it decreases the high laser intensity. Here the quasi-harmonicity of V_0 makes laser control difficult because a pure eigenstate cannot be reached by the IR excitation. In comparison with the direct UV excitation the here presented mechanism is even less effective: less than 80% of the R-enantiomer is electronically excited by the UV pulse (see fig. 5.16). In the following

section the model system is extended by a second degree of freedom. The new degree of freedom offers the possibility for a modified laser control mechanism with more effective transitions by less intense laser pulses.

property/parameter	IR pump pulse	UV pump pulse
dominant transition	$\lvert\Psi_{0R}\rangle \rightarrow \sum_{v=1}^{\sim 8} c_v \lvert\Psi_{vR}\rangle$	$\sum_{v=1}^{\sim 8} c_v \lvert\Psi_{vR}\rangle \rightarrow S_1$
(transition) dipole matrix	$\langle\Phi_{0\pm}^0\rvert \mu_y^{00} \lvert\Phi_{1\pm}^0\rangle$	$\langle\Psi_{0R}^0(t_{p_1})\rvert \mu_z^{01} \lvert\Phi_{128+}^1\rangle$
element$/ea_0$	$30.080 \cdot 10^{-3}$	-0.22920
coupled to laser field	E_y^0	E_z^0
field amplitude E_i^0/GVm^{-1}	0.231	0.68
phase $\eta_i/^\circ$	0	0
(transition) dipole matrix	$\langle\Phi_{0\pm}^0\rvert \mu_x^{00} \lvert\Phi_{1\mp}^0\rangle$	$\langle\Psi_{0R}^0(t_{p_1})\rvert \mu_x^{01} \lvert\Phi_{128+}^1\rangle$
element$/ea_0$	$-0.66107 \cdot 10^{-3}$	-0.010102
coupled to laser field	E_x^0	E_x^0
field amplitude E_i^0/GVm^{-1}	10.5	-15.6
phase $\eta_i/^\circ$	0	0
frequency $\omega_i/2\pi c \cdot cm^{-1}$	189.15	$46652^{(a)}$
duration t_{p_i}/ps	7.0	0.35
total field amplitude $\overline{E}^0/GVm^{-1}$	10.5	15.6
intensity $I_k/TWcm^{-2}$	29.265	64.598
polarization angle $\alpha/^\circ$	88.7	-87.5

Table 5.4: Laser pulse parameters for the IR+UV laser pulse sequence depicted in figure 5.16. (a) The transition frequency was initially chosen as the energetic difference between the wave packet in the ground state $\lvert\Psi_{0R}^0(t_{p_1})\rangle$ and $\lvert\Phi_{128+}^1\rangle$.

5.4   Two-dimensional model including pyramidalization

5.4.1   Quantum chemical results

So far all dynamical simulations for 4-Me(C_6H_9)CHF were based on a one-dimensional model reduced to the direct reaction path between the two enantiomers. Although this simplification is an instructive approximation, a second degree of freedom will offer a better understanding of the efficiency and restrictions of the investigated laser control.

Ethylene, as the simplest model of a C=C double bond undergoes pyramidalization after $\pi \rightarrow \pi^*$ excitation, as first noticed by Salem and coworkers [149, 150]. This pyramidalization indicates a hybridization change of one carbon atom from sp^2 to sp^3. *Ab initio* calculations have proven that pyramidalization plays an important role on the ethylene dynamics in the valence state [151]. After excitation to the valence state the ethylene begins to twist around the C=C bond and subsequently one of the methylene units pyramidalizes leading directly to a conical intersection [144, 152]. The ionic state $(\pi \rightarrow \pi^*)^2$ is responsible for the stabilization of the pyramidalized geometry of ethylene in the electronic excited state [144]; formally it can be described as a localized negative charge stabilized at the sp^3 hybridized pyramidalized methylene group and a sp^2 hybridized positively charged unpyramidalized methylene group. This pyramidalized state of the C=C double bond should be even more favorable for the cyclohexylidene derivative, since the fluorine stabilizes a formal negative charge on the C_1 atom due to its high electronegativity. Therefore, the pyramidalization coordinate is an obvious extension of the one-dimensional model of $4\text{-Me}(C_6H_9)\text{CHF}$.

Figure 5.17 shows a sketch of the part of $4\text{-Me}(C_6H_9)\text{CHF}$ that undergoes twisting and pyramidalization. Both terminal substituents F and H at the C_1 carbon are formally rotated together in the same direction either around the laboratory fixed z-axis for twisting or for pyramidalization around a fictive axis P which is perpendicular to the z-axis[9], cf. fig. 5.17. For $\theta = 0°$ the original one-dimensional torsion is obtained by changing ϕ; for $\theta = \pm 90°$ the F and H atoms are in the xy-plane, cf. fig. 5.4.
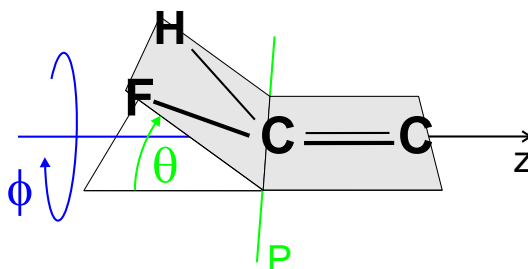

Figure 5.17: Sketch of twisting along ϕ and pyramidalization along θ for the pre-oriented $4\text{-Me}(C_6H_9)\text{CHF}$.

Figures 5.18 and 5.19 depict the unrelaxed two-dimensional PES for the ground $(V_0(\phi, \theta))$ and first excited state $(V_1(\phi, \theta))$, respectively, calculated at B3LYP/6-311+G(d,p) level of theory. As in the 1D calculations the averaged geometry shown in fig. 5.5 was used as reference geometry. The PESs are constructed from 324 points retrieved from

---

[9]For $\phi = \pm 90°$ it is the x-axis.

ab initio calculations. To obtain smooth two-dimensional surfaces Akima's surface fitting method SURF[10], as implemented in the IMSL mathematical library [153], was used.

Both PESs possess an inversion center at $\phi = 0°, \theta = 0°$, with the pyramidalization angle θ defined positive for a specific direction of the rotation around the molecule fixed axis P, see fig. 5.17. The electronic ground state potential V_0 has two equivalent minima at $\phi = \pm 90°, \theta = 0°$ corresponding to the L- and R-enantiomers. The potential V_1 shows two minima at $\phi = 0°, \theta = 0°$ and $\phi = \pm 180°, \theta = 0°$, respectively, centered in valleys along θ, see fig. 5.19. After excitation of (S)-4-Me(C_6H_9)CHF to the S_1 state the double bond will undergo torsion, but not necessarily pyramidalization.

The permanent dipole moment as a function of ϕ and θ was calculated at the same level of theory as the PES. The components of the permanent dipole moment μ_x^{00}, μ_y^{00} and μ_z^{00} are shown in figures 5.20, 5.21 and 5.22. The corresponding electronic transition dipole moment components μ_x^{01}, μ_y^{01} and μ_z^{01} are found in figures 5.23, 5.24 and 5.25. Since the PESs possess an center of inversion all components of dipole and transition dipole moments are either symmetric or anti-symmetric with respect to inversion at $\phi = 0°, \theta = 0°$. This behavior is labeled by g (*gerade*) if the function is symmetric with respect to inversion and u (*ungerade*) if it is anti-symmetric with respect to $\phi = 0°, \theta = 0°$, i.e. if the the sign of the function is changed. Therefore, μ_x^{00}, μ_x^{01} are *ungerade* and all other components (μ_y^{00}, μ_z^{00} and μ_y^{01} and μ_z^{01}) are *gerade*.

The one-dimensional potential curves for S_0 and S_1, as well as the components of the permanent and of the electronic transition dipole moment along ϕ, as used in section 5.3, can be obtained from figures 5.18 to 5.25 as cuts along $\theta = 0°$.

---

[10]The algorithm of SURF returns values of a bivariate interpolant to scattered data in plane; it utilizes piecewise quintic polynomials on a triangular mesh.
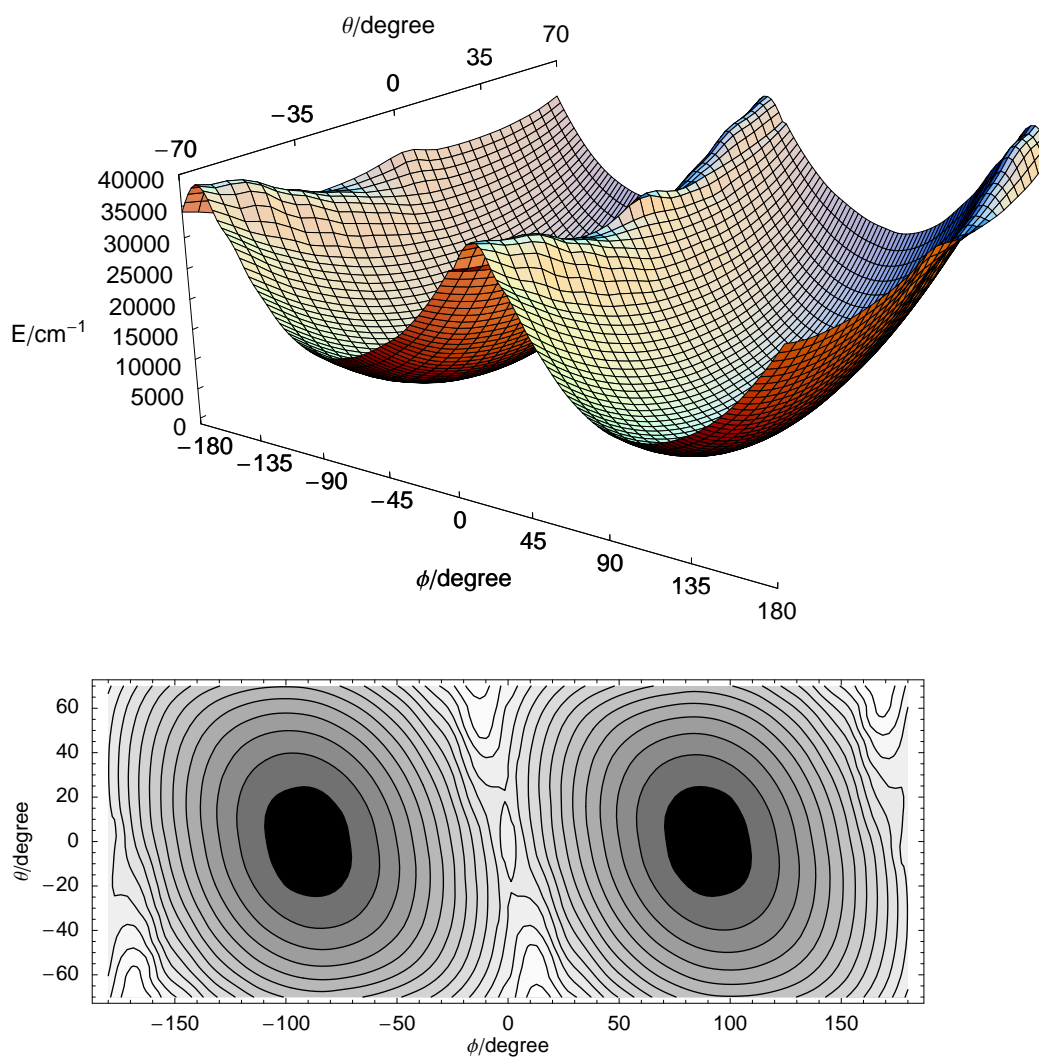
Figure 5.18: PES (top) and contour plot (bottom) of the electronic ground state S_0 of 4-Me(C_6H_9)CHF as a function of the torsion angle ϕ and the pyramidalization angle θ, calculated at B3LYP/6-311+G(d,p) level of theory. Equicontour lines $V_0(\phi, \theta) = E_0 + i\Delta E$, i=1–16, E_0/cm^{-1} = 37, ΔE/cm^{-1} = 2427.
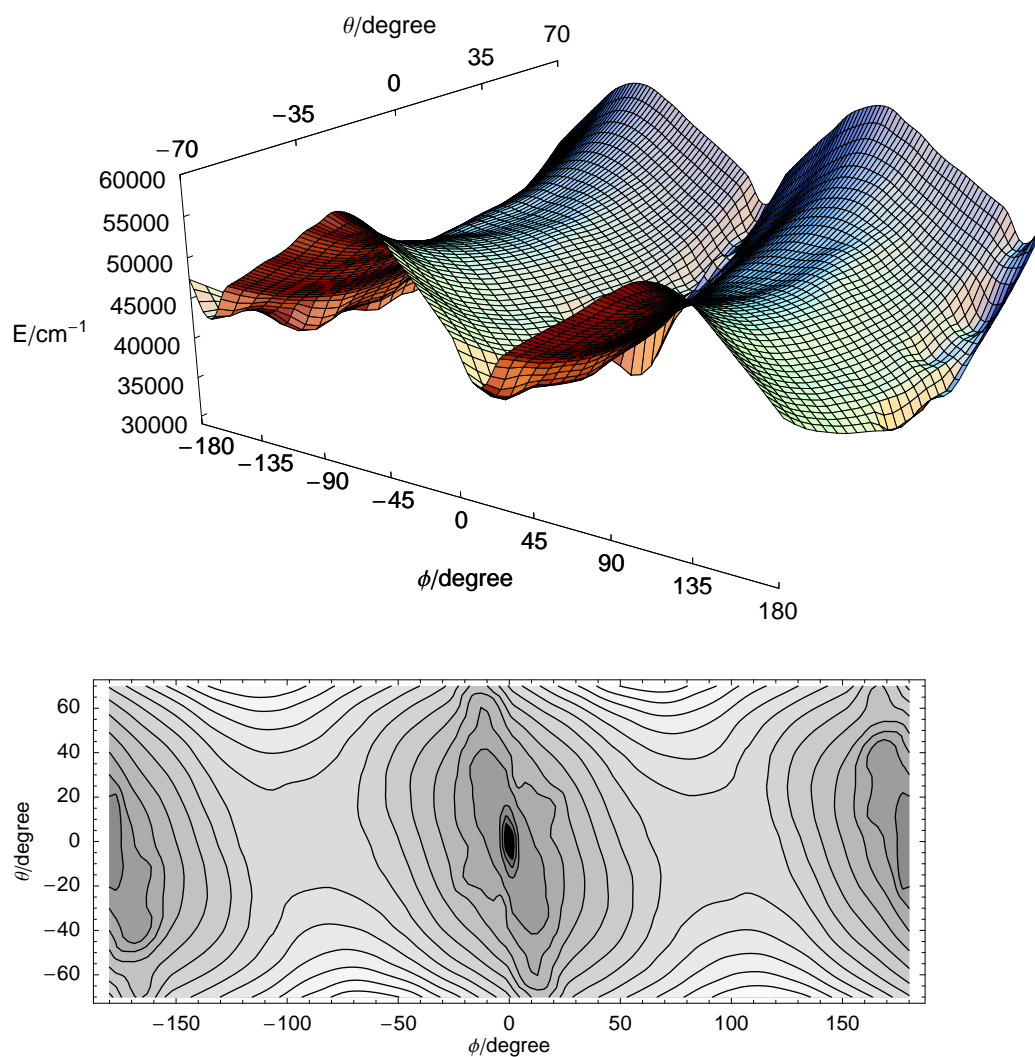
Figure 5.19: PES (top) and contour plot (bottom) of the electronic first excited singlet state S_1 of 4-Me(C_6H_9)CHF as a function of the torsion angle ϕ and the pyramidalization angle θ, calculated at B3LYP/6-311+G(d,p) level of theory. Equicontour lines $V_1(\phi, \theta) = E_0 + i\Delta E$, i=1–16, E_0/cm^{-1} = 30569, ΔE/cm^{-1} = 1793.

Figure 5.20: 2D-surface (top) and contour plot (bottom) of the x-component μ_x^{00} of the permanent dipole moment of 4-Me(C_6H_9)CHF as a function of the torsion angle ϕ and the pyramidalization angle θ, calculated at B3LYP/6-311+G(d,p) level of theory. Equicontour lines $\mu_x^{00}(\phi,\theta) = \mu_0 + i\Delta\mu$, i=1–16, μ_0/Debye = -1.168, $\Delta\mu$/Debye = 0.146.

Figure 5.21: 2D-surface (top) and contour plot (bottom) of the y-component μ_y^{00} of the permanent dipole moment of 4-Me(C_6H_9)CHF as a function of the torsion angle ϕ and the pyramidalization angle θ, calculated at B3LYP/6-311+G(d,p) level of theory. Equicontour lines $\mu_y^{00}(\phi,\theta) = \mu_0 + i\Delta\mu$, i=1–16, μ_0/Debye $= -1.224$, $\Delta\mu$/Debye $= 0.183$.
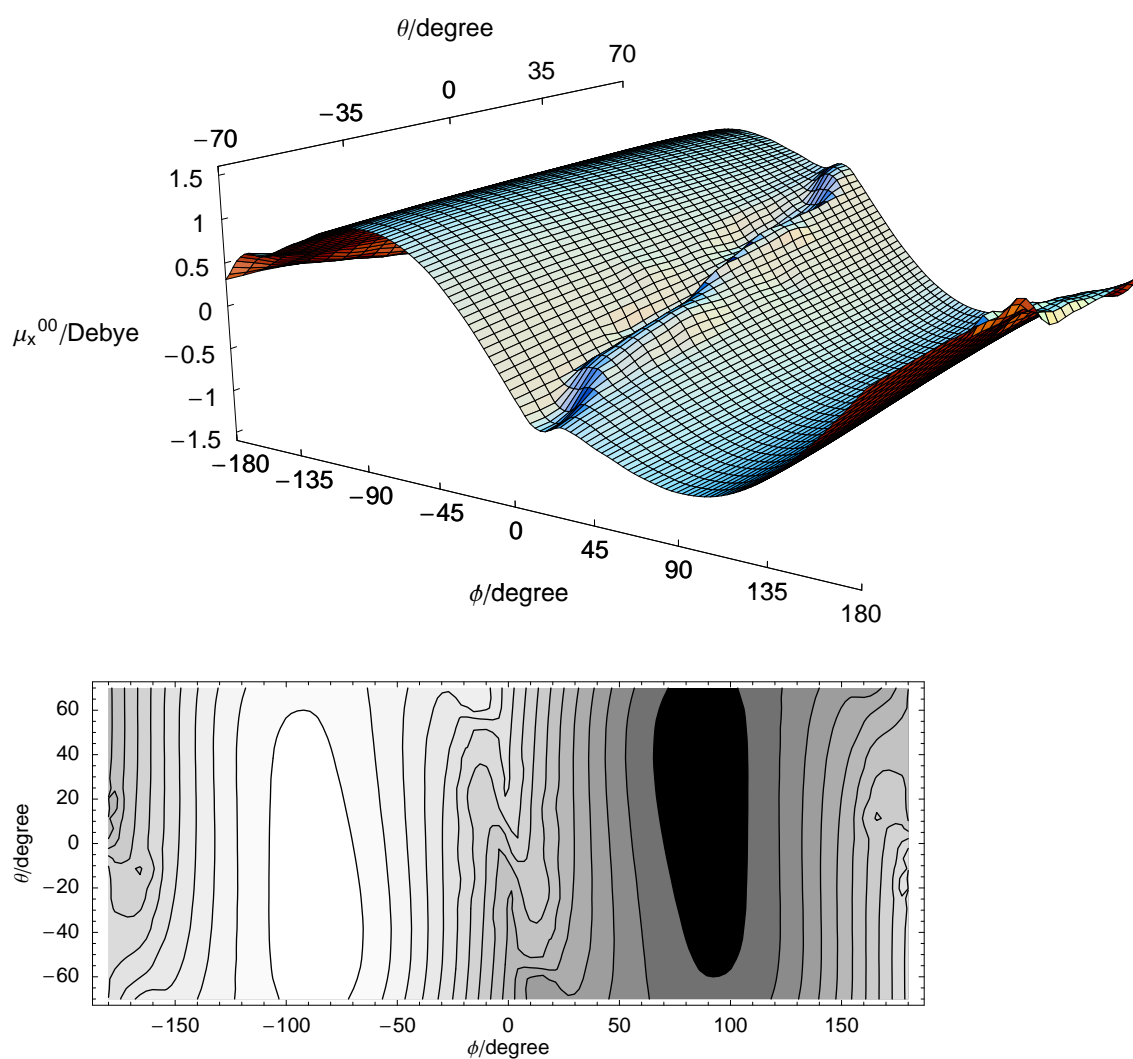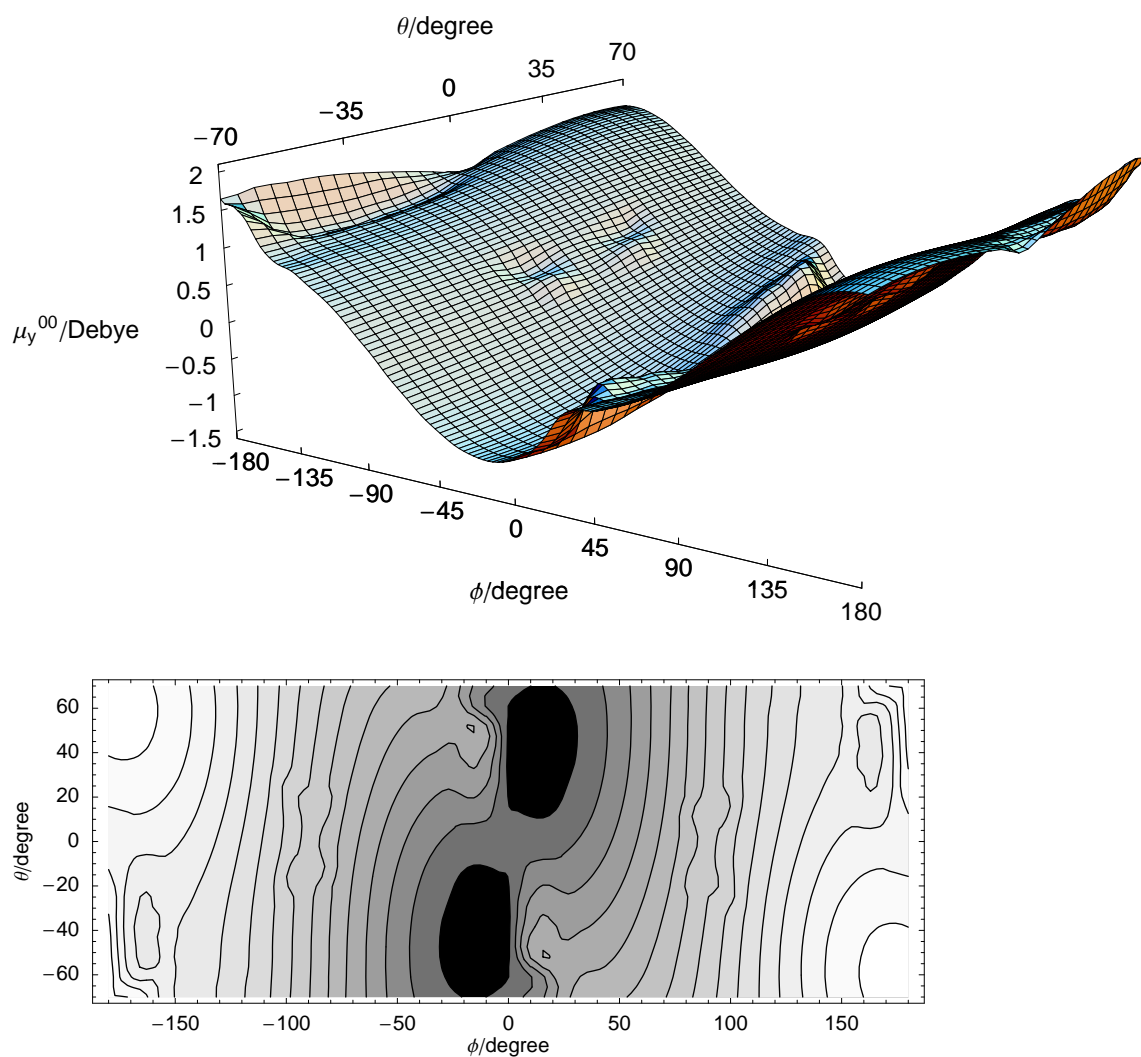
Figure 5.22: 2D-surface (top) and contour plot (bottom) of the z-component μ_z^{00} of the permanent dipole moment of 4-Me(C_6H_9)CHF as a function of the torsion angle ϕ and the pyramidalization angle θ, calculated at B3LYP/6-311+G(d,p) level of theory. Equicontour lines $\mu_z^{00}(\phi, \theta) = \mu_0 + i\Delta\mu$, i=1–16, μ_0/Debye = 0.217, $\Delta\mu$/Debye = 0.214.

Figure 5.23: 2D-surface (top) and contour plot (bottom) of the x-component μ_x^{01} of the electronic transition dipole moment of 4-Me(C_6H_9)CHF as a function of the torsion angle ϕ and the pyramidalization angle θ, calculated at B3LYP/6-311+G(d,p) level of theory. Equicontour lines $\mu_x^{01}(\phi, \theta) = \mu_0 + i\Delta\mu$, i=1–16, μ_0/Debye $= -0.368$, $\Delta\mu$/Debye $= 0.0460$.

Figure 5.24: 2D-surface (top) and contour plot (bottom) of the y-component μ_y^{01} of the electronic transition dipole moment of 4-Me(C_6H_9)CHF as a function of the torsion angle ϕ and the pyramidalization angle θ, calculated at B3LYP/6-311+G(d,p) level of theory. Equicontour lines $\mu_y^{01}(\phi, \theta) = \mu_0 + i\Delta\mu$, i=1–16, μ_0/Debye $= -0.649$, $\Delta\mu$/Debye $= 0.0416$.
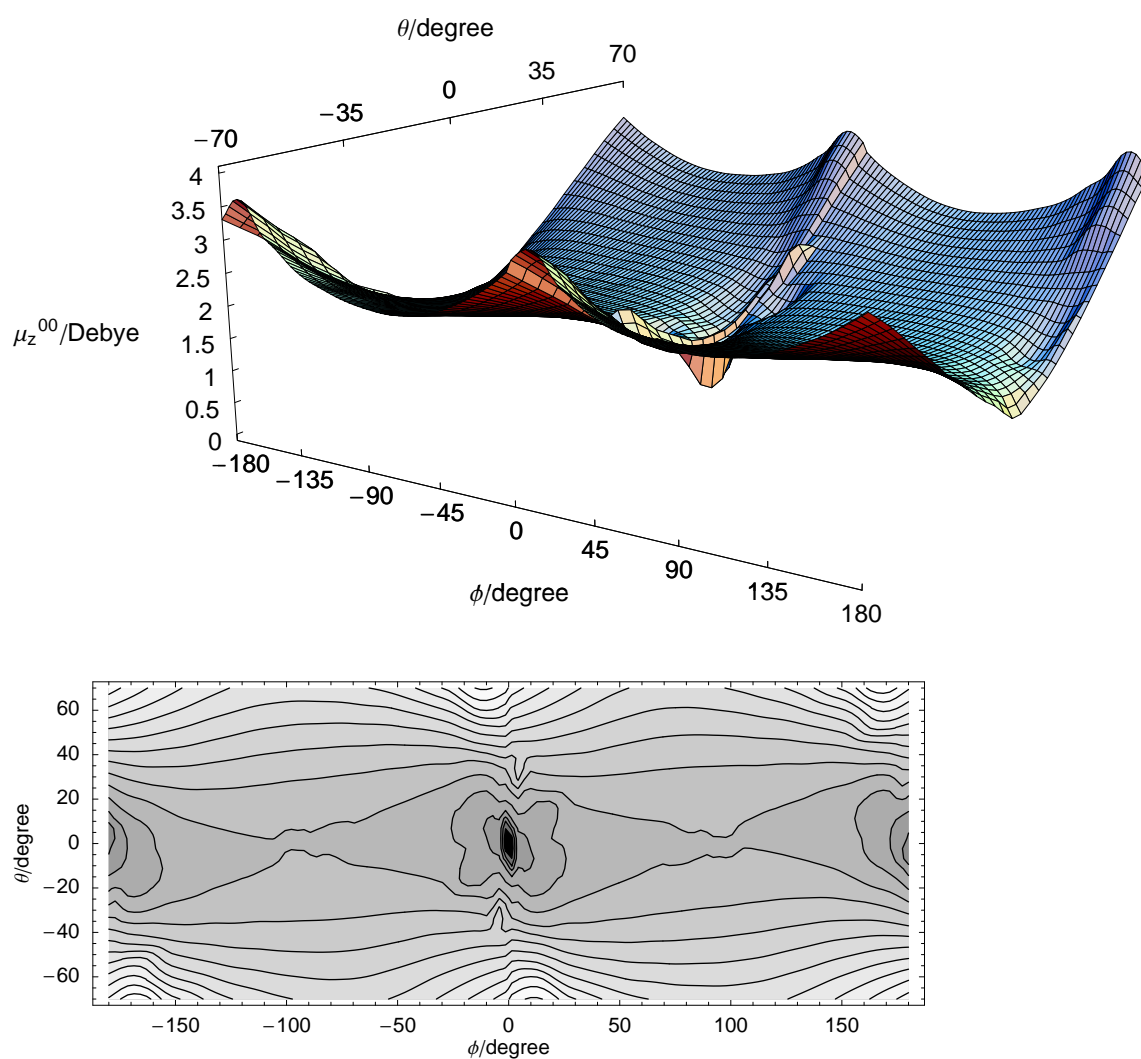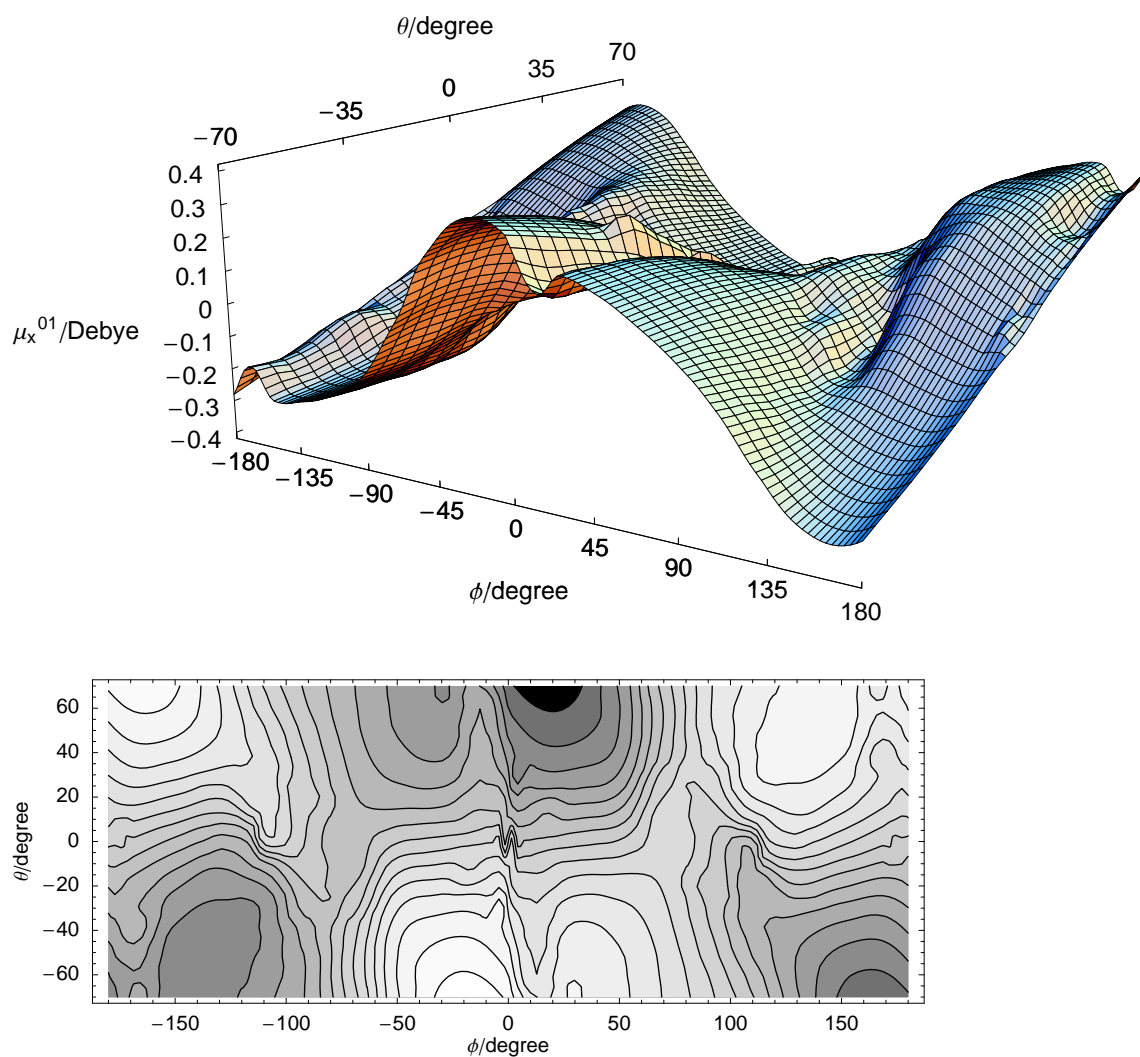
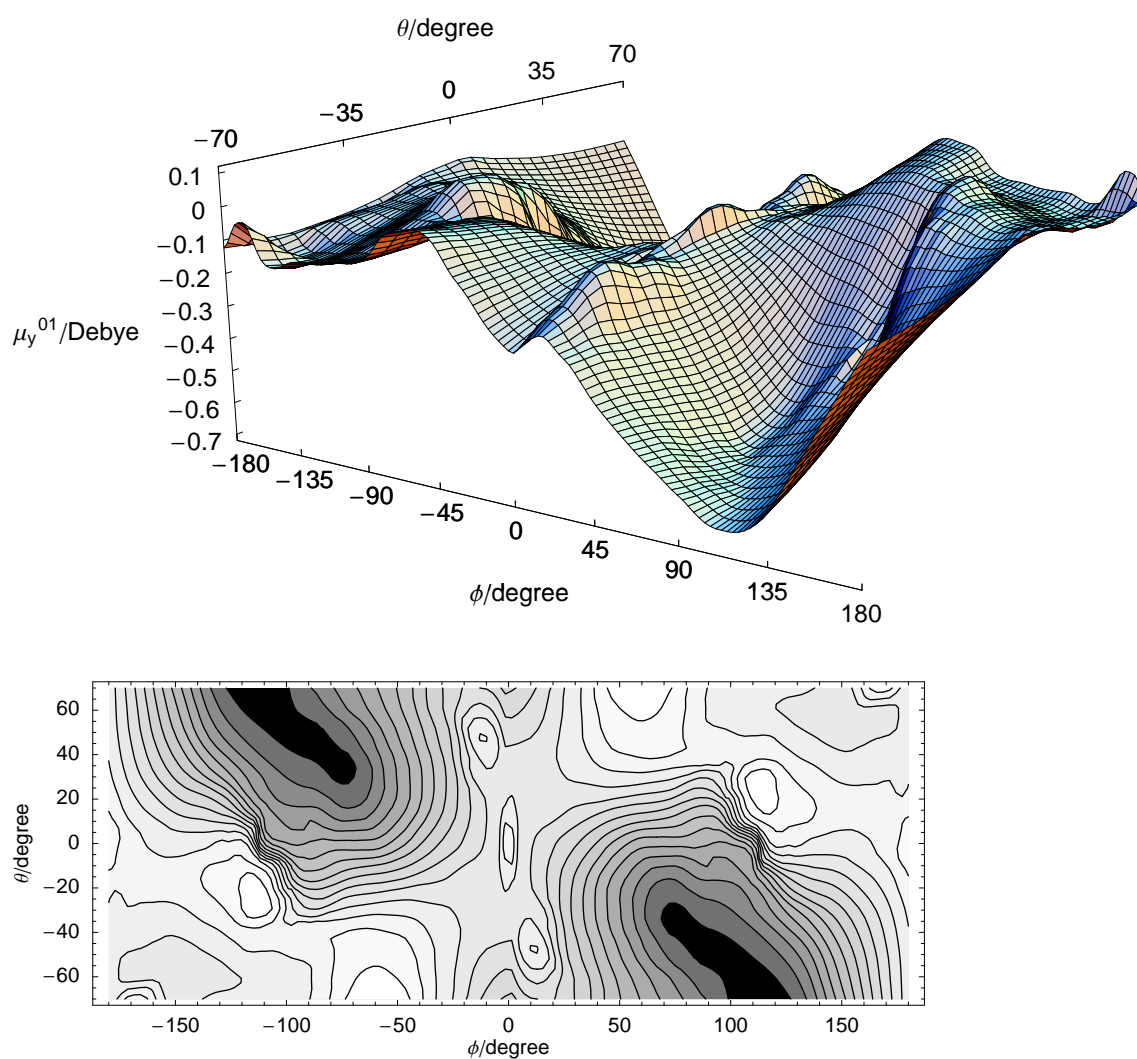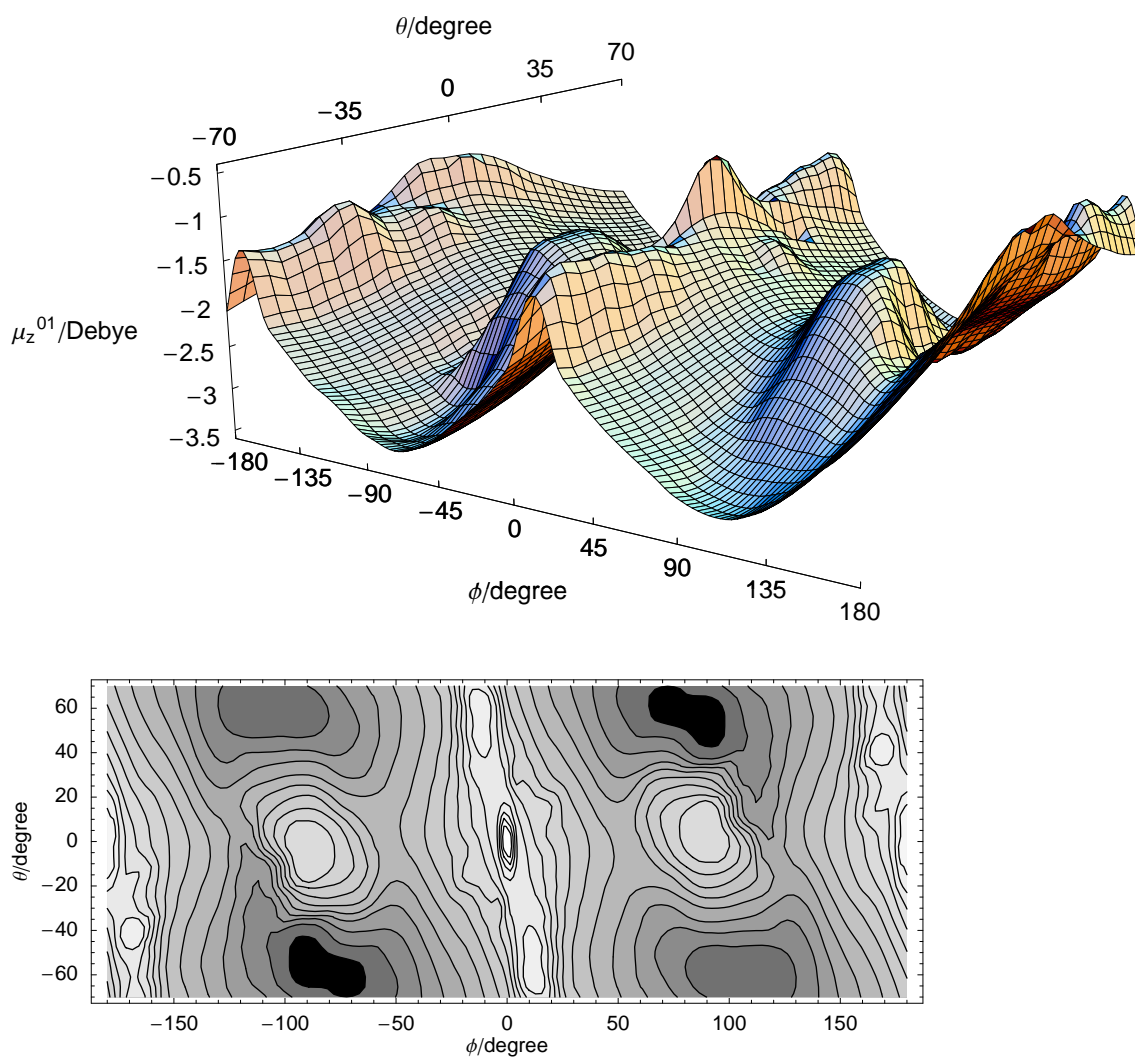Figure 5.25: 2D-surface (top) and contour plot (bottom) of the z-component μ_z^{01} of the electronic transition dipole moment of 4-Me(C_6H_9)CHF as a function of the torsion angle ϕ and the pyramidalization angle θ, calculated at B3LYP/6-311+G(d,p) level of theory. Equicontour lines $\mu_z^{01}(\phi, \theta) = \mu_0 + i\Delta\mu$, i=1–16, μ_0/Debye $= -3.422$, $\Delta\mu$/Debye $= 0.178$.

5.4.2   Derivation and eigenstates of the 2D-Hamiltonian for coupled torsion and pyramidalization

To obtain the eigenfunctions and eigenenergies for the torsion-pyramidalization the TISE has to be solved. The PES has been calculated along two degrees of freedom, i.e. the angles ϕ for the torsion and θ for the pyramidalization. It is convenient to express the kinetic energy operator also in terms of these curvilinear coordinates. This results in a complex expression for the kinetic operator of the Hamiltonian because torsion and pyramidalization are coupled degrees of freedom. In the following, the kinetic operator is derived.
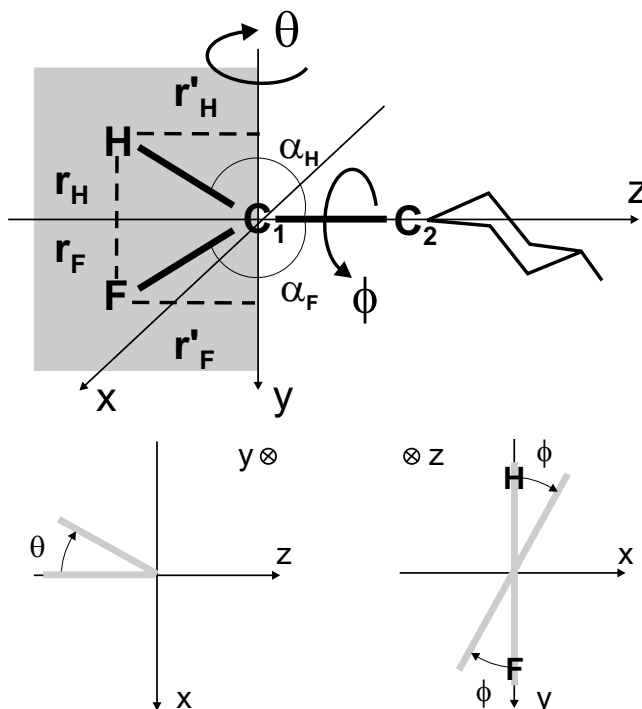
Figure 5.26: Sketch of the oriented molecule 4-Me(C_6H_9)CHF for $\phi = 0°, \theta = 0°$ in the laboratory fixed coordinate system (top) and a view in +y-direction (bottom left) and in +z-direction for defining the rotation angles θ and ϕ, cf. text. The torsional motion of H and F along ϕ is always around the $C_1=C_2$ double bond, and hence, around the space-fixed z-axis, independent of θ. The pyramidalization along θ is a rotation of H and F around an axis (previously called P) perpendicular to the z-axis. This axis goes through C_1 and lies in plane with H and F; therefore, its position depends on ϕ (for $\phi = 0°$ it is the y-axis). The symbol $\otimes$ represents a vector that is perpendicular to the page, pointing away from the reader.

First, the Cartesian coordinate vectors of the F and H atom of the pre-oriented molecule have to be expressed in terms of the angles ϕ and θ. The vectors $\vec{x}_F$ and $\vec{x}_H$ describe the F and H atom in the space-fixed coordinate system centered at C_1. For $\phi = 0°$ and $\theta = 0°$ F and H are in the yz-plane with F pointing in positive y-direction, as shown in figure 5.26; then $\vec{x}_F$ and $\vec{x}_H$ are given as:

$$\vec{x}_F = \begin{pmatrix} x_F \\ y_F \\ z_F \end{pmatrix} \overset{\phi=0°}{\underset{\theta=0°}{=}} \begin{pmatrix} 0 \\ R_{C_1F} \cdot \sin(180 - \alpha_F) \\ -R_{C_1F} \cdot \cos(180 - \alpha_F) \end{pmatrix} \equiv \begin{pmatrix} 0 \\ r_F \\ -r'_F \end{pmatrix} \qquad (5.16)$$

$$\vec{x}_H = \begin{pmatrix} x_H \\ y_H \\ z_H \end{pmatrix} \overset{\phi=0°}{\underset{\theta=0°}{=}} \begin{pmatrix} 0 \\ -R_{C_1H} \cdot \sin(180 - \alpha_H) \\ -R_{C_1H} \cdot \cos(180 - \alpha_H) \end{pmatrix} \equiv \begin{pmatrix} 0 \\ -r_H \\ -r'_H \end{pmatrix}, \qquad (5.17)$$

where R_{C_1F} and R_{C_1H} are the bond distances between the respective atoms and α_F and α_H are defined as the angles between the respective atom and the C=C double bond. To obtain a general expression of $\vec{x}_F$ and $\vec{x}_H$, for any angle ϕ and θ, the coordinates in equations (5.16) and (5.17) are transformed first by a clockwise rotation around the y-axis and then by a clockwise rotation around the z-axis, as shown in fig. 5.26:

$$\begin{aligned} \vec{x}_F &= \begin{pmatrix} \cos\phi & -\sin\phi & 0 \\ \sin\phi & \cos\phi & 0 \\ 0 & 0 & 1 \end{pmatrix} \cdot \begin{pmatrix} \cos\theta & 0 & \sin\theta \\ 0 & 1 & 0 \\ -\sin\theta & 0 & \cos\theta \end{pmatrix} \cdot \begin{pmatrix} 0 \\ r_F \\ -r'_F \end{pmatrix} \\ &= \begin{pmatrix} -r_F \sin\phi - r'_F \cos\phi \sin\theta \\ r_F \cos\phi - r'_F \sin\phi \sin\theta \\ -r'_F \cos\theta \end{pmatrix} \end{aligned} \qquad (5.18)$$

$$\begin{aligned} \vec{x}_H &= \begin{pmatrix} \cos\phi & -\sin\phi & 0 \\ \sin\phi & \cos\phi & 0 \\ 0 & 0 & 1 \end{pmatrix} \cdot \begin{pmatrix} \cos\theta & 0 & \sin\theta \\ 0 & 1 & 0 \\ -\sin\theta & 0 & \cos\theta \end{pmatrix} \cdot \begin{pmatrix} 0 \\ -r_H \\ -r'_H \end{pmatrix} \\ &= \begin{pmatrix} r_H \sin\phi - r'_H \cos\phi \sin\theta \\ -r_H \cos\phi - r'_H \sin\phi \sin\theta \\ -r'_H \cos\theta \end{pmatrix}. \end{aligned} \qquad (5.19)$$

The torsional angle ϕ, measured from the space-fixed y-axis, is defined for $-\pi \leq \phi \leq \pi$; ϕ is positive for a clockwise rotation around the z-axis. The angle for pyramidalization θ, measured from the space-fixed z-axis, is defined for $-\pi \leq \theta \leq \pi$; θ is positive for a clockwise rotation around the y-axis for $\phi = 0°$. The vectors $\vec{x}_F$ and $\vec{x}_H$ in eqns. (5.18) and (5.19) are functions of the angles ϕ and θ and represent the bonds between the respective atom and the center of the Cartesian coordinate system at C_1.

The kinetic operator of the molecular Hamiltonian for 4-Me(C_6H_9)CHF is derived from the formalism used by Luckhaus for torsion-inversion dynamics in hydroxylamine

[154]. The derivation of this formalism for a general internal motion of molecules can be found in the work of Meyer and Günthard [155, 156]. The Hamiltonian used by Luckhaus is given as [154]:[11]

$$\hat{\mathbf{H}} = \frac{1}{2}(\hat{\mathbf{J}}^{\top}, \hat{\mathbf{p}}^{\top}) \begin{pmatrix} \mathbf{I} & \mathbf{C} \\ \mathbf{C}^{\top} & \mathbf{g} \end{pmatrix}^{-1} \begin{pmatrix} \hat{\mathbf{J}} \\ \hat{\mathbf{p}} \end{pmatrix} + u(q_1, q_2, ...) + V(q_1, q_2, ...), \quad (5.20)$$

$$I_{\alpha\beta} = \sum_a m_a (\vec{e}_\alpha \times \vec{x}_a)(\vec{e}_\beta \times \vec{x}_a),$$

$$C_{\alpha j} = \sum_a m_a (\vec{e}_\alpha \times \vec{x}_a)\frac{\partial \vec{x}_a}{\partial q_j}, \quad (5.21)$$

$$g_{jk} = \sum_a m_a \frac{\partial \vec{x}_a}{\partial q_j} \cdot \frac{\partial \vec{x}_a}{\partial q_k}, \quad (5.22)$$

$$(\hat{\mathbf{J}}^{\top}, \hat{\mathbf{p}}^{\top}) = (\hat{J}_x, \hat{J}_y, \hat{J}_z, \hat{p}_1, \hat{p}_2, ...), \quad (5.23)$$

for generalized vibrational coordinates q_j with momenta $\hat{p}_j = -i\hbar(\partial/\partial q_j)$. In equation (5.20) the tensor consists of the tensor of inertia $\mathbf{I}$ with elements $I_{\alpha\beta}$, the Coriolis coupling matrix $\mathbf{C}$ with elements $C_{\alpha j}$ and its transpose $\mathbf{C}^{\top}$, and the matrix $\mathbf{g}$ with elements g_{jk}. $\hat{\mathbf{J}}$ is the total angular momentum operator, $\vec{e}_\alpha (\alpha = x, y, z)$ are the unit vectors along the coordinate axes, and $\vec{x}_a$ is the Cartesian coordinate vector of the atom a, all referring to the molecule fixed center of mass coordinate system. V is the potential energy in terms of the coordinates q_j and u is the pseudo potential, a 'purely quantum mechanical' mass-dependent contribution to the potential energy[12].

In the system 4-Me(C_6H_9)CHF the cyclohexane ring including the methyl substituent is much heavier than the F and H atom at C_1, hence, the molecule can be approximated to be fixed while F and H undergo torsion and pyramidalization. For an infinite heavy molecular frame the tensor of inertia $\mathbf{I}$ becomes infinite and the rotational blocks $\mathbf{I}$ and $\mathbf{C}$ can be neglected; then, equation (5.20) simplifies to

$$\hat{\mathbf{H}} = \frac{1}{2}\hat{\mathbf{p}}^{\top}\mathbf{g}^{-1}\hat{\mathbf{p}} + u(q_1, q_2, ...) + V(q_1, q_2, ...) \quad (5.24)$$

with the pseudo potential u given as

$$u(q_1, q_2, ...) = \frac{\hbar^2}{2} \sum_{j,k} \frac{1}{4} \cdot \frac{\partial}{\partial q_j} \left\{ \mathbf{g}_{jk}^{-1} \cdot \frac{\partial \ln(|\mathbf{g}|)}{\partial q_k} \right\} + \quad (5.25)$$

$$\frac{1}{16} \cdot \frac{\partial \ln(|\mathbf{g}|)}{\partial q_j} \cdot \mathbf{g}_{jk}^{-1} \cdot \frac{\partial \ln(|\mathbf{g}|)}{\partial q_k}, \quad (5.26)$$

---

[11]Note that in formula (9) of ref. [154] the units of $\hat{\mathbf{H}}$ are not given correctly and u is missing the factor $\hbar^2/2$.

[12]For a derivation of the pseudo potential see e.g. ref. [157].

where $|\mathbf{g}|$ is the determinant of the matrix $\mathbf{g}$ and $\mathbf{g}_{jk}^{-1}$ are the elements of the inverse matrix. Then, the molecular Hamilton operator for torsion-pyramidalization of the CFH-group for each electronic state i reads as follows

$$\hat{\mathbf{H}} = \frac{1}{2}\left(\hat{p}_\phi, \hat{p}_\theta\right)\mathbf{g}^{-1}\begin{pmatrix} \hat{p}_\phi \\ \hat{p}_\theta \end{pmatrix} + u(\phi, \theta) + V_i(\phi, \theta), \tag{5.27}$$

where $\mathbf{g}$ and $\mathbf{g}^{-1}$ are defined as

$$\mathbf{g} = \begin{pmatrix} g_{\phi\phi} & g_{\phi\theta} \\ g_{\theta\phi} & g_{\theta\theta} \end{pmatrix}, \tag{5.28}$$

$$\mathbf{g}^{-1} = \begin{pmatrix} g^{\phi\phi} & g^{\phi\theta} \\ g^{\theta\phi} & g^{\theta\theta} \end{pmatrix}, \tag{5.29}$$

and

$$\hat{p}_\phi = -i\hbar\frac{\partial}{\partial\phi}, \tag{5.30}$$

$$\hat{p}_\theta = -i\hbar\frac{\partial}{\partial\theta}. \tag{5.31}$$

The elements of the matrix $\mathbf{g}$ are obtained applying eqn. (5.22) for the Cartesian coordinate vectors $\vec{x}_F$ and $\vec{x}_H$, which refer to the molecule fixed center of mass coordinate system[13] centered at C_1, as depicted in fig. 5.26:

$$\begin{aligned} g_{\phi\phi} &= m_F\frac{\partial\vec{x}_F}{\partial\phi}\cdot\frac{\partial\vec{x}_F}{\partial\phi} + m_H\frac{\partial\vec{x}_H}{\partial\phi}\cdot\frac{\partial\vec{x}_H}{\partial\phi} \\ &= m_F r_F^2 + m_H r_H^2 + (m_F r_F'^2 + m_H r_H'^2)\sin^2\theta \end{aligned} \tag{5.32}$$

$$\begin{aligned} g_{\phi\theta} &= m_F\frac{\partial\vec{x}_F}{\partial\phi}\cdot\frac{\partial\vec{x}_F}{\partial\theta} + m_H\frac{\partial\vec{x}_H}{\partial\phi}\cdot\frac{\partial\vec{x}_H}{\partial\theta} = \\ g_{\theta\phi} &= m_F\frac{\partial\vec{x}_F}{\partial\theta}\cdot\frac{\partial\vec{x}_F}{\partial\phi} + m_H\frac{\partial\vec{x}_H}{\partial\theta}\cdot\frac{\partial\vec{x}_H}{\partial\phi} \\ &= (m_F r_F r_F' - m_H r_H r_H')\cos\theta \end{aligned} \tag{5.33}$$

$$\begin{aligned} g_{\theta\theta} &= m_F\frac{\partial\vec{x}_F}{\partial\theta}\cdot\frac{\partial\vec{x}_F}{\partial\theta} + m_H\frac{\partial\vec{x}_H}{\partial\theta}\cdot\frac{\partial\vec{x}_H}{\partial\theta} \\ &= m_F r_F'^2 + m_H r_H'^2 \end{aligned} \tag{5.34}$$

---

[13]Since the molecule is considered to be fixed in space at the C_1 atom, molecule fixed and space fixed coordinate system are the same in terms of the vectors $\vec{x}_F$ and $\vec{x}_H$.

For the elements of the inverted matrix $\mathbf{g}^{-1}$ the following four terms are derived:

$$g^{\phi\phi} = \frac{1}{|\mathbf{g}|} \cdot (m_F r_F'^2 + m_H r_H'^2) \tag{5.35}$$

$$g^{\phi\theta} = g^{\theta\phi} = -\frac{1}{|\mathbf{g}|} \cdot (m_F r_F r_F' - m_H r_H r_H') \cos\theta \tag{5.36}$$

$$g^{\theta\theta} = \frac{1}{|\mathbf{g}|} \cdot (m_F r_F^2 + m_H r_H^2 + (m_F r_F'^2 + m_H r_H'^2) \sin^2\theta) \tag{5.37}$$

with the determinant $|\mathbf{g}|$ being

$$\begin{aligned}
|\mathbf{g}| = {} & m_F^2 r_F^2 r_F'^2 + m_F m_H r_F'^2 r_H^2 + m_F m_H r_F^2 r_H'^2 + m_H^2 r_H^2 r_H'^2 \\
& - (m_F r_F r_F' - m_H r_H r_H')^2 \cos^2\theta + (m_F r_F'^2 + m_H r_H'^2)^2 \sin^2\theta
\end{aligned} \tag{5.38}$$

It is interesting to note that the coupling term $g^{\phi\theta}$ disappears in the case of two identical substituents at C_1, e.g. in ethylene. The coupling term $g^{\phi\theta}$ also vanishes for $\theta = \pm 90°$, but it is maximal at the equilibrium configuration $\theta = 0°$.

The derivation of the pseudo potential u was performed using the software package *Mathematica 3.0* [158]. Since $|\mathbf{g}|$ does not depend on ϕ, all terms of the pseudo potential with derivatives $\partial/\partial\phi$ of the determinant become zero and u simplifies to

$$u(\theta) = \frac{\hbar^2}{8} \cdot \frac{\partial}{\partial\theta} \left(g^{\theta\theta} \frac{\partial \ln|\mathbf{g}|}{\partial\theta} \right) + \frac{\hbar^2}{32} \frac{\partial \ln|\mathbf{g}|}{\partial\theta} g^{\theta\theta} \frac{\partial \ln|\mathbf{g}|}{\partial\theta}. \tag{5.39}$$

parameter	value
$R_{C_1 F}$	1.3552 Å
$R_{C_1 H}$	1.0849 Å
α_F	122.30°
α_H	125.48°
m_F	18.998 amu
m_H	1.0080 amu

Table 5.5: Geometric parameters (from MP2/6-311G(d,p)) used to calculate $\mathbf{g}^{-1}$ and u.

For the numerical simulations it is convenient to present $\mathbf{g}^{-1}$ and u in terms of the geometric parameters of 4-Me(C_6H_9)CHF. In table 5.5 the bond distances and angles, as obtained from the geometry optimization (see section 5.3.2), are listed. With the

calculated distances (in at. un., i.e. in a_0)

$$
\begin{align}
r_F &= R_{C_1F} \cdot \sin(180° - \alpha_F) = 2.165, \tag{5.40}\\
r'_F &= R_{C_1F} \cdot \cos(180° - \alpha_F) = 1.368, \tag{5.41}\\
r_H &= R_{C_1H} \cdot \sin(180° - \alpha_H) = 1.669, \tag{5.42}\\
r'_H &= R_{C_1H} \cdot \cos(180° - \alpha_H) = 1.190, \tag{5.43}
\end{align}
$$

the matrix elements (in at. un., i.e. in $\frac{1}{m_e a_0^2}$) are:

$$
g^{\phi\phi} = \frac{1}{|\mathbf{g}|} \cdot 67442 \tag{5.44}
$$

$$
g^{\phi\theta} = g^{\theta\phi} = -\frac{1}{|\mathbf{g}|} \cdot 98928 \cos\theta \tag{5.45}
$$

$$
g^{\theta\theta} = \frac{1}{|\mathbf{g}|} \cdot (167404 + 67442 \sin^2\theta) \tag{5.46}
$$

with the determinant $|\mathbf{g}|$ (in at. un., i.e. in $m_e^2 a_0^4$)

$$
|\mathbf{g}| = 1.1290 \cdot 10^{10} - 98928^2 \cdot \cos^2\theta + 67442^2 \cdot \sin^2\theta, \tag{5.47}
$$

and the pseudo potential (in at. un., i.e. in E_h):

$$
u(\theta) = \frac{-71.037 + 70.619 \cdot \cos(2\theta) + 8.8951 \cdot \cos(4\theta) + 0.54137 \cdot \cos(6\theta)}{(1.1290 \cdot 10^{10} - 98930^2 \cdot \cos^2(\theta) + 67444^2 \cdot \sin^2(\theta))^3} \cdot 10^{23}. \tag{5.48}
$$

In figure 5.27 the pseudo potential is plotted as a function of the pyramidalization angle θ; u is constant with respect to the torsional angle ϕ. For the numerical solution of the Schrödinger equation the pseudo potential is added to each potential $V_i(\phi, \theta)$. The effect of u on the PES is rather small ($1E_h \approx 200000$ cm^{-1}).
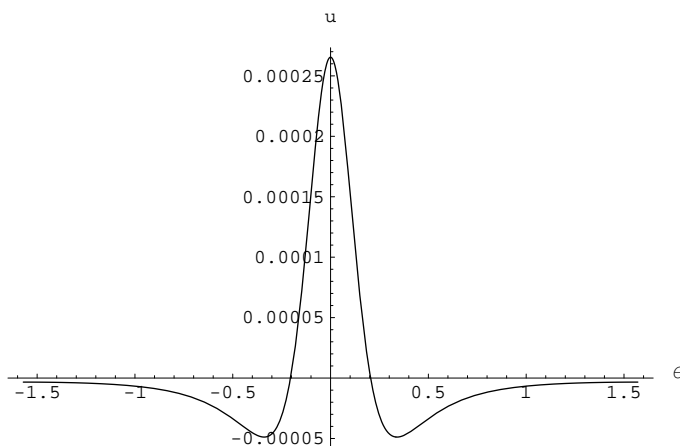

Figure 5.27: Pseudo-potential u as described in equation (5.48) for $-\pi/2 \leq \theta \leq +\pi/2$, in E_h.

From eqn. 5.27 one obtains for the kinetic operator the following expression:

$$\hat{\mathbf{T}} = \frac{1}{2}\left(\hat{p}_\phi g^{\phi\phi}\hat{p}_\phi + \hat{p}_\phi g^{\phi\theta}\hat{p}_\theta + \hat{p}_\theta g^{\theta\phi}\hat{p}_\phi + \hat{p}_\theta g^{\theta\theta}\hat{p}_\theta\right).$$

In $\hat{\mathbf{T}}$ the factors g^{jk} do not commute with the partial kinetic energy operator $\hat{p}_\theta$ because all g^{jk} depend on the angle θ. Therefore, the split operator method discussed in section 2.3.2 cannot be applied to solve the Schrödinger equation, and the second order differencing (SOD) method (see section 2.3.3) is used. The action of the partial kinetic operator on the wave function $\Psi(\phi, \theta)$ has to be evaluated in momentum space, while the action of the factors g^{ij} on Ψ is determined in position space. Hence, several Fourier transformations (FT) are needed to evaluate the kinetic operator for a given wave function. The following scheme has been applied:

1. FT of the total wave function $\Psi(\phi, \theta)$ to momentum space:

$$\Psi(\phi, \theta) \xrightarrow{FT} \Psi(p_\phi, p_\theta) \tag{5.49}$$

2. Duplication of the wave function $\Psi(p_\phi, p_\theta)$ to two separated wave functions:

$$\Psi(p_\phi, p_\theta) \nearrow \Psi_\phi(p_\phi, p_\theta) \searrow \Psi_\theta(p_\phi, p_\theta) \tag{5.50}$$

3. Calculation of the action of $\hat{p}_j$ on $\Psi_j(p_\phi, p_\theta)$ in momentum space:

$$\hat{p}_\phi \Psi_\phi(p_\phi, p_\theta) = \Psi'_\phi(p_\phi, p_\theta) \tag{5.51}$$
$$\hat{p}_\theta \Psi_\theta(p_\phi, p_\theta) = \Psi'_\theta(p_\phi, p_\theta) \tag{5.52}$$

4. Inverse FT of $\Psi'_j(p_\phi, p_\theta)$ to position space:

$$\Psi'_\phi(p_\phi, p_\theta) \xrightarrow{iFT} \Psi'_\phi(\phi, \theta) \tag{5.53}$$
$$\Psi'_\theta(p_\phi, p_\theta) \xrightarrow{iFT} \Psi'_\theta(\phi, \theta) \tag{5.54}$$

5. Calculation of the action of all matrix elements g^{jk} on $\Psi'_j(p_\phi, p_\theta)$ in position space:

$$g^{\phi\phi}\Psi'_\phi(\phi, \theta) + g^{\phi\theta}\Psi'_\theta(\phi, \theta) = \Psi_{\phi\theta}(\phi, \theta) \tag{5.55}$$
$$g^{\theta\phi}\Psi'_\phi(\phi, \theta) + g^{\theta\theta}\Psi'_\theta(\theta, \theta) = \Psi_{\theta\phi}(\phi, \theta) \tag{5.56}$$

6. FT of $\Psi_{jk}(\phi,\theta)$ to momentum space:

$$\Psi_{\phi\theta}(\phi,\theta) \quad \xrightarrow{FT} \quad \Psi_{\phi\theta}(p_\phi,p_\theta) \tag{5.57}$$

$$\Psi_{\theta\phi}(\phi,\theta) \quad \xrightarrow{FT} \quad \Psi_{\theta\phi}(p_\phi,p_\theta) \tag{5.58}$$

7. Calculation of the action of $\hat{p}_j$ on $\Psi_{jk}(p_\phi,p_\theta)$ in momentum space:

$$\hat{p}_\phi\Psi_{\phi\theta}(p_\phi,p_\theta) \; = \; \Psi'_{\phi\theta}(p_\phi,p_\theta) \tag{5.59}$$

$$\hat{p}_\theta\Psi_{\theta\phi}(p_\phi,p_\theta) \; = \; \Psi'_{\theta\phi}(p_\phi,p_\theta) \tag{5.60}$$

8. Inverse FT of $\Psi'_{jk}(p_\phi,p_\theta)$ to position space:

$$\Psi'_{\phi\theta}(p_\phi,p_\theta) \quad \xrightarrow{iFT} \quad \Psi'_{\phi\theta}(\phi,\theta) \tag{5.61}$$

$$\Psi'_{\theta\phi}(p_\phi,p_\theta) \quad \xrightarrow{iFT} \quad \Psi'_{\theta\phi}(\phi,\theta) \tag{5.62}$$

9. Summation of the wave functions $\Psi'_{jk}(\phi,\theta)$ to obtain the total wave function in position space:

$$\Psi'(\phi,\theta) = \frac{1}{2}\left(\Psi'_{\phi\theta}(\phi,\theta) + \Psi'_{\theta\phi}(\phi,\theta)\right) \tag{5.63}$$

In position space the action of the potential energy operator $\hat{\mathbf{V}}_i\ (= V_i(\phi,\theta) + u(\theta))$ of the electronic state i has to be calculated by multiplication with the wave function $\Psi(\phi,\theta)$. Then the effect of the complete Hamiltonian on the total wave function is obtained. Altogether, seven Fourier transformations are necessary.

The solution of the TISE yields the eigenenergies and two-dimensional eigenfunctions. The numerical solution was obtained by the FGH method [131] (section 2.2.8) using a total of 4096 grid points, i.e. 128 grid points along ϕ and 32 along θ. Eigenenergies and eigenfunctions which are important for the dynamical simulations are listed in table 5.6 and shown as contour plots in figure 5.28, respectively. The energetically low eigenfunctions of the electronic ground state S$_0$ can be distinguished in terms of the two degrees of freedom. They are labeled by two quantum numbers $\left|\Phi^0_{vw(g/u)}\right\rangle$ with $v = 0, 1, 2, ...$ for the torsional degree of freedom and $w = 0, 1, 2, ...$ for the pyramidalization. The symmetry of the eigenfunctions with respect to the center of inversion at $\phi = 0°, \theta = 0°$ is denoted by g for symmetric functions and u for anti-symmetric functions. The eigenstates of S$_1$ $\left|\Phi^1_{v'(g/u)}\right\rangle$ are denoted by a single quantum number v', since a distinction between torsional and pyramidalizational degree of freedom is not possible for energetically high lying

states[14]. The localized functions corresponding to the L- and R-enantiomer are defined analogously to those of the one-dimensional model system:

$$|\Psi_{vwL}\rangle = \frac{1}{\sqrt{2}}\left(\left|\Phi_{vwg}^0\right\rangle + \left|\Phi_{vwu}^0\right\rangle\right) \tag{5.64}$$

$$|\Psi_{vwR}\rangle = \frac{1}{\sqrt{2}}\left(\left|\Phi_{vwg}^0\right\rangle - \left|\Phi_{vwu}^0\right\rangle\right). \tag{5.65}$$

For the eigenfunctions $\left|\Phi_{vw(g/u)}^0\right\rangle$ shown in fig. 5.28 the corresponding localized functions $\left|\Psi_{vw(L/R)}\right\rangle$ are depicted in figure 5.29. As in the one-dimensional case doublets of eigenstates are formed in both potential wells of V_0. Since the energy splittings of the first 50 doublets is smaller than the numerical error, no tunneling times can be computed. A pure enantiomer is stable even at room temperature, cf. section 5.

eigenstate $vw(g/u)$	energy [cm^{-1}]	eigenstate $vw(g/u)$	energy [cm^{-1}]
00g	493.408	01g	1240.65
00u	493.408	01u	1240.65
10g	622.911	60g	1280.19
10u	622.911	60u	1280.19
20g	756.731	11g	1376.20
20u	756.731	11u	1376.20
30g	887.194	70g	1410.40
30u	887.194	70u	1410.40
40g	1017.81	21g	1506.98
40u	1017.81	21u	1506.98
50g	1149.44	80g	1542.31
50u	1149.44	80u	1542.31

Table 5.6: Eigenenergies of the first 22 torsion-pyramidalization states of the S_0 state of 4-Me(C_6H_9)CHF. The eigenstates are denoted by the first quantum numbers v for the torsion and second quantum numbers w for the pyramidalization; g and u are used for the symmetry with respect to the center of inversion at $\phi = \theta = 0°$. The corresponding eigenfunctions of selected states are shown in figure 5.28.

---

[14]The energetically low lying eigenstates would be labeled in accordance with the electronic ground state as $\left|\Phi_{vw(g/u)}^1\right\rangle$, but they do not play any role in the dynamical simulations.
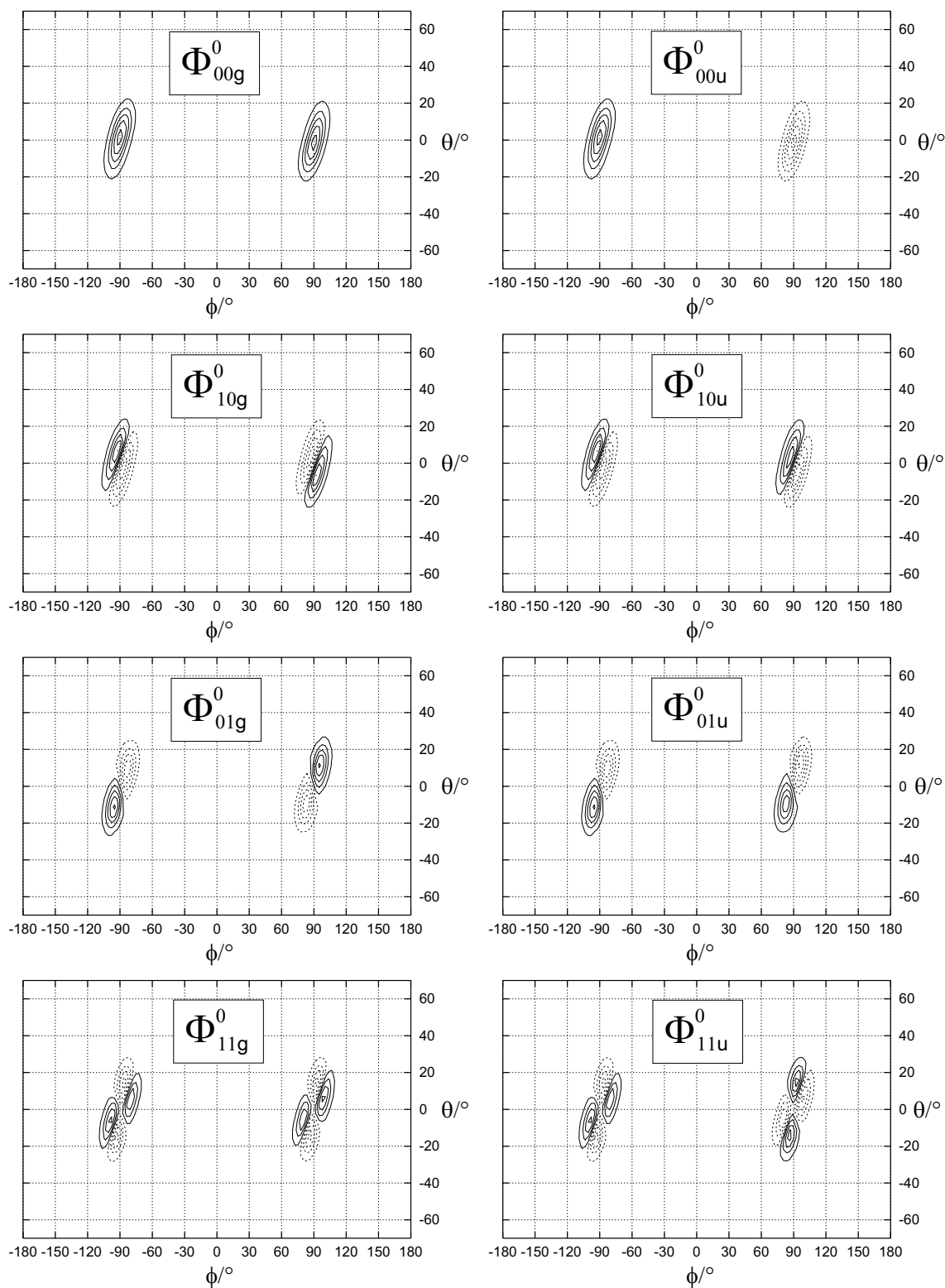
Figure 5.28: Contour plots of the eigenfunctions $\left| \Phi^0_{vw(g/u)} \right\rangle$ of V_0 for the 2D-model 4-Me(C$_6$H$_9$)CHF. The first quantum number v corresponds to the torsion along ϕ, the second quantum number w denotes the pyramidalization along θ, g/u denotes the symmetry with respect to $\phi = \theta = 0°$.
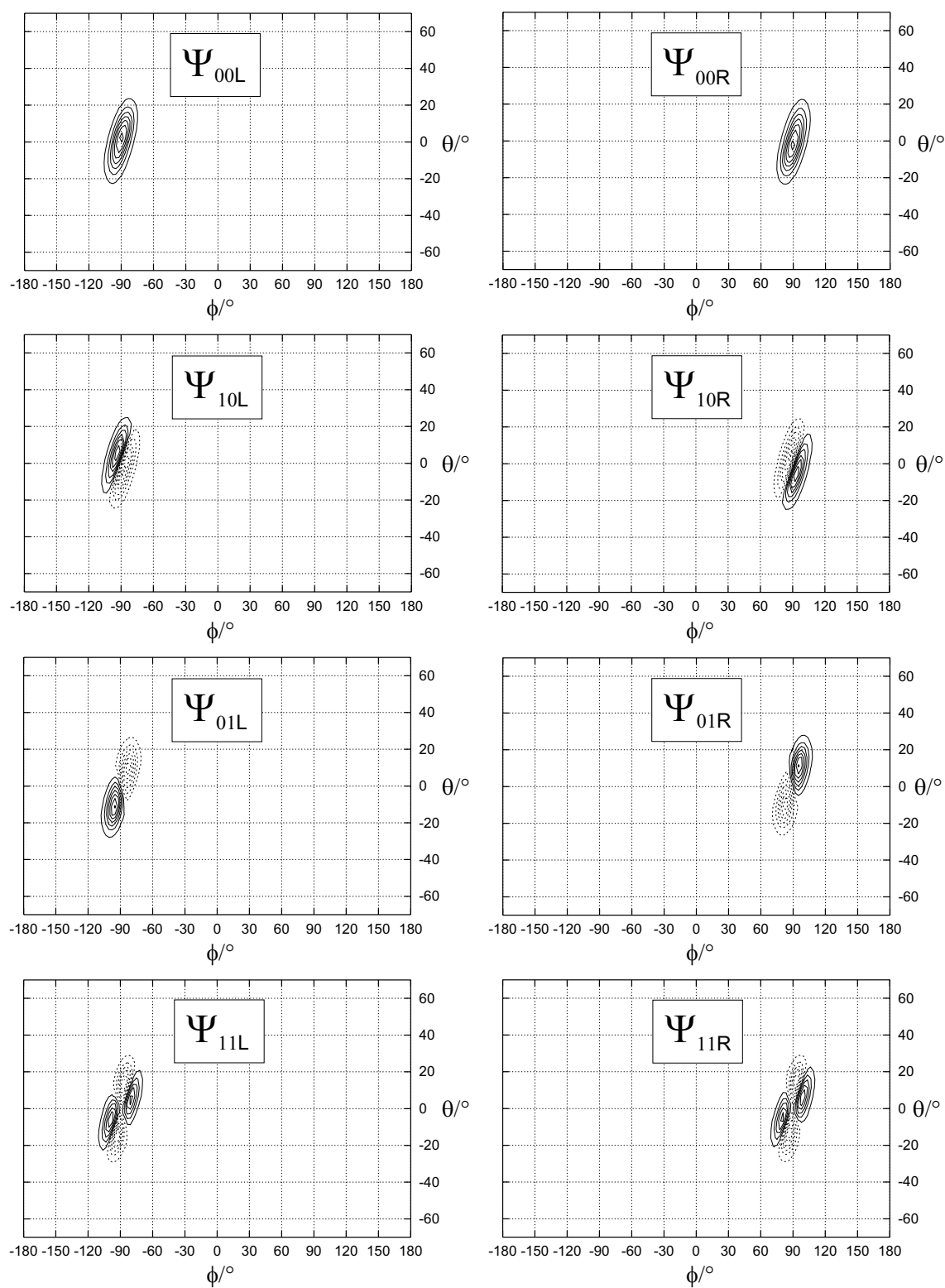
Figure 5.29: Contour plots of the localized functions $\left|\Psi_{vw(L/R)}\right\rangle$ of V_0 for the 2D-model 4-Me(C_6H_9)CHF as defined in eqns. (5.64) and (5.65). The first quantum number v corresponds to the torsion along ϕ, the second quantum number w denotes the pyramidalization along θ.

5.4.3   2D-dynamics using IR and UV laser pulses

The goal of the following laser control is to break the energetic degeneracy of both enantiomers of the racemate by exciting selectively one stereoisomer to the electronic excited state. Here the same laser control strategies as used for the 1D model shall be applied introducing modifications due to the second degree of freedom, i.e. the pyramidalization. The pyramidalization does not directly convert one chiral form into the other and hence, enantio-selectivity could be reduced by exciting this degree of freedom. Nevertheless, the pyramidalization allows an alternative path for an IR excitation possibly overcoming the problem of the harmonicity of the PES along the torsional degree of freedom. In the following, a modified laser control mechanism taking advantage of the pyramidalizational degree of freedom is presented.

At initial time $t = 0$ ps the system is prepared in the lowest doublet of eigenstates as an incoherent mixture of the L- and R-enantiomer corresponding to a racemic mixture (cf. section 5.3.3):

$$\rho(t = 0) = \frac{1}{2}\rho_{00L} + \frac{1}{2}\rho_{00R}. \tag{5.66}$$

Note that this low temperature approximation is still valid even though the temperature must be lower than in the 1D case because the energy gap to the first excited doublet is smaller for the 2D than for the 1D model system (130 cm^{-1} vs. 190 cm^{-1}), i.e. the coupling with the pyramidalization decreases the energy differences between the torsional doublets in the 2D model.

All the following dynamical simulations solving the TDSE have been carried out on a grid of 4096 points using the SOD propagation scheme, as implemented in *qmpropa* [133], with a time step of 0.01 fs. Figure 5.30 shows a sequence of two pump pulses that selectively excite the L-enantiomer to the electronic excited state S$_1$. The first pump pulse is designed to induce population transfer from $|\Psi_{00L}\rangle$ to $|\Psi_{01L}\rangle$, i.e. to excite one quantum of pyramidalization in the L-enantiomer. Because of the harmonicity of the potential V_0 in the regime of energetically low *torsional* eigenstates, an excitation to the first excited torsional doublet $|\Psi_{10L}\rangle$ would cause the wave packet to climb the ladder of torsional eigenstates creating a travelling wave packet, as in the one-dimensional model simulations, making laser control more demanding (see discussion in section 5.3.3). After the IR excitation, the L- and R-enantiomers are no longer degenerate. A subsequent enantio-selective UV laser pulse pumps the L-enantiomer to the electronic excited state S$_1$ with no effect on the R-enantiomer. The parameters of this pulse were initially adjusted to transfer all population from $|\Psi_{01L}\rangle$ selectively to the target state $\left|\Phi^1_{1384g}\right\rangle$. This target state was chosen because the transition dipole elements $|\left\langle\Phi^0_{01g}\right|\mu^{01}_x\left|\Phi^1_{1384g}\right\rangle|$ and $|\left\langle\Phi^0_{01u}\right|\mu^{01}_z\left|\Phi^1_{1384g}\right\rangle|$ are large compared to neighbouring states in S$_1$. Still, after further optimization the UV

laser pulse transfers population also to other torsion-pyramidalization states in V_1, such as $\left|\Phi^1_{1376g}\right\rangle$, $\left|\Phi^1_{1354g}\right\rangle$, $\left|\Phi^1_{1364g}\right\rangle$, $\left|\Phi^1_{1391u}\right\rangle$, $\left|\Phi^1_{1369g}\right\rangle$ and $\left|\Phi^1_{1382u}\right\rangle$ (listed in decreasing amount of population), as well as others which have 1% or less of the population.
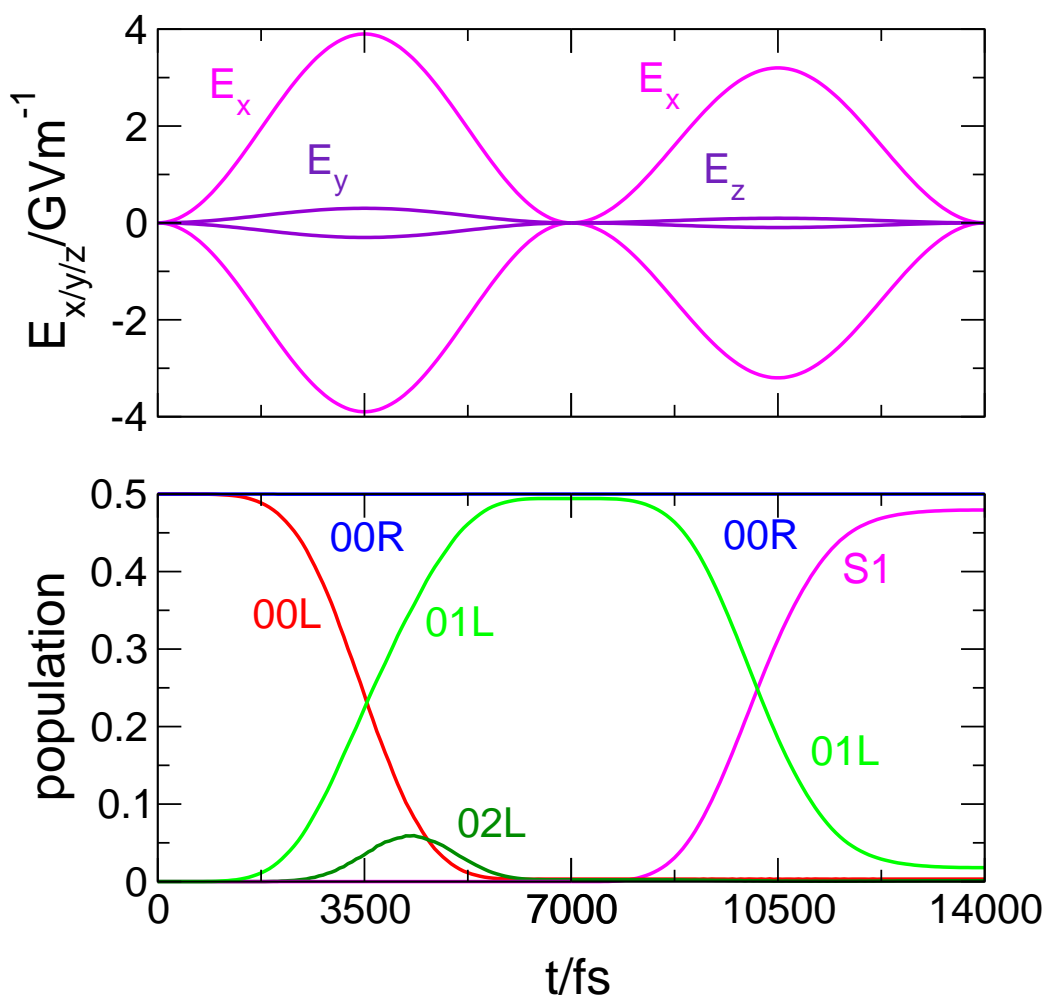
Figure 5.30: Asymmetric excitation of the L-enantiomer of 4-Me(C$_6$H$_9$)CHF to the electronic excited state S_1 by a sequence of two linearly polarized enantio-selective laser pulses. Top: Envelope of the IR and UV laser fields; Bottom: Population dynamics of the affected localized states $\left|\Psi_{vwL/R}\right\rangle$ ($\widehat{=}$ vwL/R) and of the overall population in S_1.

Figure 5.31: Densities of the L- and the R-enantiomer at initial time $t = 0$ ps, after the first L-selective IR pump pulse $t = 7$ ps, and at final time after the second L-selective UV pump pulse $t = 14$ ps for the torsion-pyramidalization model of 4-Me(C_6H_9)CHF. During the first IR excitation no population is transferred from the electronic ground state S_0 to the electronic excited state S_1.

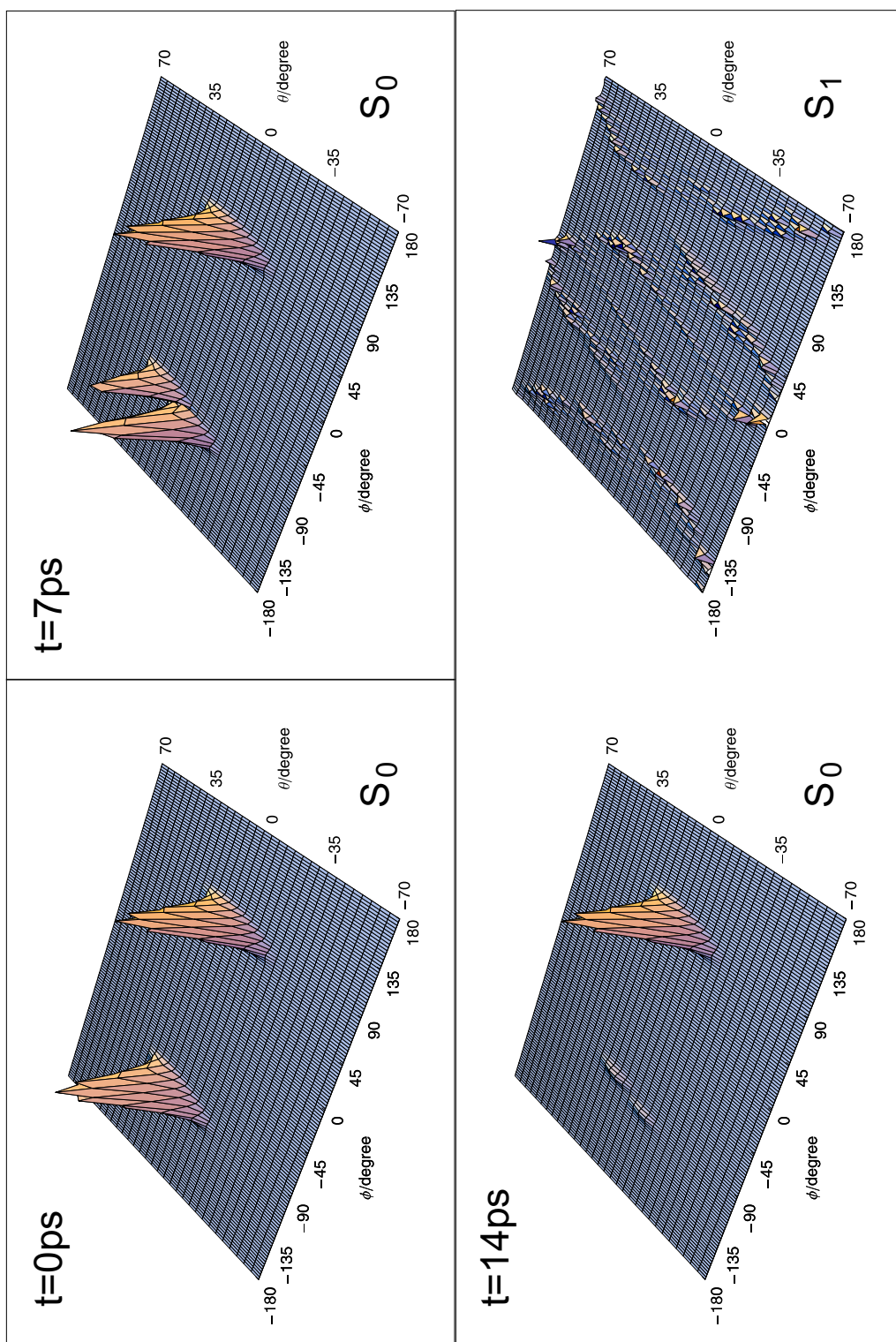Figure 5.31 shows snapshots of the density of both enantiomers at initial time $t = 0$ ps, after the first IR excitation ($t = 7$ ps) and at the final time $t = 14$ ps. After the second laser pulse at $t = 14$ ps the R-enantiomer is still in its initial state $|\Psi_{00R}\rangle$, while the L-enantiomer is almost completely[15] transfered to S_1 where a superposition of energetically high lying torsion-pyramidalization states are populated, as shown in fig. 5.31 (bottom right). Since the wave packet prepared in S_1 is delocalized over a large area of the potential, it is rather challenging to dump this population selectively to the ground state in order to purify the initial racemate, cf. scenario (a) of section 5.3.3. However, relaxation, e.g. via conical intersections, offers a possiblity for the purification of the racemate by laser distillation, see scenario (b).

property/parameter	IR pump pulse	UV pump pulse
dominant transition	$|\Psi_{00L}^0\rangle \rightarrow |\Psi_{01L}^0\rangle$	$|\Psi_{01L}^0\rangle \rightarrow S_1$
(transition) dipole	$\left\langle \Phi_{00g/u}^0 \middle| \mu_y^{00} \middle| \Phi_{01g/u}^0 \right\rangle$	$\langle \Phi_{01g}^0 | \mu_z^{01} | \Psi^1(10.5\text{ps}) \rangle^{(a)}$
matrix element/ea_0	$19.641 \cdot 10^{-3}$	$-88.213 \cdot 10^{-3}$
coupled to laser field	E_y^0	E_z^0
field amplitude E_j^0/GVm^{-1}	0.301	0.0955
(transition) dipole	$\left\langle \Phi_{00g/u}^0 \middle| \mu_x^{00} \middle| \Phi_{01u/g}^0 \right\rangle$	$\langle \Phi_{01u}^0 | \mu_x^{01} | \Psi^1(10.5\text{ps}) \rangle^{(a)}$
matrix element/ea_0	$1.5167 \cdot 10^{-3}$	$-2.4375 \cdot 10^{-3}$
coupled to laser field	E_x^0	E_x^0
field amplitude E_i^0/GVm^{-1}	3.9	3.2
frequency $\omega_i/2\pi c \cdot cm^{-1}$	747.7	46274.0
duration t_p/ps	7.0	7.0
phase $\eta_i/°$	0.0	0.0
pulse delay t_d/ps	0.0	7.0
total field amplitude $\overline{E}^0/GVm^{-1}$	3.91	3.20
intensity $I_k/TWcm^{-2}$	4.058	2.718
polarization angle $\alpha/°$	85.6	88.3

Table 5.7: Laser pulse parameters for the laser pulse sequence depicted in figure 5.30. (a) The transition dipole matrix elements are given for the optimized laser pulse parameters, i.e. for a transition between $\left| \Phi_{01u/g}^0 \right\rangle$ and the wave function in S_1 at the maximum of the UV laser pulse $|\Psi^1(\text{t=7ps+3.5ps})\rangle$.

The laser parameters of the pulse sequence are summarized in table 5.7. The duration of the UV pulse (7 ps) is much longer than the one of the UV laser used in the last 1D

---

[15]Less than 2% of the population is left in the left popential well of V_0.

calculation, see tab. 5.4 (section 5.3.3). Note that the long pulse durations for the IR and UV pulse allow much lower laser intensities than obtained for the 1D simulations. A long pulse duration for the UV pulse is possible because the population of a single eigenstate is transferred and not of a wave packet covering many eigenstates. Here the pyramidalizational degree of freedom offers an alternative route for asymmetric excitation without destroying the enantio-selectivity of the laser control. This modified enantio-selective IR-UV excitation is also very effective: more than 96% of the population of the L-enantiomer is pumped to S_1, see fig. 5.30.

It is also interesting to note that the IR light is propagating in z-direction while the UV light propagates perpendicular to it, i.e. in y-direction. This will become more important in the next section, where the effect of the orientation of the model system on the laser control is discussed.

5.5   Molecular orientation

An important assumption for both model systems presented in this work is the need of a defined molecular orientation with respect to the laser field. Although there are several ways to orient molecules, e.g. by intense laser fields [159, 160, 161, 162], experiments are usually based on a randomly oriented ensemble of molecules. Therefore, the effect of the molecular oriention on the selectivity of the enantio-selective laser control shall be investigated in the following.

In an oriented one-dimensional model system the conversion from one enantiomer to the other is described by the torsional angle ϕ, with $\phi = -90°$ corresponding to the L-form and $\phi = 90°$ to the R-form. Since the two enantiomers are mirror images of each other, they can be oriented in the laboratory frame (X, Y, Z) such that their respective permanent dipole moments $\vec{\mu}^L$ and $\vec{\mu}^R$ are given in molecule fixed coordinates (x, y, z) by

$$\vec{\mu}(\phi = -90°) \equiv \vec{\mu}^L = \begin{pmatrix} \mu_X^L \\ \mu_Y \\ \mu_Z \end{pmatrix} = \begin{pmatrix} \mu_x^L \\ \mu_y \\ \mu_z \end{pmatrix} \quad \text{and} \tag{5.67}$$

$$\vec{\mu}(\phi = 90°) \equiv \vec{\mu}^R = \begin{pmatrix} \mu_X^R \\ \mu_Y \\ \mu_Z \end{pmatrix} = \begin{pmatrix} \mu_x^R \\ \mu_y \\ \mu_z \end{pmatrix}, \quad \text{with} \tag{5.68}$$

$$\mu_x^L = -\mu_x^R, \tag{5.69}$$

provided $\vec{\mu}^L$ is transformed to $\vec{\mu}^R$ by a reflection at the YZ-plane, cf. fig. 5.4. This corresponds to the $+$ and $-$ symmetry of the components of the dipole moment along ϕ:

$\mu_x(\phi)$ has $-$ symmetry with respect to the achiral conformation of the model system at $\phi = 0°$, while $\mu_y(\phi)$ and $\mu_z(\phi)$ have $+$ symmetry.

Assuming a 1:1 mixture of both chiral forms, the electric field vector $\vec{E}_Z = \begin{pmatrix} E_X \\ E_Y \end{pmatrix}$ of a laser pulse propagating in Z-direction may be chosen linearly polarized such that its interaction with $\vec{\mu}^{01L}$ is non zero while its interaction with $\vec{\mu}^{01R}$ vanishes, cf. eqns. (5.5) and (5.6):

$$\vec{E}_Z \cdot \vec{\mu}^{01L} \neq 0 \tag{5.70}$$

$$\vec{E}_Z \cdot \vec{\mu}^{01R} = 0, \tag{5.71}$$

in order to excite selectively only the L-enantiomer from $|\Psi_{0L}\rangle$ to $|\Psi_{1L}\rangle$. Here $\vec{\mu}^{01L}$ and $\vec{\mu}^{01R}$ are the *transition dipole vectors* for the desired transition $|\Psi_{0L/R}\rangle \rightarrow |\Psi_{1L/R}\rangle$ and are defined in general in molecular coordinates as:

$$\vec{\mu}^{vv'L} = \begin{pmatrix} \langle \Psi_{vL} | \mu_x(\phi) | \Psi_{v'L}\rangle \\ \langle \Psi_{vL} | \mu_y(\phi) | \Psi_{v'L}\rangle \\ \langle \Psi_{vL} | \mu_z(\phi) | \Psi_{v'L}\rangle \end{pmatrix} = \begin{pmatrix} \mu_x^{vv'L} \\ \mu_y^{vv'L} \\ \mu_z^{vv'L} \end{pmatrix} \tag{5.72}$$

$$\vec{\mu}^{vv'R} = \begin{pmatrix} \langle \Psi_{vR} | \mu_x(\phi) | \Psi_{v'R}\rangle \\ \langle \Psi_{vR} | \mu_y(\phi) | \Psi_{v'R}\rangle \\ \langle \Psi_{vR} | \mu_z(\phi) | \Psi_{v'R}\rangle \end{pmatrix} = \begin{pmatrix} \mu_x^{vv'R} \\ \mu_y^{vv'R} \\ \mu_z^{vv'R} \end{pmatrix}, \tag{5.73}$$

for a transition $|\Psi_{vL}\rangle \rightarrow |\Psi_{v'L}\rangle$ or $|\Psi_{vR}\rangle \rightarrow |\Psi_{v'R}\rangle$ ($v \neq v'$), respectively. Using the definition of $|\Psi_{vL}\rangle$ and $|\Psi_{vR}\rangle$ (cf. eqn. 3.1) and the selection rules (cf. eqn. 4.19), $\mu_x^{vv'L}$ and $\mu_x^{vv'R}$ are expressed as

$$\mu_x^{vv'L} = \frac{1}{2}\left(\langle \Phi_{v+} | \mu_x | \Phi_{v'-}\rangle + \langle \Phi_{v-} | \mu_x | \Phi_{v'+}\rangle \right) \approx \langle \Phi_{v+} | \mu_x | \Phi_{v'-}\rangle \tag{5.74}$$

$$\mu_x^{vv'R} = -\frac{1}{2}\left(\langle \Phi_{v+} | \mu_x | \Phi_{v'-}\rangle + \langle \Phi_{v-} | \mu_x | \Phi_{v'+}\rangle \right) \approx - \langle \Phi_{v+} | \mu_x | \Phi_{v'-}\rangle \tag{5.75}$$

since $\langle \Phi_{v+} | \mu_x | \Phi_{v'-}\rangle \approx \langle \Phi_{v-} | \mu_x | \Phi_{v'+}\rangle$ for doublets v, v' where $+$ and $-$ states are energetically degenerate. From equations (5.74) and (5.75) one sees that $\mu_x^{vv'L} = -\mu_x^{vv'R}$. On the other hand, the y-component as well as the z-component of the transition dipole vector are equal for the L- and R-enantiomer, i.e. $\mu_y^{vv'L} = \mu_y^{vv'R}$ and $\mu_z^{vv'L} = \mu_z^{vv'R}$, since $\mu_y(\phi)$ and $\mu_z(\phi)$ have $+$ symmetry.

Condition (5.71) means that the electric field vector $\vec{E}_Z$ must be perpendicular to the transition dipole vector $\vec{\mu}^{01R}$ to suppress an excitation of the R-enantiomer. In figure 5.32 (left) the projection of $\vec{\mu}^{01L}$ and $\vec{\mu}^{01R}$ onto the XY-plane is sketched for the special case $|\mu_x^{01L/R}| = |\mu_y^{01L/R}|$, i.e. $\vec{\mu}^{01L}$ and $\vec{\mu}^{01R}$ are perpendicular to each other in the XY-plane. The L-selective linearly polarized electric field vector $\vec{E}_Z$ is parallel to $\vec{\mu}^{01L}$ since

it must be perpendicular to $\vec{\mu}^{01R}$ to suppress any interaction with the R-enantiomer. But after the molecule has been rotated by $90°$ counter-clockwise around the Z-axis the exact opposite result is obtained, see fig. 5.32 (right). Now the laser field $\vec{E}_Z$ is perpendicular to $\vec{\mu}^{01L}$ and, hence, it interacts with the R-form by transferring population from $|\Psi_{0R}\rangle$ to $|\Psi_{1R}\rangle$ without effecting the L-form. The same result can be achieved by a rotation of the molecule around the Y-axis by $180°$ or by a rotation around the X-axis by $180°$, see fig. 5.33.
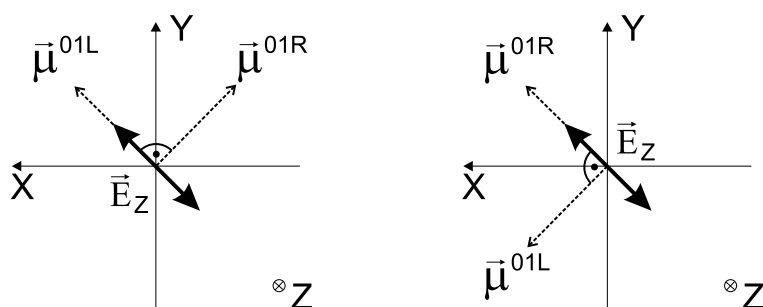

Figure 5.32: Left: Projection of the transition dipole vectors $\vec{\mu}^{01L}$ and $\vec{\mu}^{01R}$, as defined in eqns. (5.72) and (5.73), onto the XY-plane of the laboratory fixed coordinate system for the special case $|\mu_x^{01L/R}| = |\mu_y^{01L/R}|$. The electric field vector $\vec{E}_Z$ of the laser pulse is polarized such that it induces a transition from $|\Psi_{0L}\rangle$ to $|\Psi_{1L}\rangle$ without effecting the R-enantiomer. Right: The molecules has been rotated by $90°$ counter-clockwise around the Z-axis; now the enantio-selective laser pulse excites the R-enantiomer from $|\Psi_{0R}\rangle$ to $|\Psi_{1R}\rangle$ while $|\Psi_{0L}\rangle$ is not affected.
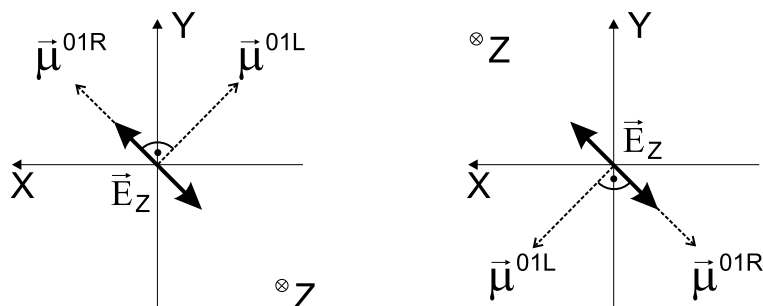
Figure 5.33: Projection of the transition dipole vectors $\vec{\mu}^{01L}$ and $\vec{\mu}^{01R}$ onto the XY-plane, as used in fig. 5.32 (left). Left: After rotation of the molecule by $180°$ around the Y-axis the originally L-selective laser field $\vec{E}_Z$ excites the R-enantiomer from $|\Psi_{0R}\rangle$ to $|\Psi_{1R}\rangle$. Right: The same effect is obtained after rotation of the molecule around the X-axis by $180°$.

Considering an ensemble of randomly oriented molecules, it becomes clear that no matter how the enantio-selective laser pulse is polarized, on the average, it will interact with the same amount of R- and L-enantiomers leaving their 1:1 ratio in a racemic mixture untouched. However, if the molecules are oriented e.g. in the positive Z-direction, as shown in fig. 5.4, but allowing all possible orientations with respect to the X- and Y-axis, i.e. the molecules are aligned along the Z-axis pointing in the same direction[16], then enantio-selectivity can be maintained by introducing an additional subsequent enantio-selective laser pulse. Before the effect of the second laser pulse is discussed, it is convenient to make several assumptions:

a) The control sequence consists of two subsequent enantio-selective laser pulses which propagate perpendicular to each other. In analogy to the results in section 5.4.3, the first laser pulse is an IR pulse propagating in Z-direction, and the second is an UV pulse propagating in Y-direction.

b) All molecules are aligned along the Z-axis of the laboratory frame pointing in the same direction, specifically in the positive Z-direction, as shown in fig. 5.4. In the following the molecules are referred to *oriented along* the Z-axis.

c) Let the angle χ represent all possible orientations of the enantiomers in the racemic mixture *around* the Z-axis. Specifically, χ is *defined* zero for the case where the first enantio-selective pulse $\vec{E}_Z$ interacts with the enantiomers such that the product $\vec{E}_Z \cdot \vec{\mu}^{01R}$ becomes zero, i.e. for a 100% effective L-selective $|\Psi_{0L}\rangle \rightarrow |\Psi_{1L}\rangle$ excitation. Then, the electric field vector $\vec{E}_Z$ becomes perpendicular to $\vec{\mu}^{01L}$ at two specific angles, χ and $\chi \pm 180°$. In the example shown in fig. 5.32 this is the case at $\chi = 90°$ and $\chi = 270°$. In general, the orientation angle χ for which the product $\vec{E}_Z \cdot \vec{\mu}^{01L}$ equals zero depends on the relation of $|\mu_x^{01L/R}|$ to $|\mu_y^{01L/R}|$. For simplicity $|\mu_x^{01L/R}| = |\mu_y^{01L/R}|$ is assumed.

d) The subsequent UV laser pulse $\vec{E}_Y$ is designed to selectively excite the L-enantiomer from $|\Psi_{1L}\rangle$ to an eigenstate $\left|\Phi_{w\pm}^1\right\rangle \widehat{=} |e\rangle$ of the electronic excited state S_1. The pulse is optimized such that its electric field vector is perpendicular to the respective transition dipole vector $\vec{\mu}^{1Re}$ at $\chi = 0°$ fulfilling the condition:

$$\vec{E}_Y \cdot \vec{\mu}^{1Le} \neq 0 \tag{5.76}$$
$$\vec{E}_Y \cdot \vec{\mu}^{1Re} = 0, \tag{5.77}$$

---

[16]Alignment is the defined order of the molecular geometry with respect to a space-fixed axis, while orientation also includes a defined direction with respect to the space-fixed axis. Therefore, the molecules here are *oriented* with respect to the Z-axis, but not with respect to the X- and Y-axis. In order to distinguish between molecules oriented with respect to all three axis and those oriented with respect to only one specific axis, the later case will be called orientation *along* the specific axis or *unidirectional* orientation, which is equivalent to an unidirectional alignment.

i.e. inducing a 100% population transfer from $|\Psi_{1L}\rangle$ to $|e\rangle$. Here $\vec{\mu}^{1Le}$ and $\vec{\mu}^{1Re}$ are defined in the molecule fixed coordinate system analogously to eqn. (5.72):

$$\vec{\mu}^{vLe} = \begin{pmatrix} \langle\Psi_{vL}|\,\mu_x^{01}(\phi)\,|\Phi_{w\pm}^1\rangle \\ \langle\Psi_{vL}|\,\mu_y^{01}(\phi)\,|\Phi_{w\pm}^1\rangle \\ \langle\Psi_{vL}|\,\mu_z^{01}(\phi)\,|\Phi_{w\pm}^1\rangle \end{pmatrix} = \begin{pmatrix} \mu_x^{vLe} \\ \mu_y^{vLe} \\ \mu_z^{vLe} \end{pmatrix} \tag{5.78}$$

$$\vec{\mu}^{vRe} = \begin{pmatrix} \langle\Psi_{vR}|\,\mu_x^{01}(\phi)\,|\Phi_{w\pm}^1\rangle \\ \langle\Psi_{vR}|\,\mu_y^{01}(\phi)\,|\Phi_{w\pm}^1\rangle \\ \langle\Psi_{vR}|\,\mu_z^{01}(\phi)\,|\Phi_{w\pm}^1\rangle \end{pmatrix} = \begin{pmatrix} \mu_x^{vRe} \\ \mu_y^{vRe} \\ \mu_z^{vRe} \end{pmatrix}, \tag{5.79}$$

for a transition from $|\Psi_{vL/R}\rangle$ to $|\Phi_{w\pm}^1\rangle$ assuming a different transition frequency as for the transition from $|\Psi_{0L}\rangle$ to $|\Psi_{1L}\rangle$. The x-component of the transition dipole vector is defined to have $-$ symmetry while the z- and y-component have $+$ symmetry. Hence, $\mu_x^{vLe} = -\mu_x^{vRe}$ while $\mu_y^{vLe} = \mu_y^{vRe}$ and $\mu_z^{vLe} = \mu_z^{vRe}$. In figure 5.34 (left) the projection of the transition dipole vectors $\vec{\mu}^{1Le}$ and $\vec{\mu}^{1Re}$ onto the XZ-plane of the laboratory fixed coordinate system for $\chi = 0°$, i.e. the pre-oriented molecule, as well as the electric field vector $\vec{E}_Y$ are shown; for simplicity the special case $|\mu_x^{1L/Re}| = |\mu_z^{1L/Re}|$ ($\neq |\mu_y^{1L/Re}|$) is considered.

In order to illustrate the effect of the second enantio-selective laser pulse, four special cases for the orientation of the molecules, namely $\chi = 0/360°$, $90°$, $180°$ and $270°$, are considered:

$\chi = 0/360°$:
   The molecules are pre-oriented. Then, the first L-selective laser pulse transfers the population of $|\Psi_{0L}\rangle$ to $|\Psi_{1L}\rangle$ (fig. 5.32 left), and the second pulse transfers $|\Psi_{1L}\rangle$ to $|e\rangle$ (fig. 5.34 left) leaving $|\Psi_{0R}\rangle$ completely populated.

$\chi = 180°$:
   The molecules have been rotated around the Z-axis by $\chi = 180°$. Then, the enantio-selectivity of the second laser pulse is switched from L to R because $\vec{E}_Y$ becomes parallel to $\vec{\mu}^{1Re}$ and perpendicular to $\vec{\mu}^{1Le}$, see figure 5.34 (right). These rotated molecules are still interacting with the first laser pulse as desired, i.e. population is selectively excited from $|\Psi_{0L}\rangle$ to $|\Psi_{1L}\rangle$[17]. Hence, the second laser pulse has for $\chi = 180°$ neither an effect on $|\Psi_{1L}\rangle$ nor on $|\Psi_{0R}\rangle$.

$\chi = 90°$:
   The molecules have been rotated counter-clockwise around the Z-axis by $90°$, as

---

[17]Not shown, but can easily be derived from fig. 5.32 (left).

shown in fig. 5.32 (right). Then, population is transferred from $|\Psi_{0R}\rangle$ to $|\Psi_{1R}\rangle$ by the first laser pulse. The second laser pulse propagating in Y-direction, however, will not interact with the x- and z-components of $\vec{\mu}^{1Le}$ and $\vec{\mu}^{1Re}$ any more, i.e. with their projections onto the YZ-plane of the laboratory frame, see figure 5.35 (left). The laser field $\vec{E}_Y$ interacts with the projections of the rotated transition dipole vectors onto the XZ-plane, i.e. with their y- and z-components. Since $\mu_y^{1Le} = \mu_y^{1Re}$ and $\mu_z^{1Le} = \mu_z^{1Re}$ the projection of $\vec{\mu}^{1Le}$ and $\vec{\mu}^{1Re}$ onto the XZ-plane of the laboratory frame are after the rotation the same vector $\vec{\mu}^{1L/Re}$, as shown in fig. 5.35 (middle), and thus, the laser field cannot differentiate between the L- and R-form. Therefore, since the first pulse transfers population only to $|\Psi_{1R}\rangle$, $\vec{E}_Y$ will transfer this population to $|e\rangle$. The amount of population excited to S_1 depends on how effective $\vec{E}_Y$ interacts with $\vec{\mu}^{1L/Re}$, i.e. it depends on the components of the transition dipole vector $\mu_y^{1L/Re}$ and $\mu_z^{1L/Re}$.

$\chi = 270°$:

The molecules have been rotated counter-clockwise by 270° around the z-axis. Then, the first laser pulse will selectively excite $|\Psi_{0R}\rangle$ to $|\Psi_{1R}\rangle$. The amount of population the second laser field $\vec{E}_Y$ transfers to $|e\rangle$ depends again only on its interaction with $\vec{\mu}^{1L/Re}$, i.e. with the components $\mu_y^{1L/Re}$ and $\mu_z^{1L/Re}$, see fig. 5.35 (right).
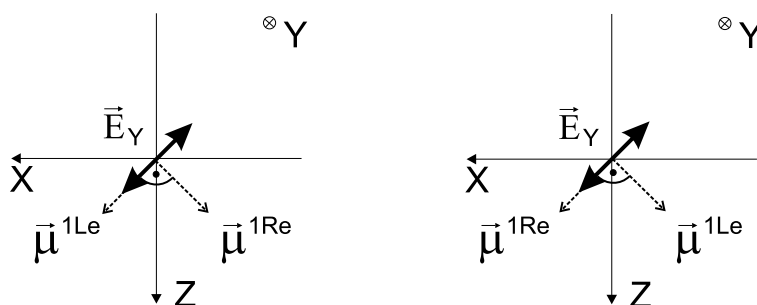

Figure 5.34: Left: Projection of the transition dipole vectors $\vec{\mu}^{1Le}$ and $\vec{\mu}^{1Re}$ onto the XZ-plane of the laboratory fixed coordinate system for a pre-oriented one-dimensional model system. The electric field vector $\vec{E}_Y$ of the laser pulse is polarized such that it induces a transition from $|\Psi_{1L}\rangle$ to S_1 ($\widehat{=} |e\rangle$) without affecting the R-enantiomer. Right: After the molecule is rotated around the Z-axis by 180°, the enantio-selective laser pulse excites the R-enantiomer from $|\Psi_{1R}\rangle$ to $|e\rangle$ without affecting $|\Psi_{1L}\rangle$.
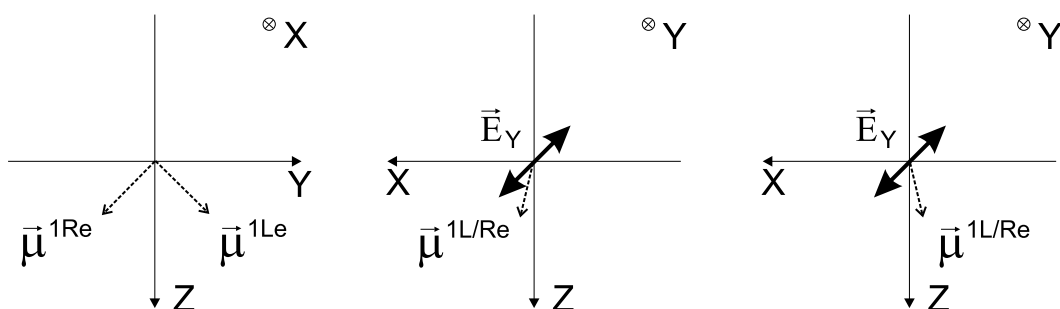
Figure 5.35: Left: Projection of the interaction dipole vectors $\vec{\mu}^{1Le}$ and $\vec{\mu}^{1Re}$ onto the XY-plane (composed of the components $\mu_x^{1L/Re}$ and $\mu_z^{1L/Re}$), as used in fig. 5.34 (left), after counter-clockwise rotation of the molecule by $90°$ around the Z-axis. Middle and right: Projection of the transition dipole vector $\vec{\mu}^{1L/Re}$ onto the XZ-plane ($\mu_y^{1Le} = \mu_y^{1Re}$ and $\mu_z^{1Le} = \mu_z^{1Re}$) which interact with the laser field $\vec{E}_Y$ after counter-clockwise rotation of the molecule by $90°$ (middle) or $270°$ (right) around the Z-axis.

orientation	1st pulse $\vec{E}_Z$ (IR)		2nd pulse $\vec{E}_Y$ (UV)	
angle χ	$\lvert\Psi_{0L}\rangle \rightarrow \lvert\Psi_{1L}\rangle$	$\lvert\Psi_{0R}\rangle \rightarrow \lvert\Psi_{1R}\rangle$	$\lvert\Psi_{1L}\rangle \rightarrow \lvert e\rangle$	$\lvert\Psi_{1R}\rangle \rightarrow \lvert e\rangle$
$0°$	100%	-	100%	-
$90°$	-	100%	a%[*)]	a%[*)]
$180°$	100%	-	-	100%
$270°$	-	100%	b%[*)]	b%[*)]

Table 5.8: Dominant transition induced by a sequence of two enantio-selective pump pulses with respect to the orientation of the molecules. The orientation angle χ is given for a counter-clockwise rotation of the molecules around the Z-axis. The table holds for a model system as discussed in the text. The amount of population transferred by the transitions marked by [*)] depends on the y- and z-component of the transition dipole vector $\vec{\mu}^{1L/Re}$, see fig. 5.35.

Table 5.8 summarizes the effect of the two sequent enantio-selective linearly polarized laser pulses for the four discussed molecular orientations. The net effect of the first laser pulse is that $\lvert\Psi_{0L}\rangle$ and $\lvert\Psi_{0R}\rangle$ are excited to the same extent and, hence no selectivity is achieved (see tab. 5.8). After the second laser pulse an overall enantio-selectivity is obtained if the total amount of population transferred from $\lvert\Psi_{1R}\rangle$ to $\lvert e\rangle$ of the molecules oriented at $\chi = 90°$ and $270°$ together is different than the population transferred from $\lvert\Psi_{1L}\rangle$ to $\lvert e\rangle$ at $\chi = 0°$, i.e. if $a + b \neq 100$ (see table 5.8). Since the amount of population

transferred by the UV pulse at $\chi = 90°/270°$ depends only on the components $\mu_y^{1L/Re}$ and $\mu_z^{1L/Re}$ of the transition dipole vector $\vec{\mu}^{1L/Re}$ (see fig. 5.35 middle and right) the amount of the enantiomeric excess obtained in S_1 in a real molecular model system is difficult to predict.

Averaged over all orientation angles, also the second laser pulse would excite $|\Psi_{1L}\rangle$ and $|\Psi_{1R}\rangle$ to $|e\rangle$ by the same extent if $|\Psi_{1L}\rangle$ and $|\Psi_{1R}\rangle$ were completely populated after the first pulse, see tab. 5.8. But the maxima of the interaction $\vec{E}_Z \cdot \vec{\mu}^{01L/R}$ along χ do not coincide with the ones of the second pulse, see e.g. $\chi = 180°$. Therefore, a laser pulse sequence consisting of two enantio-selective laser pulses should produce enantiomeric excess in S_1 in an ensemble of molecules oriented along the Z-axis. Yet, how much population is enantio-selectively transferred to S_1 at the orientation angles not given in table 5.8 can only be calculated using a molecular model system.

But before numerical simulations are discussed, it is interesting to consider also the case in which the molecules are oriented along the Y-axis instead along the Z-axis. The dominant transitions induced by the sequence of the two enantio-selective pump pulses are listed in table 5.9 for four orientation angles. Note that the two pairs of columns with the dominant transitions are exchanged accordingly, in comparison to table 5.8. Now the efficiency of the *first* IR pulse depends on the amount of population transferred at $\chi = 90°$ and $270°$ (marked by [*)] in tab. 5.9). Nevertheless, also for an ensemble of molecules oriented along the Y-axis enantiomeric excess in S_1 should be achieved by the sequence of the two enantio-selective laser pulses, as long as $c + d \neq 100$ (cf. tab. 5.9).

orientation angle χ	1st pulse $\vec{E}_Z$ (IR)		2nd pulse $\vec{E}_Y$ (UV)	
	$|\Psi_{0L}\rangle \rightarrow |\Psi_{1L}\rangle$	$|\Psi_{0R}\rangle \rightarrow |\Psi_{1R}\rangle$	$|\Psi_{1L}\rangle \rightarrow |e\rangle$	$|\Psi_{1R}\rangle \rightarrow |e\rangle$
0°	100%	-	100%	-
90°	c%[*)]	c%[*)]	-	100%
180°	-	100%	100%	-
270°	d%[*)]	d%[*)]	-	100%

Table 5.9: Dominant transition induced by a sequence of two enantio-selective pump pulses with respect to the orientation of the molecule. The rotation angle χ is given for a counter-clockwise rotation of the molecule around the Y-axis. The table holds for a model system as discussed in the text. The effectiveness of the transitions marked by [*)] depends on the y- and z-component of the transition dipole vector $\vec{\mu}^{01L/R}$.

The dominant transitions induced by the sequence of the two enantio-selective pump pulses in a racemic mixture of enantiomers oriented along the X-axis are summarized in

table 5.10. A rotation around the X-axis is not favorable for the suggested laser pulse sequence because at $\chi = 180°$ the first and the second laser pulse will excite selectively population from $|\Psi_{0R}\rangle$ via $|\Psi_{1R}\rangle$ to $|e\rangle$ compensating for the excess of L-population in S_1 obtained at $\chi = 0°$. Besides, at $\chi = 90°$ and $270°$ the laser pulses can, unlike in the cases of molecular orientation along the Y- or Z-axis, still differentiate between the L- and R-form of the molecules. At these orientation angles the projections of the transition dipole vectors $\vec{\mu}^{01L}$ and $\vec{\mu}^{01R}$ onto the XY-plane do not coincide to one single vector. Also the projections of $\vec{\mu}^{1Le}$ and $\vec{\mu}^{1Re}$ onto the YZ-plane are different vectors at $\chi = 90/270°$. For both laser pulses the reason is that the projection vectors depend on the anti-symmetric x-components of the respective transition dipole vectors at $\chi = 90/270°$. Therefore, the transitions marked by [*] and [**] in table 5.10 cannot cause any enantiomeric excess.

orientation angle χ	1st pulse $\vec{E}_Z$ (IR)		2nd pulse $\vec{E}_Y$ (UV)	
	$|\Psi_{0L}\rangle \rightarrow |\Psi_{1L}\rangle$	$|\Psi_{0R}\rangle \rightarrow |\Psi_{1R}\rangle$	$|\Psi_{1L}\rangle \rightarrow |e\rangle$	$|\Psi_{1R}\rangle \rightarrow |e\rangle$
0°	100%	-	100%	-
90°	e%[*]	f%[*]	g%[**]	h%[**]
180°	-	100%	-	100%
270°	f%[*]	e%[*]	h%[**]	g%[**]

Table 5.10: Dominant transition induced by a sequence of two enantio-selective pump pulses with respect to the orientation of the molecule. The rotation angle χ is given for a counter-clockwise rotation of the molecule around the X-axis. The table holds for a model system as discussed in the text. The effectiveness of the transitions marked by [*] depends on the x- and z-component of the transition dipole vectors $\vec{\mu}^{01L}$ and $\vec{\mu}^{01R}$. The effectiveness of the transitions marked by [**] depends on the x- and y-component of the transition dipole vectors $\vec{\mu}^{1Le}$ and $\vec{\mu}^{1Re}$.

In order to test the predictions made for molecules oriented along the Z-axis the two-dimensional model system 4-Me(C_6H_9)CHF, as described in section 5.4.3, is used. The first enantio-selective pump pulse of the control sequence excites the system from $|\Psi_{00L}\rangle$ to $|\Psi_{01L}\rangle$ at $\chi = 0°$. Note that for a pre-oriented molecule ($\chi = 0°$) this transition was optimized to $\sim$100% population transfer. To describe the different orientations of the model the laser field is rotated (together with the laboratory coordinate system) clockwise around the z-axis of the molecular frame, which is equivalent to a counter-clockwise rotation of the molecule with respect to the Z-axis of the laboratory frame. The rotation angle χ describes the orientation of the laser field with respect to the molecule. For $\chi = 0°$ the molecule is fixed in the laboratory coordinate system as shown in fig. 5.26. For an

arbitrary angle χ the electric field vector $\vec{E}^0(\chi)$ is given in molecular coordinates as:

$$\vec{E}^0(\chi) = \begin{pmatrix} \cos\chi & -\sin\chi & 0 \\ \sin\chi & \cos\chi & 0 \\ 0 & 0 & 1 \end{pmatrix} \begin{pmatrix} E_x^0 \\ E_y^0 \\ E_z^0 \end{pmatrix} = \begin{pmatrix} E_x^0\cos\chi - E_y^0\sin\chi \\ E_x^0\sin\chi + E_y^0\cos\chi \\ E_z^0 \end{pmatrix}. \qquad (5.80)$$

In the case of the IR pulse propagating in Z-direction $\vec{E}_Z^0$ one obtains (in at. un., i.e. in E_h/ea_0) using the parameters from table 5.7:[18]

$$\vec{E}_Z^0(\chi) = \begin{pmatrix} 7.58\cos\chi - 0.585\sin\chi \\ 7.58\sin\chi + 0.585\cos\chi \\ 0.0 \end{pmatrix} \cdot 10^{-3}. \qquad (5.81)$$

To scan all possible orientations $\vec{E}_Z^0$ is rotated along χ in steps of $\chi = 2.5°$. For each χ a quantum wave packet propagation is carried out (SOD, 4096 grid points, 0.01 fs/step, qmpropa [133]) starting each time from a racemic mixture of $|\Psi_{00L}\rangle$ and $|\Psi_{00R}\rangle$. In figure 5.36 (top) the population of the initial states $|\Psi_{00L}\rangle$ (plain line) and $|\Psi_{00R}\rangle$ (dashed line) after the first IR laser pulse is plotted versus the orientation angle χ.

At $\chi = 0°$ the L-selective laser pulse $\vec{E}_Z^0(0°)$ depopulates $|\Psi_{00L}\rangle$ completely leaving $|\Psi_{00R}\rangle$ untouched. As expected at $\chi = 180°$ the same result is obtained because $\vec{E}_Z^0(180°)$ and $\vec{\mu}^{01R}$ are perpendicular. In order to determine the angle χ at which $\vec{E}_Z^0(\chi)$ becomes perpendicular to $\vec{\mu}^{01L}$ the parameters from table 5.7 are used; the transition dipole vector $\vec{\mu}^{01L}$ is defined, in accordance with eqn. (5.72)[19] (in at. un., i.e. in ea_0):

$$\begin{aligned} \vec{\mu}^{01L} &= \begin{pmatrix} \langle\Psi_{00L}|\,\mu_x^{00}\,|\Psi_{01L}\rangle \\ \langle\Psi_{00L}|\,\mu_y^{00}\,|\Psi_{01L}\rangle \\ \langle\Psi_{00L}|\,\mu_z^{00}\,|\Psi_{01L}\rangle \end{pmatrix} = \begin{pmatrix} \langle\Phi_{00g}|\,\mu_x^{00}\,|\Phi_{01u}\rangle \\ \langle\Phi_{00g}|\,\mu_y^{00}\,|\Phi_{01g}\rangle \\ \langle\Phi_{00g}|\,\mu_z^{00}\,|\Phi_{01g}\rangle \end{pmatrix} \\ &= \begin{pmatrix} \langle\Phi_{00u}|\,\mu_x^{00}\,|\Phi_{01g}\rangle \\ \langle\Phi_{00u}|\,\mu_y^{00}\,|\Phi_{01u}\rangle \\ \langle\Phi_{00u}|\,\mu_z^{00}\,|\Phi_{01u}\rangle \end{pmatrix} = \begin{pmatrix} 1.52 \\ 19.6 \\ 1.41 \end{pmatrix} \cdot 10^{-3}. \qquad (5.82) \end{aligned}$$

The respective interaction vector $\vec{\mu}^{01R}$ has a negative x-component ($\mu_x^{01R} = -1.52 \cdot 10^{-3}\ ea_0$). For $\vec{E}_Z^0(171.2°) = \begin{pmatrix} -7.58 \\ 0.585 \end{pmatrix} \cdot 10^{-3}\ E_h/ea_0$ and for $\vec{E}_Z^0(351.2°) = \begin{pmatrix} 7.58 \\ -0.585 \end{pmatrix} \cdot 10^{-3}\ E_h/ea_0$, the scalar product $\vec{E}_z^0(\chi) \cdot \vec{\mu}^{01L}$ equals zero. Accordingly, at $\chi = 171°$ and $351°$ in figure 5.36 (top) $|\Psi_{00R}\rangle$ is almost completely depopulated while $|\Psi_{00L}\rangle$ keeps approximately its initial population of 0.5. This means, if the curve for $|\Psi_{00L}\rangle$ is shifted by

---

[18] $1\ E_h/ea_0 = 514.22$ GV/m

[19] Note that for simplicity here the superindices vv' of the transition dipol vector $\vec{\mu}^{vv'L}$ indicate a change only in one quantum number, i.e. $\vec{\mu}^{01L} \equiv \vec{\mu}^{0001L}$.
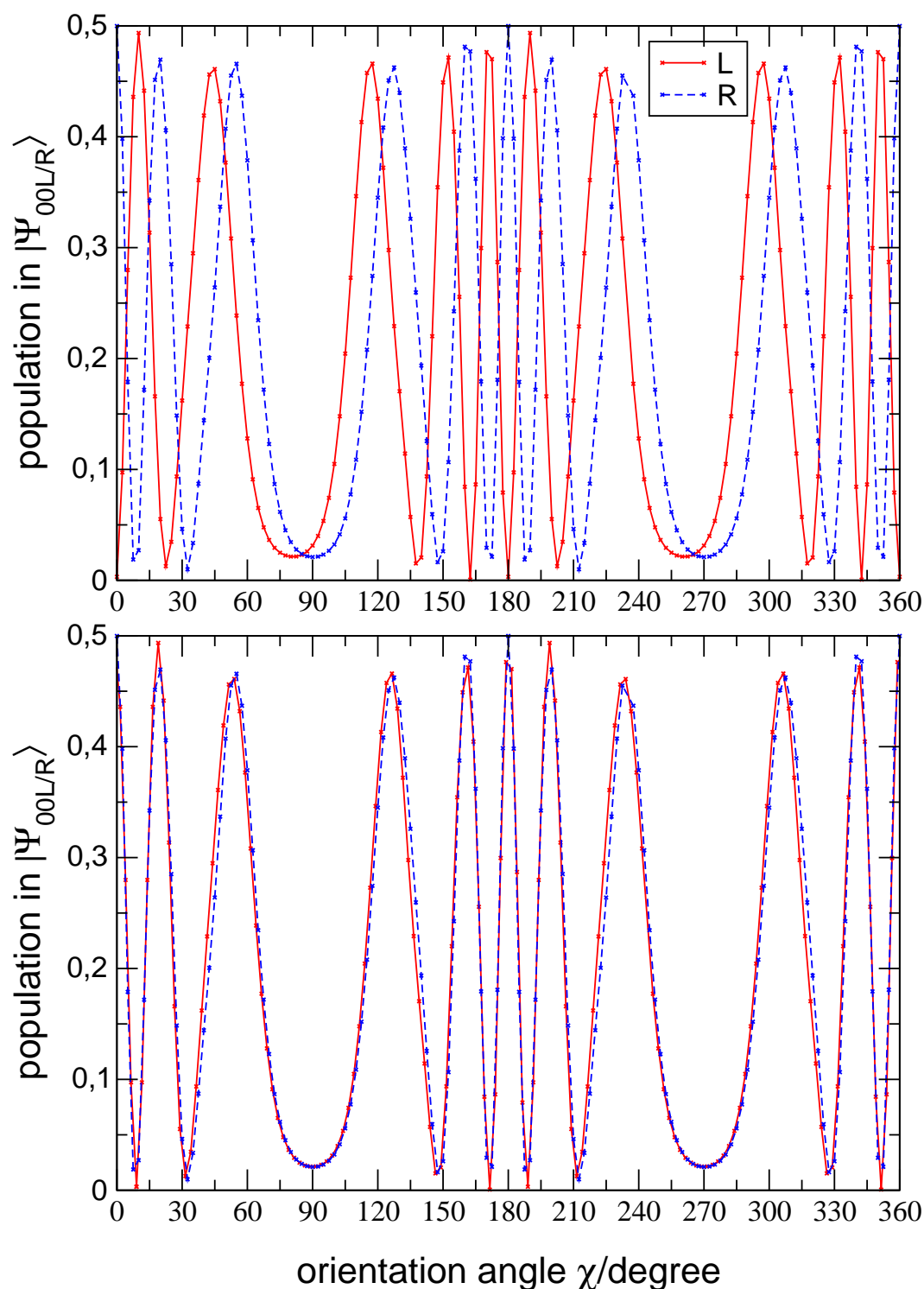
Figure 5.36: Top panel: Population of the initial state $|\Psi_{00L}\rangle$ (plain line) and $|\Psi_{00R}\rangle$ (dashed line) versus the orientation angle χ (in steps of 2.5°) after the first enantio-selective IR pump pulse depicted in fig. 5.30. Bottom panel: The curve for the population of $|\Psi_{00L}\rangle$ is shifted by 9° to coincide with the curve for the population of $|\Psi_{00R}\rangle$ (see text).

$\sim +9°$ then it should coincides with the curve for $|\Psi_{00R}\rangle$. Figure 5.36 (bottom) shows the two almost coinciding curves. Although these curves give no information about how much $|\Psi_{01L}\rangle$ or $|\Psi_{01R}\rangle$ or other states are populated, they show, as predicted, that an L-selective laser pulse optimized for a certain molecular orientation will be not enantio-selective for an ensemble of molecules oriented along the Z-axis (cf. tab. 5.8): The integrals under the $|\Psi_{00L}\rangle$- and $|\Psi_{00R}\rangle$-curves, using the values of the calculated points, give a ratio of 1:0.99. It is also important to note that both curves in fig. 5.36 (bottom) are almost perfectly symmetric with respect to $\chi = 0/180°$, as expected from the theoretical example discussed before.

For the pre-oriented molecule ($\chi = 0°$) the IR laser pulse was choosen to be a π-pulse, i.e. to cause a 100% population transfer from $|\Psi_{00L}\rangle$ to $|\Psi_{01L}\rangle$, see the derivation in section 5.3.3. With the values from eqns. (5.81) and (5.82) the pulse area A, as defined in eqn. (2.98), can be calculated as a function of χ. For $A = (2n + 1)\pi$ ($n = 0, 1, 2...$) a full population transfer should be induced by the laser pulse. If the pulse area A is an even multiple of π then no population transfer should occur, see section 2.4.1. Figure 5.37 shows the calculated pulse area $A(\chi) = \vec{E}_Z^0(\chi) \cdot \vec{\mu}^{01L/R} \cdot t_p/2$ in units of π of the IR laser pulse as a function of the orientation angle χ. The solid curve calculated from $\vec{\mu}^{01L}$ is shifted by $\sim -9°$ with respect to the dashed curve calculated from $\vec{\mu}^{01R}$. The horizontal lines at $A/\pi \approx 1$ and $A/\pi \approx 2$ mark the value for which approximately a 1π- or 2π-transition, respectively, is induced by the laser field. Table 5.11 lists the calculated values of A for the orientation angles χ marked in fig. 5.37 by arrows. The solid lined arrows mark the orientation angle χ at which the pulse area A for the interaction with the L-enantiomers reaches π or 2π; the dashed lined arrows mark the respective π or 2π-pulse interaction with the R-enantiomers.

At $\chi = 0/360°$ and $180°$ the dashed line for the interaction with the R-enantiomer reaches zero while the solid line for the L-enantiomer has the value of approximately π, marked by solid lined arrows in fig. 5.37. The opposite result is found for $\chi = 171°$ and $351°$, marked by dashed lined arrows. At $\chi \approx 162°$ and $\chi \approx 342°$ a π-pulse transition is induced in the L-enantiomer and a 2π-pulse transition, i.e. no population transfer, in the R-enantiomer. Note that at these angles $|\Psi_{00L}\rangle$ is almost depopulated while the population of $|\Psi_{00R}\rangle$ stays almost unchanged, see fig. 5.36. The opposite result is found at $\chi = 9°$ and $189°$, see figures 5.37 and 5.36. This investigation can be continued towards the maxima of the curves in fig. 5.37 resulting in higher even or odd π-pulse areas for L- and R-enantiomers. The oscillation of the $|\Psi_{00L}\rangle$- and $|\Psi_{00R}\rangle$-curves in fig. 5.36 around $\chi = 0/360°$ and $\chi = 180°$ can be explained by the resulting alternating even and odd π-pulse transitions, cf. tab. 5.11.
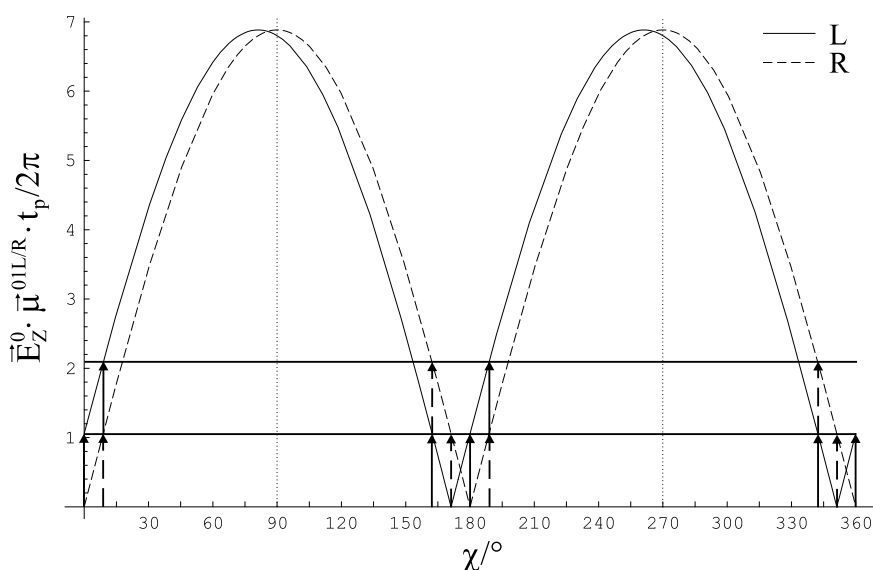
Figure 5.37: The area $A(\chi) = \vec{E}_Z^0(\chi) \cdot \vec{\mu}^{01L/R} \cdot t_p/2$ of the first IR laser pulse in units of π calculated for the values given in eqn. (5.81) and (5.82). The two horizontal lines mark the value for which $\sim 100\%$ and $\sim 0\%$, corresponding to a π and 2π-pulse, population transfer from $\left|\Psi_{00L/R}\right\rangle$ to $\left|\Psi_{01L/R}\right\rangle$ is accomplished. The solid and dashed lined arrows mark the angles χ for the L- and R-selective transitions listed in tab. 5.11, respectively.

orientation angle χ	$\left|\Psi_{00L}\right\rangle \rightarrow \left|\Psi_{01L}\right\rangle$	$\left|\Psi_{00R}\right\rangle \rightarrow \left|\Psi_{01R}\right\rangle$
0/360°	π	-
9°	2π	π
90°	6.4π	6.5π
162°	π	2π
171°	-	π
180°	π	-
189°	2π	π
270°	6.4π	6.5π
342°	π	2π
351°	-	π

Table 5.11: The area $A(\chi)$ of the first IR laser pulse calculated for the values given in eqn. (5.81) and (5.82) for the orientation angles χ marked by arrows in fig. 5.37. Note that 1π refers to the exact value of $A(\chi = 0°)$ which is 1.06π.

In general, the more χ increases the stronger the interaction of $\vec{E}_Z^0$ with $\vec{\mu}^{01L/R}$ becomes since the increasing value of the y-component $|E_y^0(\chi)|$ is multiplied with the relatively high value of $\mu_y^{01L/R}$ (see eqn. 5.82), which means that $\vec{E}_Z^0$ and $\vec{\mu}^{01L/R}$ become parallel. These intense laser pulses excite the population not only to $|\Psi_{01L/R}\rangle$ but also to higher states $|\Psi_{02L/R}\rangle$, $|\Psi_{03L/R}\rangle$ and $|\Psi_{04L/R}\rangle$. As a consequence, the curves in fig. 5.36 show broad minima around $\chi = 90°$ and $\chi = 270°$. It is important to note that not only the curves in fig. 5.37 reach their maxima around $\chi = 90°$ and $270°$, but that at exactly these angles the interaction with the R-enantiomer is slightly stronger than with the L-enantiomer (6.5π vs. 6.4π), see tab. 5.11 and dotted vertical lines in fig. 5.37. This will become more important for the effect of the second laser pulse.

The second laser pulse was optimized to transfer selectively the population in $|\Psi_{01L}\rangle$ to the electronic excited state S_1, specifically to the target state $|\Phi_{1384g}^1\rangle$, see section 5.4.3. The laser field propagating in Y-direction is also written in terms of the orientation angle χ as (in at. un., i.e. in E_h/ea_0)

$$\vec{E}_Y^0(\chi) = \begin{pmatrix} 6.22\cos\chi \\ 6.22\sin\chi \\ 0.186 \end{pmatrix} \cdot 10^{-3}. \tag{5.83}$$

The transition dipole vectors interacting with $\vec{E}_Y^0$ are denoted $\vec{\mu}^{1Le}$ and $\vec{\mu}^{1Re}$, where the e stands for the target state $|\Phi_{1384g}^1\rangle$, and are they defined as in eqns. (5.78) and (5.79). For $\vec{\mu}^{1Le}$ one obtains using the numerical values from tab. 5.7 (in at. un., i.e. in ea_0):

$$\begin{aligned} \vec{\mu}^{1Le} &= \begin{pmatrix} \langle\Psi_{01L}|\,\mu_x^{01}\,|\Phi_{1384g}^1\rangle \\ \langle\Psi_{01L}|\,\mu_y^{01}\,|\Phi_{1384g}^1\rangle \\ \langle\Psi_{01L}|\,\mu_z^{01}\,|\Phi_{1384g}^1\rangle \end{pmatrix} = \frac{1}{\sqrt{2}} \begin{pmatrix} \langle\Phi_{01u}^0|\,\mu_x^{01}\,|\Phi_{1384g}^1\rangle \\ \langle\Phi_{01g}|\,\mu_y^{01}\,|\Phi_{1384g}^1\rangle \\ \langle\Phi_{01g}|\,\mu_z^{01}\,|\Phi_{1384g}^1\rangle \end{pmatrix} \\ &= \frac{1}{\sqrt{2}} \begin{pmatrix} -2.44 \\ -23.1 \\ -88.2 \end{pmatrix} \cdot 10^{-3} \end{aligned} \tag{5.84}$$

The respective interaction vector $\vec{\mu}^{1Re}$ has a positive x-component ($\mu_x^{1Re} = +2.44 \cdot 10^{-3}$ at. un.). Note that the values in eqn. (5.84) are derived from the wave packet in S_1 at the peak of the second laser pulse $|\Psi^1(t = 10.5\text{ps})\rangle$ and not from the original target state $|\Phi_{1384g}^1\rangle$, see section 5.4.3.

As for the first IR laser pulse 144 simulations along χ in steps of $2.5°$ were carried out using the laser field calculated by equation (5.83). For each χ the quantum dynamical simulations started at the end of the first IR laser pulse. The overall population in S_1 at the end of the second laser pulse versus the orientation angle χ is plotted in figure 5.38 (top).

At $\chi = 0°$ almost all population of $|\Psi_{01L}\rangle$ is pumped to S_1 while the R-enantiomer is uneffected.[20] At $\chi = 180°$ the x-component of $\vec{E}_Y^0$ has changed its sign (see eqn. 5.83) and hence, the product $\vec{E}_Y^0 \cdot \vec{\mu}^{1Le}$ becomes zero. Neither the population in $|\Psi_{01L}\rangle$ nor in $|\Psi_{00R}\rangle$ will be touched by this laser field, and therefore, both curves in fig. 5.38 (top) reach zero – as predicted above (see tab. 5.8).

In figure 5.38 (bottom) the curve of the R-enantiomer is shifted by -13°, because at this angle $\vec{E}_Y^0 \cdot \vec{\mu}^{1Le}$ equals zero. Since the shifted curves do not coincide the amount of enantiomeric excess created by the laser pulse sequence can already be anticipated from figure 5.38 (bottom). The intergrals under the curves of fig. 5.38, using the values of the calculated points, yield that 10% more population of the R-enantiomer (1:0.9 for R:L) is excited to S_1, mainly due to the region around $\chi = 90°$.

To understand how this enantiomeric excess in S_1 is achieved it is necessary to look at the pulse area of the UV laser pulse. Figure 5.39 shows the pulse area $A(\chi) = \vec{E}_Y^0(\chi) \cdot \vec{\mu}^{1L/Re} \cdot t_p/2$ in units of π as a function of χ calculated for the values in eqns. (5.81) and (5.82). Solid and dashed curves are used for interaction with the L- and R-enantiomer, respectively. The solid horizontal line marks the value of $A \approx \pi$, the dot-dashed lines mark the value of approximately 4π and 5π. Solid and dashed lined arrows mark the angles at which a π-pulse transition for the L- and R-enantiomer, respectively, is expected. In table 5.12 the calculated values of A are listed for several orientation angles. The two curves in fig. 5.39 are shifted by $\sim 13°$ which confirms the results found in fig. 5.38 (bottom). The reason is that at $\chi = 193°$ the L-enantiomer is excited leaving the R-form untouched, while at 347° the opposite effect is found (see arrows in fig. 5.39).

As derived before, at $\chi = 90°$ and 270° only the y- and the z-component of the UV laser field $\vec{E}_Y^0$ (see eqn. 5.83) interact with the transition dipole vector $\vec{\mu}^{1L/Re}$ (cf. fig. 5.35 middle and right) and because $\mu_y^{1Le} = \mu_y^{1Re}$ and $\mu_z^{1Le} = \mu_z^{1Re}$, no enantio-selectivity can be achieved at either angle. Figure 5.36 proves that at these angles (see dotted vertical lines) no selectivity can be expected since both curves cross. At $\chi = 90°$ the pulse area becomes approximately 5π (see tab. 5.12) which means that the population of both $|\Psi_{01L}\rangle$ and $|\Psi_{01R}\rangle$ should be transferred completely to the target state. At the angle $\chi = 270°$ a $\sim 4\pi$-pulse is found, see fig. 5.39, hence no population should be excited. Still, population is transferred to S_1 at $\chi = 270°$, see fig. 5.38. Therefore, most of the transferred population at $\chi = 270°$, and then also at $\chi = 90°$, is probably due to the effect of high laser intensity, beyond the limit of the theory for π-pulses. However, at exactly $\chi = 90°$ more population of the R-enantiomers is excited to S_1, see fig. 5.38. At this angle (and also at 270°) the first IR laser pulse interacts slightly stronger with the R-enantiomer than with the L-enantiomer, as shown in figures 5.36 (top) and 5.37, and hence, $|\Psi_{00R}\rangle$ was depopulated

---

[20]Many states in S_1 are populated, not only the target state $|\Phi_{1384g}^1\rangle$, see section 5.4.3.
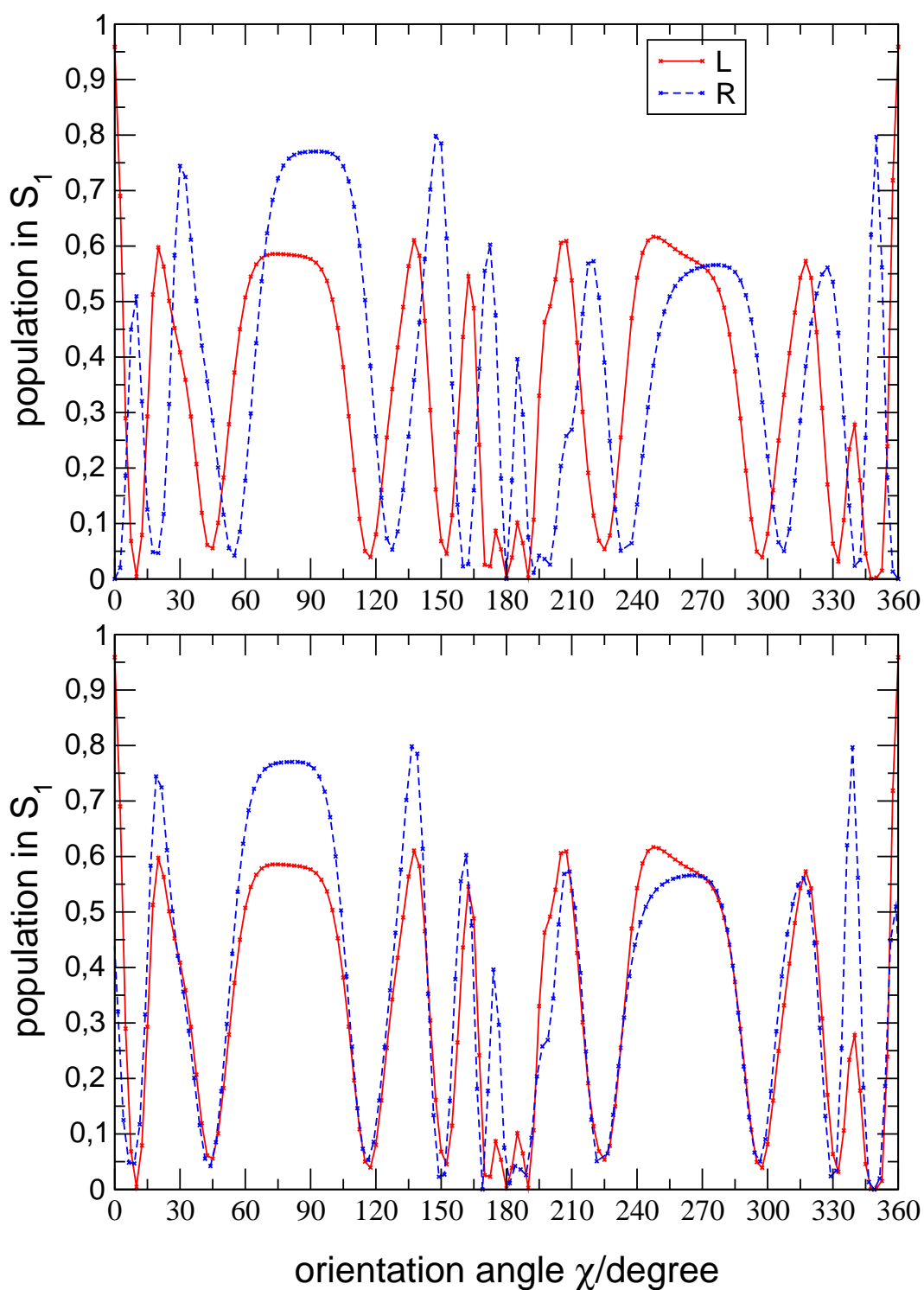
Figure 5.38: Top panel: Total population of the *L*-enantiomer (plain line) and the *R*-enantiomer (dashed line) in S_1 versus χ (in steps of 2.5°) after the sequence of the enantio-selective IR and UV pump pulse depicted in fig. 5.30. Bottom panel: The curve for the population of *R*-enantiomer is shifted by -13° (see text).

more than $|\Psi_{00L}\rangle$. As a concequence, at $\chi = 90°$ more R-population is transferred to S_1 by the second UV laser pulse, see fig. 5.38 (top). At $\chi = 270°$ one would expect the same effect which would increase the enantiomeric excess in S_1 in favor of the R-enantiomer. However, the population excited to S_1 is almost equal for both enantiomers confirming the effect of high laser intensity.
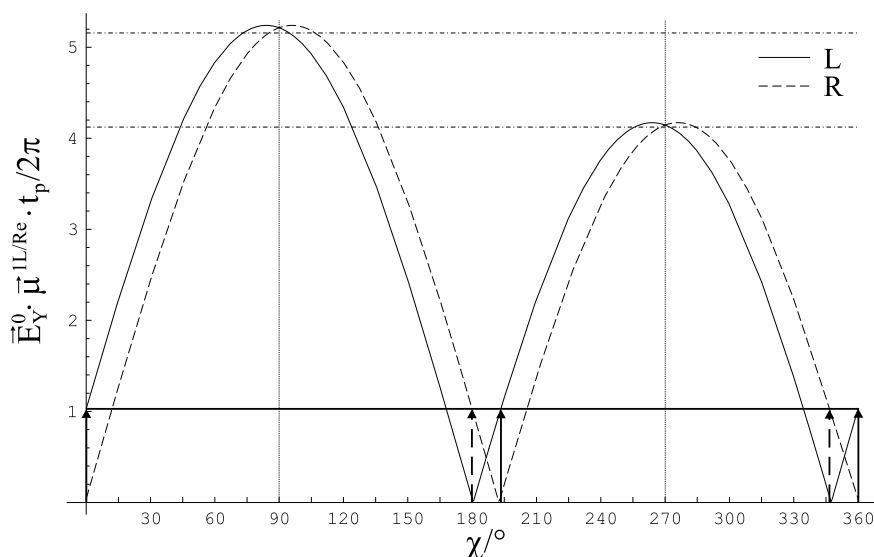

Figure 5.39: The area $A(\chi) = \vec{E}_Y^0(\chi) \cdot \vec{\mu}^{1L/Re} \cdot t_p/2$ of the second UV laser pulse in units of π calculated for the values given in eqn. (5.83) and (5.84). The plain horizontal line marks the value for which $\sim 100\%$, corresponding to a π pulse, population transfer from $|\Psi_{01L/R}\rangle$ to S_1 is accomplished. The two horizontal dot-dashed lines correspond to a pulse area of approximately 4π and 5π. The solid and dashed lined arrows mark the angles χ for the L- and R-selective transitions listed in tab. 5.12.

orientation angle χ	$|\Psi_{01L}\rangle \rightarrow S_1$	$|\Psi_{01R}\rangle \rightarrow S_1$
0/360°	π	-
90°	5π	5π
180°	-	π
193°	π	-
270°	4π	4π
347°	-	π

Table 5.12: The area $A(\chi)$ of the second UV laser pulse calculated for the values given in eqn. (5.83) and (5.84) for the orientation angles marked by arrows in fig. 5.39. Note that 1π refers to the exact value of $A(\chi = 0°)$ which is 1.03π.

Table 5.13 summarizes the transitions induced by the laser pulse sequence at four orientation angles. Note that not only these four angles χ contribute to the enantiomeric excess in S_1 found. However, the table stresses two important effects of the laser control: a) At $\chi = 180°$ no population is transferred to S_1, and b) At $\chi = 90/270°$ the UV laser pulse cannot differentiate between the L- and R-enantiomer. The consequences are: a) While at $\chi = 0°$ the population transfer for the L-enantiomer is almost 100%, at $\chi = 180°$ no population of the R-enantiomer is excited to S_1.[21] b) Since at $\chi = 90/270°$ the first laser pulse cannot excite the population of both enantiomers by the same extent, at these angles the second laser pulse creates an enantiomeric excess in S_1, as predicted by the theory.

orientation angle χ	1st pulse $\vec{E}_Z^0$ (IR)		2nd pulse $\vec{E}_Y^0$ (UV)	
	$|\Psi_{00L}\rangle \rightarrow |\Psi_{01L}\rangle$	$|\Psi_{00R}\rangle \rightarrow |\Psi_{01R}\rangle$	$|\Psi_{01L}\rangle \rightarrow S_1$	$|\Psi_{01R}\rangle \rightarrow S_1$
0°	π	-	π	-
90°	6.4π	6.5π	5π	5π
180°	π	-	-	π
270°	6.4π	6.5π	4π	4π

Table 5.13: The pulse area A for the enantio-selective IR+UV laser pulse sequence as a function of the orientation angle χ for the case of molecules being oriented along the Z-axis.

The effects a) and b) depend on the axis along which the molecules are oriented. Therefore, it is interesting to investigate these effects for the case where the molecules are oriented along the Y- or the X-axis and thereby test the predictions made in tables 5.9 and 5.10. For this purpose, the pulse area A is calculated for the four orientation angles $\chi = 0°, 90°, 180°$ and $270°$.

For the case of molecules being oriented along the Y-axis the laser fields of both pulses are rotated clockwise around the y-axis:

$$\vec{E}^0(\chi) = \begin{pmatrix} \cos\chi & 0 & \sin\chi \\ 0 & 1 & 0 \\ -\sin\chi & 0 & \cos\chi \end{pmatrix} \begin{pmatrix} E_x^0 \\ E_y^0 \\ E_z^0 \end{pmatrix} = \begin{pmatrix} E_x^0 \cos\chi + E_z^0 \sin\chi \\ E_y^0 \\ -E_x^0 \sin\chi + E_z^0 \cos\chi \end{pmatrix}. \qquad (5.85)$$

With the values of the transition dipole vectors from eqns. (5.82) and (5.84), A is calculated and listed in table 5.14. As predicted in tab. 5.9 the first pulse cannot differentiate between the L- and R-form of the molecules at $\chi = 90°$ and $\chi = 270°$. However, the

---

[21]This could not be expected for a sequence of parallel propagating laser pulses.

slight difference in enantio-selectivity (17.36π vs. 17.39π) of the UV pulse at these angles would cause an enantiomeric excess of the R-enantiomer in S_1.

orientation angle χ	1st pulse $\vec{E}_Z^0$ (IR)		2nd pulse $\vec{E}_Y^0$ (UV)	
	$|\Psi_{00L}\rangle \rightarrow |\Psi_{01L}\rangle$	$|\Psi_{00R}\rangle \rightarrow |\Psi_{01R}\rangle$	$|\Psi_{01L}\rangle \rightarrow S_1$	$|\Psi_{01R}\rangle \rightarrow S_1$
0°	π	-	π	-
90°	0.04π	0.04π	17.36π	17.39π
180°	-	π	π	-
270°	0.96π	0.96π	17.36π	17.39π

Table 5.14: The pulse area $A(\chi)$ for the enantio-selective IR+UV laser pulse sequence as a function of the orientation angle χ for the case of molecules being oriented along the Y-axis. Note that 1π refers to the exact value of $A(\chi = 0°)$ which is 1.06π for the IR pulse and 1.03π for the UV pulse.

For the case of orientating the molecules along the X-axis the electric field vectors of both pulses are rotated clockwise around the x-axis:

$$\vec{E}^0(\chi) = \begin{pmatrix} 1 & 0 & 0 \\ 0 & \cos\chi & -\sin\chi \\ 0 & \sin\chi & \cos\chi \end{pmatrix} \begin{pmatrix} E_x^0 \\ E_y^0 \\ E_z^0 \end{pmatrix} = \begin{pmatrix} E_x^0 \\ E_y^0 \cos\chi - E_z^0 \sin\chi \\ E_y^0 \sin\chi + E_z^0 \cos\chi \end{pmatrix}. \qquad (5.86)$$

The pulse area A is calculated for four cases, see table 5.15, using the values of the transition dipole vectors in eqns. (5.82) and (5.84). As expected from tab. 5.10, the transitions induced at $\chi = 0°$ and 180° bring no change to the initial racemic mixture eliminating effect a). At $\chi = 90°$ and 270° there is a preference for one chiral form for both pulses, see tab. 5.15. However, since the effect at $\chi = 90°$ and 270° are opposite, no enantiomeric excess will be achieved in S_1 at these angles destroying the effect b).

orientation angle χ	1st pulse $\vec{E}_Z^0$ (IR)		2nd pulse $\vec{E}_Y^0$ (UV)	
	$|\Psi_{00L}\rangle \rightarrow |\Psi_{01L}\rangle$	$|\Psi_{00R}\rangle \rightarrow |\Psi_{01R}\rangle$	$|\Psi_{01L}\rangle \rightarrow S_1$	$|\Psi_{01R}\rangle \rightarrow S_1$
0°	π	-	π	-
90°	0.54π	0.46π	0.34π	0.62π
180°	-	π	-	π
270°	0.46π	0.54π	0.62π	0.34π

Table 5.15: The pulse area A for the enantio-selective IR+UV laser pulse sequence as a function of the orientation angle χ for the case of molecules being oriented along the X-axis. Note that 1π refers to the exact value of $A(\chi = 0°)$ which is 1.06π for the IR pulse and 1.03π for the UV pulse.

In summary, the predictions made using a simplified model for molecules oriented along the X-, Y- or Z-axis were confirmed by the numerical simulations based on the model system 4-Me(C_6H_9)CHF. A sequence of two perpendicular propagating enantio-selective laser pulses was applied to a racemate of molecules oriented along the Z-axis. Even though this laser pulse sequence was originally optimized for a racemic mixture of pre-oriented molecules (see section 5.4.3), an enantiomeric excess of 10% was created in the electronic excited state of the unidirectionally aligned but randomly oriented molecules. The polarization directions of both laser fields are almost 90° (cf. tab. 5.7) corresponding to a polarization nearly in x-direction. This causes the graphs for the L- and R-enantiomer in figures 5.36 and 5.38 to be shifted only by a few degrees making chiral discrimination very sensitive with respect to the orientation angle χ. A close look at figures 5.37 and 5.39 also reveals that if the laser pulses were optimized at $\chi = 0°$ to couple to transition matrix elements with higher values the maxima of the curves could possibly be reduced drastically suppressing very high laser intensities (see previous discussion). Therefore, the here applied laser pulse sequence can be considered a rather unfavorable case for an essemble of molecules oriented along the Z-axis. However, the positions of the maxima of the $A(\chi)$-curves depend both on the laser parameters and on the axis along which the molecules are oriented, cf. tables 5.14 and 5.15. From the results obtained in this section it can be anticipated that the choice of the laser induced transitions as well as the axis along which the molecules are oriented are decisive for the success of creating enantiomeric excess. Therefore, it would be interesting to investigate laser excitations with more favorable laser-dipole couplings and, by doing that, also estimate the effect of the relative polarization direction between both perpendicular propagating laser fields on the enantio-selectivity. In this sense, this approach could also be tested for control mechanisms including sequences of parallel propagating laser pulses.

Note that, the here presented model simulation differs from the purification of a racemate of unidirectionally oriented, but rotating H_2POSH molecules by means of circularly polarized laser pulses, see section 4.6.5. While in the case of rotating H_2POSH molecules the inital state of the calculation is characterized by the quantum state $M = 0$ representing all possible molecular orientations of a single molecule around its chiral axis, here an essemble of molecules oriented along a specific laboratory fixed axis with different orientation around this axis is considered. Further, the quantum simulations of H_2POSH include the overall rotation of the molecules as a degree of freedom, while in the here presented model simulations the overall rotation, i.e. a coupling to the cyclohexyl ring, is neglected.